Optical and Excited-State Properties of Complex Metal Alloy Systems: $(Ga_{1-x}Zn_x)(N_{1-x}O_x)$ Nanoparticles and Ag-TiO_2 Films

by

Marta Sulima

B.A., Chemistry, Cornell University, 2014

A thesis submitted to the

Faculty of the Graduate School of the

University of Colorado on partial fulfillment

of the requirement for the degree of

Doctor of Philosophy

Department of Chemistry

2019

This thesis entitled:

Optical and Excited-State Properties of Complex Metal Alloy Systems: $(Ga_{1-x}Zn_x)(N_{1-x}O_x)$ Nanoparticles and Ag-TiO_2 Films

written by:

Marta Sulima

has been approved for the Department of Chemistry by:

Gordana Dukovic

Garry Rumbles

Date

The final copy of this thesis has been examined by the signatories, and we find that both the content and the form meet acceptable presentation standards of scholarly work in the above mentioned discipline.

Sulima, Marta (Ph.D., Chemistry)

Optical and Excited-State Properties of Complex Metal Alloy Systems: $(Ga_{1-x}Zn_x)(N_{1-x}O_x)$ Nanoparticles and Ag-TiO_2 Films

Thesis directed by Associate Professor Gordana Dukovic

Abstract

Solar fuel generation utilizing various nanomaterial light absorbers is a promising strategy to address current issues in energy production. Suitable materials for photochemical fuel production must combine properties of visible light absorption, suitable band edge potentials for catalysis, resistance to photooxidation, and long-lived excited states. Such requirements have revealed the need for materials with complex optical and excited state properties. Understanding these properties is important for improving material design for solar fuel generation. Herein, using femtosecond transient absorption (TA) spectroscopy, we study two complex metal alloy systems with properties relevant to solar fuel generation. The first part of this dissertation discusses optical and excited state properties in $(Ga_{1-x}Zn_x)(N_{1-x}O_x)$ nanoparticles. We discovered that $(Ga_{1-x}Zn_x)(N_{1-x}O_x)$ nanoparticles contain excited-state carriers with large reduced effective masses and revealed a free carrier density-dependent Burstein-Moss spectral shift. In addition, decay kinetics were found to exhibit a short-lived component assigned to trap mediated and Auger recombination and a long-lived component assigned to a broad distribution of trap states and trap-limited recombination. Furthermore, we studied these excited state properties in $(Ga_{1-x}Zn_x)(N_{1-x}O_x)$ nanoparticles with various elemental distributions and established that elemental distribution does not have a significant impact on recombination kinetics. The second part of the dissertation discusses the excited state properties in Ag-TiO_2 films which are composed of Ag nanoparticles embedded in a mesoporous TiO_2 host. TA spectroscopy was used to probe electron transfer

between Ag and TiO_2 upon visible and ultraviolet illumination. It was proposed that upon UV illumination, electron transfer from excited TiO_2 to Ag nanoparticles occurs, and upon visible illumination, the surface plasmon resonance (SPR) in Ag is excited and a direct electron transfer into TiO_2 follows. Revealing behavior of carriers in both of these systems upon illumination leads to insights for future material design and applications.

Acknowledgments

I have been so fortunate to have many influential people in my life who have all helped me along the way to completing this dissertation. First, I would like to thank my advisor Professor Gordana Dukovic. Without your mentorship, I would not be the independent researcher I am today. I would also like to thank my other committee members; Garry Rumbles, Nathan Neale, Niels Damrauer, and Steven George. A huge thank you to all of my amazing, former and current, group members – Leah Hall, Pornthip Tongying, Nelly Couzon, Chi-Hung Chuang, Kyureon Lee, Hayden Hamby, Orion Pearce, James Utterback, Amanda Grennell, Helena Keller, Madison Jilek, Kristina Vrouwenvelder, Nicholas Pogranichniy, Jesse Ruzicka, Tais Labrador, Lauren Pellows, Shelby Beer, Katherine Shinopoulos, Molly Wilker, Kyle Schnitzenbaumer, and Yinggang Lu – for all of your support and friendship over the past five years. A special thank you to Leah Hall for being a wonderful lab mate and friend. Being the only two on the "oxynitride project" throughout the entirety of these past 5 years has certainly been a challenge and I am glad that we have gone through it together. Another special thank you to Pornthip, Chi-Hung, and Kyureon, for your mentorship on the "oxynitride project" for the first few years of my time here. Thank you to Nelly Couzon, for your collaboration on the Ag-TiO_2 project, which I always called, "The Nelly Project."

Next, I want to thank my family, for all of their love and support, not just through these past five years, but my whole life. Thank you, Mom and Dad for always believing in me and helping me along the way. Thank you to my twin sister Monika. I truly believe that growing up with you influenced me to push myself to always do my best. Thank you to my brilliant brother-in-law Philip, who was always willing to help with Quantum HW. I want to also thank my family in Poland for always sending well wishes from afar. Finally, an immense thank you to my partner Ryan. I would not have made it through these five years without all of your love and support.

Thank you for all of your patience and always being willing to read my work and listen to practice presentations.

Thank you to all of my friends that have made my time in Boulder so memorable. Alexa and Robbie, I am so grateful for all of our weekend adventures. Spending time with you helped ease the stress of graduate school. Alina, Aroob, Rob, and Samantha – I am so glad to have made friends like you in my time here at CU Boulder.

Thank you to all those who inspired me to pursue graduate school. Professor Shannon Boettcher and Professor Poul Peterson, thank you for giving me the opportunity to explore research as an undergraduate.

Finally, I acknowledge the funding sources that have allowed me to complete this work – The Beckman Foundation and STROBE.

Table of Contents

List of Tables

List of Figures

Chapter 1. Introduction

1.1 Motivation

Global energy consumption has continued to increase since the onset of the industrial revolution and will continue to increase as industry and world population continue to grow.[1,2] Global energy demands have resulted in extensive use of carbon-based fuels such as natural gas, oil, and coal.[3] However, these resources are being quickly depleted and burning these fuels to use as energy sources, results in the release of greenhouse gases like CO_2 and noxious gases including SO_x and NO_x.[4] The release of these gases into our atmosphere not only leads to pollution, but increases global temperatures. Global warming has many negative impacts on the environment, including shrinking glacial ice, increased ocean levels, increased ocean acidity, and damage to ecosystems and agriculture.[5-7] These consequences of our reliance on fossil fuels make it vital that we start to move towards a clean and renewable form of energy. One sustainable and renewable form of energy that has gained considerable interest is solar energy.[8] Having such an abundant source of energy, where the amount of solar energy hitting the Earth's surface in two hours is more than the global energy use in a year, it is imperative to convert solar energy into chemical or electrical energy.[1]

Utilizing nanomaterial semiconductors for solar fuel generation is a desirable approach.[9] Hydrogen as a fuel can be produced by splitting water and is an energy dense and clean fuel.[10] Suitable materials for solar fuel production are rare, as they need to satisfy various requirements. One major requirement is the absorption of visible light in order to use a large portion of the solar spectrum. In addition, these materials need to be stable and resist photooxidation. Many materials

satisfy some of these requirements, but do not always satisfy all of them. Therefore, it is necessary to develop new materials that can improve the efficiency of solar fuel generation.

Not only is it important to develop new materials for solar fuel generation, but it is also important to understand their optical and excited-state properties. In order to enhance performance of materials for solar fuel generation, we need to be able to understand their behavior upon illumination. In particular, we need to know how excited state carriers (electrons and holes) behave when they are generated. For example, electrons and holes can recombine via different pathways with different efficiencies, therefore effecting their utilization in necessary photocatalytic reactions.

1.2 Background

In this dissertation, the optical and excited state properties in $(Ga_{1-x}Zn_x)(N_{1-x}O_x)$ nanoparticles and Ag-TiO_2 films are studied. In this section, background information about $(Ga_{1-x}Zn_x)(N_{1-x}O_x)$ nanoparticles and Ag-TiO_2 films will be reviewed. In addition, an overview of transient absorption (TA) spectroscopy, the main analysis tool used to study these materials in this work, will be presented.

1.2.1 $(Ga_{1-x}Zn_x)(N_{1-x}O_x)$: A Solid solution of GaN and ZnO

$(Ga_{1-x}Zn_x)(N_{1-x}O_x)$ was first synthesized in its bulk form as a solid solution of ZnO and GaN by the Domen group, in 2005.[11] The resulting material showed promise for photocatalytic ability due to its tunable visible bandgap (based on x value), despite the parent materials ZnO and GaN exhibiting ultraviolet (UV) bandgaps.[12] $(Ga_{1-x}Zn_x)(N_{1-x}O_x)$ has been shown to be capable of splitting water into H_2 and O_2 under visible light illumination and increased photocatalytic activity when modified with cocatalysts.[12-22] However, the quantum efficiency of water-splitting has never exceeded 20%, indicating significant energy-loss pathways present within the material.[23]

Our group sought to synthesize $(Ga_{1-x}Zn_x)(N_{1-x}O_x)$ on the nanoscale, which could increase catalytic activity due to higher surface to volume ratios in nanoscale particles. Hahn *et al,* produced $(Ga_{1-x}Zn_x)(N_{1-x}O_x)$ nanotubes which demonstrated improved photocatalytic activity as compared to bulk products.[24] In 2012, our group synthesized $(Ga_{1-x}Zn_x)(N_{1-x}O_x)$ on the nanoscale with a wide range of x values from x=0.30 to 0.87.[25] Later, an even broader range from x=0.06 to 0.98 was achieved.[26] The synthetic method involved using nanoscale ZnO and $ZnGa_2O_4$ precursors that were combined and heated to 650 °C under a flow of NH_3, resulting in our $(Ga_{1-x}Zn_x)(N_{1-x}O_x)$ nanoparticles. The resulting particles exhibited a tunable visible absorption. Figure 1.1 shows the diffuse reflectance spectra at various x values, where bandgap clearly increases with decreasing x value. The origin of this tunable visible bandgap has been explored. Early reports from the Domen group suggested that repulsion between Zn3d and N2p orbitals in the valence band results in an upward shift of the band, resulting in a narrower bandgap.[12] Other studies have focused on understanding the origin of this visible absorption, theoretically and experimentally, but the reason is still up for debate.[27-33] Work in Chapter 3 of this dissertation further explores optical properties in $(Ga_{1-x}Zn_x)(N_{1-x}O_x)$ nanoparticles.

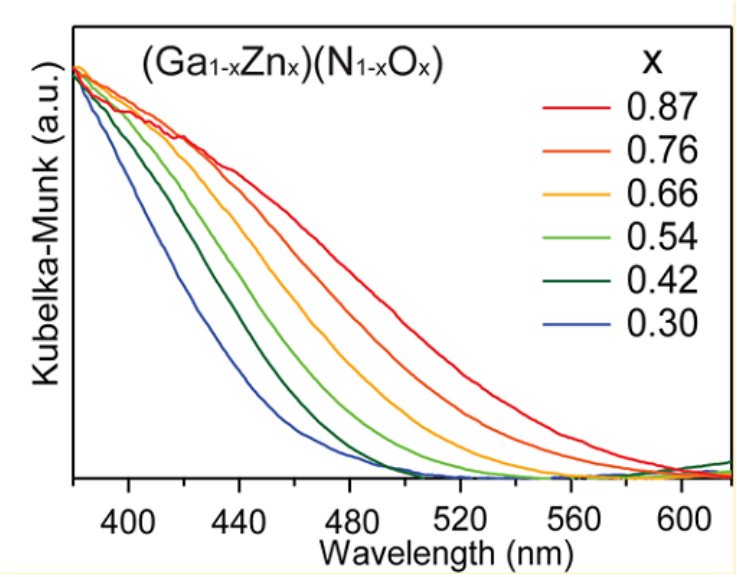

Figure 1.1. Diffuse reflectance transformed Kubelka Munk plots of $(Ga_{1-x}Zn_x)(N_{1-x}O_x)$ nanoparticles with different x values. As x value (shown in legend) increases, absorption onset wavelength also increases. Adapted from *Nano Letters* **2012**, 12, 3268-3272. © Copyright 2012 Nano Letters.

Further work in our group to determine the mechanism of formation of $(Ga_{1-x}Zn_x)(N_{1-x}O_x)$ led to the conclusion that a topotactic nucleation occurs between ZnO and $ZnGa_2O_4$ precursors.[26] Later, we found that particles synthesized at 650 °C exhibit heterogeneous elemental distributions, where Zn and O are localized to the center of the particle, while Ga and N are localized to the edges of the particles.[34] With an increase in synthesis temperature to 800 °C, we determined that the particles had elemental distributions that were evenly distributed throughout the particles. Figure 1.2 shows the proposed scheme for how synthesis temperature changes the resulting particle distribution. The formation mechanism involves phase transformation, nitridation, and diffusion of Ga, Zn, N, and O. At higher temperatures, each of these steps effectively allows for the production of homogeneous particles, while at 650 °C, nitridation, and diffusion are concentrated to the edges of the particles.[34]

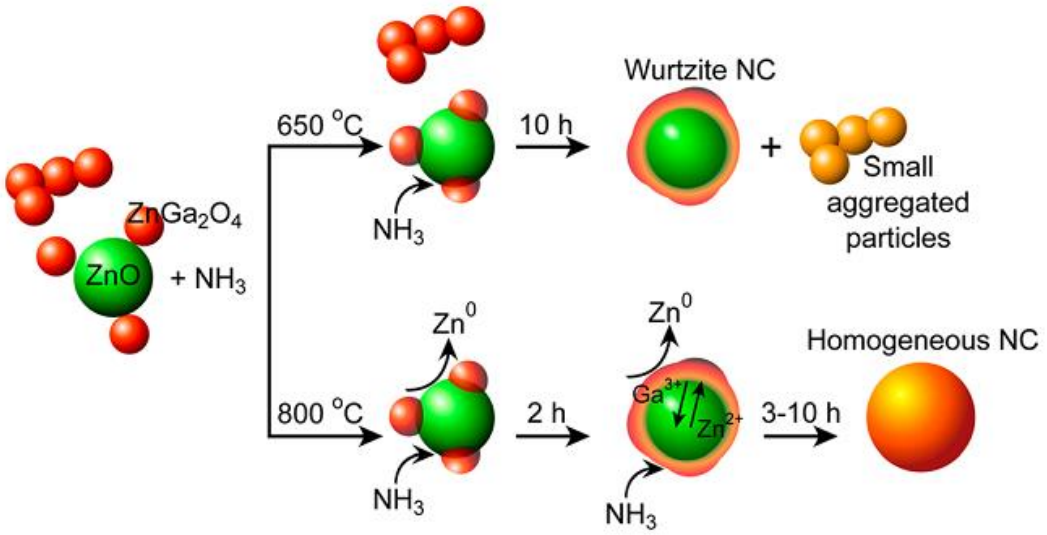

Figure 1.2. Scheme representing the synthesis mechanism of $(Ga_{1-x}Zn_x)(N_{1-x}O_x)$ nanoparticles at 650 °C and 800 °C. Synthesis at 650 °C results in heterogeneous nanoparticles and small aggregated particles, while synthesis at 800 °C results in homogeneous particles. Adapted from *ACS Nano* **2017**, 11, 8401-8412. © Copyright 2017 ACS Nano.

1.2.2 Excited State Dynamics in $(Ga_{1-x}Zn_x)(N_{1-x}O_x)$

Previous work in our group to understand the excited-state decay in $(Ga_{1-x}Zn_x)(N_{1-x}O_x)$ nanoparticles involved using transient absorption spectroscopy to study a sample with an x value of 0.73.[35] In order to perform absorption experiments, the particles needed to be solubilized. As synthesized, $(Ga_{1-x}Zn_x)(N_{1-x}O_x)$ particles are in their powder form.[25] In order to obtain particles in solution, they were functionalized in toluene with octadecyltrimethoxysilane (ODTMS) ligands.[35] Excite-state decay measurements revealed a short (15-30 ps) component, which comprised 55% of the decay and a long-lived component with an average lifetime of ~30 μs, which comprised the remaining 45% of the decay. The goal here was to elucidate what these short and long-lived decay components were due to. This is explored in Chapters 4 and 5 of the dissertation.

1.2.3 Ag-TiO_2

Silver nanoparticles possess unique and tunable optical properties.[36] One particularly unique property of metallic nanomaterials is their surface plasmon resonance (SPR), which is due to the

coherent oscillation of conduction band electrons induced by interaction with light.[36-39] Plasmonic metal nanoparticles exhibit tunable absorption, based on size and shape, across the entire visible spectrum.[36,39,40] Thus, incorporating them into photocatalytic systems would be very promising for improving efficiency of solar energy conversion. Particularly, Ag nanoparticles attached to semiconductors such as TiO_2 prove to be promising for their use in applications for solar fuel generation.[41] The interaction between metal nanoparticles and semiconductors results in three potential processes. These are shown in Figure 1.3. Upon visible illumination, plasmon-induced charge separation (PICS), or direct electron transfer can occur. In this case, the SPR in the silver nanoparticles generates hot electrons that are then injected into the TiO_2 conduction band.[36,42] Under UV illumination, TiO_2 is excited and the resulting conduction band electron transfers from TiO_2 into Ag. This is known as the co-catalysis effect.[42] Finally, the nanoantenna effect occurs when Ag nanoparticles are not in direct contact with TiO_2 (~10 nm) and a localized surface plasmon resonance (LSPR) of the Ag nanoparticles transfers electromagnetic energy back and forth across the distance between the semiconductor and nanoparticle.[42] In Chapter 6, we seek to study the electron transfer between Ag and TiO_2 in an Ag-TiO_2 film in order to distinguish between these processes and to quantify the electron transfer.

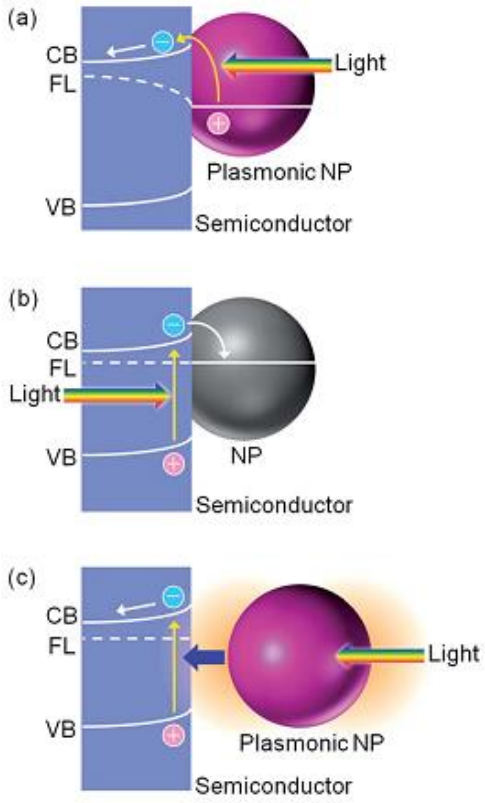

Figure 1.3. Representation of three processes that occur in metal nanoparticle-semiconductor systems. (a) Plasmon induced charge separation (PICS), or direct transfer, occurs when visible light excites the SPR in the metal nanoparticle and then a hot electron is injected into the conduction band (CB) of the semiconductor. (b) Co-catalysis effect occurs when an electron is excited into the CB of the semiconductor and then transfers into the metal nanoparticle. (c) Plasmonic nanoantenna effect occurs when the plasmonic nanoparticle (NP) and semiconductor are not in direct contact, but ~10 nm apart. Adapted from *Chemical Science* **2017**, *8*, 3325-3337. © 2017 Chemical Science.

1.2.4 Transient Absorption (TA) Spectroscopy

TA spectroscopy was used throughout the work presented in this dissertation to experimentally probe the excited-state dynamics and spectra in $(Ga_{1-x}Zn_x)(N_{1-x}O_x)$ nanoparticles and films of Ag nanoparticles embedded in mesoporous TiO_2 (Ag-TiO_2). TA spectroscopy is a pump-probe technique during which a pump pulse of monochromatic light of a chosen wavelength is used to photoexcite the sample (Figure 1.4.) Then, a probe pulse is sent through the sample at various time delays after the pump pulse. The probe pulse measures changes in the absorption spectrum of the

material after excitation with the pump pulse, resulting in a difference absorption spectrum, ΔA, which is calculated by comparing the probe absorption with and without excitation, and taking their difference. Monitoring the ΔA spectrum at a given wavelength over a range of time delays, results in a decay kinetic trace which holds information about the time evolution of the photoexcited states. In this dissertation, we perform experiments using visible and near infrared (NIR) TA spectroscopy. The visible TA spectroscopy utilizes a white light probe pulse to measure the absorption, while in the NIR an infrared probe pulse is generated. Experiments are performed at timescales from 0 to 8 ns and from 0.3 ns to 100 μs.

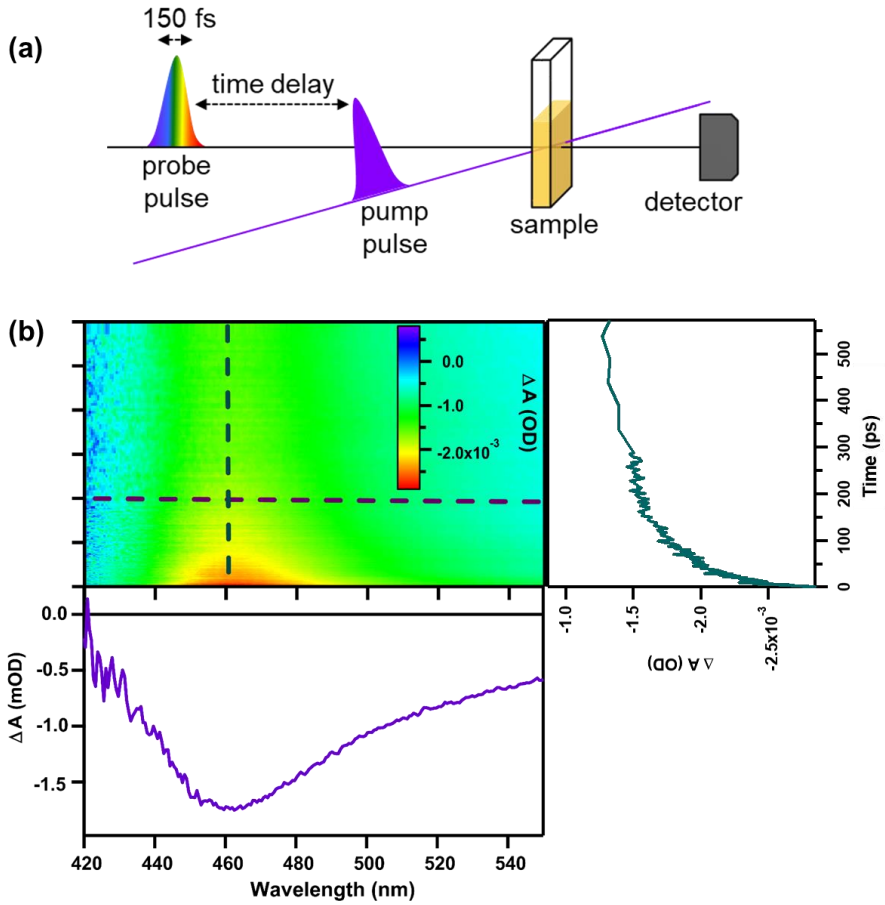

Figure 1.4. Transient absorption (TA) spectroscopy. (a) Representation of the pump-probe experiment, where the pump pulse of a particular wavelength is sent through the sample, followed by a probe pulse at various time delays after the pump pulse. The probe pulse is then detected and the probe spectrum with and without excitation is used to determine the ΔA spectrum. (b) Typical TA spectroscopy data for $(Ga_{1-x}Zn_x)(N_{1-x}O_x)$ ($\Delta A(t,\lambda)$). The TA spectrum can be extracted at a given time (purple traces) or at a particular wavelength (blue traces).

1.3 Summary and Outline of Dissertation

This dissertation focuses on understanding the excited-state and optical properties of metal oxide nanocrystal systems; $(Ga_{1-x}Zn_x)(N_{1-x}O_x)$ nanoparticles and Ag-TiO_2 films. Using various spectroscopic techniques, in particular, ultrafast transient absorption spectroscopy, we gain insight into the behavior of these materials upon illumination.

First, in Chapter 2, we describe the experimental methods used throughout this dissertation. Then, we explore the properties of two nanocrystal systems, first focusing on the $(Ga_{1-x}Zn_x)(N_{1-x}O_x)$ nanoparticles. Chapter 3 begins the study of $(Ga_{1-x}Zn_x)(N_{1-x}O_x)$ nanoparticles using steady-state measurements, in particular, diffuse reflectance spectroscopy. We apply a band fluctuations model to diffuse reflectance transformed Kubelka Munk plots to determine the Urbach tail energies and bandgaps in particles of varying composition and elemental distributions. In Chapters 4 and 5, we use TA spectroscopy to understand the carrier dynamics in these particles. Chapter 4 focuses on a sample with a composition of x=0.40 that was synthesized at 650 °C. We find that spectral shifts in visible TA spectra can be modeled by the Burstein-Moss theory, which led to the determination of the reduced effective mass of excited carriers in these particle. In addition, a carrier recombination model was used to determine that trap mediated and Auger recombination occur on a fast timescale, while a broad distribution of trap states results in a long-lived carrier decay component. In Chapter 5, we further explore the excited-state signals in $(Ga_{1-x}Zn_x)(N_{1-x}O_x)$ with homogeneous and heterogeneous elemental distributions. We find that elemental distribution does not play a large role in the recombination kinetics of these materials. Chapter 5 also explores TA signals probed in the NIR where we observe free carrier recombination. In this chapter, we also studied electron scavenger experiments to determine whether signals observed in TA spectroscopy of $(Ga_{1-x}Zn_x)(N_{1-x}O_x)$ were due to electrons, holes, or both.

The second nanocrystal system studied in this dissertation is Ag-TiO_2, a film of silver nanoparticles embedded in mesoporous TiO_2. Chapter 6 discusses TA spectroscopic studies performed on these Ag-TiO_2 films. We explored the behavior of this system upon UV and visible illumination to observe electron transfer between Ag nanoparticles and TiO_2. With UV excitation, electrons transfer from TiO_2 to Ag, while with visible excitation, SPR excited electrons transfer into TiO_2. Finally, Chapter 7 provides a summary of the work presented in this dissertation and an outlook for future experiments.

Chapter 2. Methods

2.1 Synthesis

2.1.1 $ZnGa_2O_4$ Nanocrystal Synthesis

All chemicals were purchased from Sigma-Aldrich and used without any additional purification. $ZnGa_2O_4$ nanoparticles were synthesized according to previously reported methods.[25] 2 mmol gallium acetylacetonate ($Ga(acac)_3$, 99.99%), 1 mmol zinc acetylacetonate hydrate ($Zn(acac)_2$, 99.995%), 6 mmol oleic acid (≥99.0%), 5 mmol of 1,2 hexadecanediol (90%), 6 mmol oleylamine (70%), and 10 mL of benzyl ether (98%) were placed in a three-necked round bottom flask and were heated to 40 °C under Ar. The temperature was then increased to 100 °C while under vacuum, after the solution became optically transparent. This was done in order to remove excess O_2 and H_2O from the reaction. Then, the temperature was raised to 200 °C for 30 minutes under Ar. Finally, the reaction was heated to 280 °C for 2 hours. Once the solution cooled to room temperature, the resulting $ZnGa_2O_4$ nanoparticles were collected using centrifugation and purified using 5 mL of hexane and precipitated using 45 mL of ethanol. The particles were dried under vacuum.

2.1.2 ZnO Nanocrystal Synthesis

All chemicals were purchased from Sigma-Aldrich and used without further purification. ZnO nanocrystals were synthesized following previously reported methods.[21] 40 mmol of zinc chloride ($ZnCl_2$, ≥98%) was dissolved in 200 mL of 1,2-ethanediol (99.8%) and heated to 150 °C in air. Then, 16 mL of a 5 M sodium hydroxide (NaOH) solution was added dropwise to the solution. The solution was constantly stirred using a stir bar and stir plate. The reaction temperature was

maintained at 150 °C. The solution was cooled to room temperature after all NaOH was added and a white powder formed. The resulting white powder was collected by sedimentation and the supernatant solution was decanted off. After the supernatant was discarded, the particles were washed with water five times to remove NaCl from the product. Finally, the ZnO nanoparticles were collected by centrifugation. They were then purified again three more times with water washes and then dried.

2.1.3 Ligand Exchange Procedure for $ZnGa_2O_4$ Nanocrystals

All chemicals were purchased from Sigma-Aldrich and used without further purification. The ligand exchange procedure was previously published.[25] $ZnGa_2O_4$ nanocrystals are synthesized with native ligands allowing for solubilization in non-polar solvents. We needed to exchange for hydrophilic ligands. Therefore, the $ZnGa_2O_4$ ligands were exchanged for 3-mercaptopropionic acid (3-MPA, ≥99.0%) using a modified synthesis previously reported.[43] 0.5 g of 3-MPA was dissolved in 3 mL of methanol. Tetramethyl ammonium hydroxide (≥97%) was added until the pH reached 11. Then, 60 mg of $ZnGa_2O_4$ nanoparticles were dispersed in 3 mL of hexane. To precipitate out $ZnGa_2O_4$ particles from this solution, 15 mL of ethanol was added. The 3-MPA solution was added to the hexane/ethanol/$ZnGa_2O_4$ mixture and stirred. 25 mL of toluene was added after the solution became optically clear, which indicated $ZnGa_2O_4$ solubility in polar solvents and then $ZnGa_2O_4$ particles with new ligands were collected by centrifugation. Finally, the resulting solid was dried under vacuum and then dissolved in 5 mL of water, washed with 20 mL of toluene, and 25 mL of ethanol, and collected by centrifugation and dried again.

2.1.4 $(Ga_{1-x}Zn_x)(N_{1-x}O_x)$ Nanocrystal Synthesis

All chemicals were purchased from Sigma-Aldrich and used without further purification. Synthesis of $(Ga_{1-x}Zn_x)(N_{1-x}O_x)$ was previously published.[25] ZnO and MPA-capped $ZnGa_2O_4$

nanoparticles were synthesized as solids. ~100 mg total (mass quantities were determined based on the desired Zn content or x value in the resulting particles) of ZnO and $ZnGa_2O_4$ nanoparticles were dispersed in a 1:1 water-ethanol mixture and sonicated to evenly mix the particles. The resulting slurry was deposited on a glass slide on a heating mantle set to ~100 °C to evaporate the solvent. The dry solid was scraped off the glass slide into an alumina boat which was then placed into a quartz tube furnace (Across International model STF 1200). Argon was flowed through the sealed furnace (without heating) for 1 hour. Then, ammonia gas (NH_3, 99.99%, Airgas) was flowed through the furnace at a flow rate of 100 mL/min. The temperature was set to either 650 °C or 800 °C for 10 hours.

2.1.5 $(Ga_{1-x}Zn_x)(N_{1-x}O_x)$ Solubilization

The synthesis method for $(Ga_{1-x}Zn_x)(N_{1-x}O_x)$ nanoparticles, described above, produces particles as an insoluble powder. In order to perform absorption experiments, the particles were solubilized using surface functionalization with octadecyltrimethoxysilane (ODTMS), as previously published.[35] 20 mg of $(Ga_{1-x}Zn_x)(N_{1-x}O_x)$ powder was dispersed in 6 mL of toluene (HPLC Plus, ≥99.0%) with continuous sonication. Then, 0.15 mL butylamine (99.5%, Sigma Aldrich) and 0.4 mL of ODTMS (90%, Sigma Aldrich) ligand solution were added. The solution was sonicated for 4.5 hours at a temperature of 30 °C. After sonication, in order to precipitate the solubilized particles, the solution was washed with 2-propanol (99%, Fisher Scientific). The resulting precipitated particles were dried and pumped into a glovebox. Finally, the ODTMS-$(Ga_{1-x}Zn_x)(N_{1-x}O_x)$ nanocrystals were re-dissolved in toluene. Particles were kept airfree for future use.

2.1.6 Electron Scavenger Experiment Sample Preparation

Methylene blue (MB, ≥82%, Sigma Aldrich) was used as an electron scavenger in solution with $(Ga_{1-x}Zn_x)(N_{1-x}O_x)$. A small amount (<1 mg) of methylene blue powder was dropped into the

toluene solution of oxynitride particles and sonicated for a few minutes. The solution was placed in an airfree cuvette with a Kontes valve for transient absorption studies.

2.1.7 Ag-TiO_2 Film Synthesis

Mesoporous TiO_2 films were synthesized using the Evaporation Induced Self Assembly (EISA) technique. During a typical synthesis, 1 g of Pluronic® P-123, used as structuring agent, is added to a solution of TBT (3.4 g), HCl (3.2 g) and EtOH (12 g). The molar ratio of Ti:H_2O: HCl is 1:11.2:3.22. Films are then deposited by a dip-coating method on quartz substrates, at 2 $mm.s^{-1}$. The films are aged under ambient conditions (T=23°C, RH=40-50%) for 24 h then calcinated at 400°C during 4 h, with a heating ramp of $1°C.min^{-1}$.

In order to form silver NPs inside the mesoporous titania film, an impregnation method is used. Briefly, an ammonia silver solution is prepared by adding ammonium hydroxide solution (25%) to a silver nitrate aqueous solution (50 mM), until a clear solution is obtained. The mesoporous films are immersed in this solution for 15 minutes. Then the silver ions are chemically reduced using formaldehyde. Films are immersed for 15 min at 80°C in a solution of 12 mM of formaldehyde in ethanol. The resulting films are washed with water and stored away from light.

2.2 Spectroscopy

2.2.1 Diffuse Reflectance Spectroscopy

Diffuse reflectance (DR) spectra were recorded using a Shimadzu UV-3600 spectrophotometer and an Agilent Cary 60 spectrophotometer, both equipped with an integrating sphere. For the Shimadzu UV-3600 spectrophotometer, $BaSO_4$ was used as a reflectance reference material and in the Agilent Cary 60 spectrophotometer a 100 % reflectance standard Halon puck was used as the reference. The acquired spectra and their reference spectra were used to convert to Kubelka-Munk plots using the Kubelka-Munk equation $[F(R_\infty = (1 - R_\infty)^2/2R_\infty;\ 2R_\infty =$

$R_{sample}/R_{reference}$]. Samples for DR measurements were prepared by suspending the solid powder in ethanol and then drop casting onto a glass slide.

2.2.2 Ultraviolet-Visible Spectroscopy

Ultraviolet-Visible Spectroscopy was conducted using an Agilent 8453 UV-Vis spectrophotometer and an Agilent Cary 60 spectrophotometer. Samples were measured in 1 cm quartz cuvettes or 2 mm airfree quartz cuvettes. Film samples were held in the absorption beam path for measurements.

2.2.3 Transient Absorption (TA) Spectroscopy

Femtosecond TA spectroscopy measurements were obtained using a regeneratively amplified Ti:sapphire laser (Solstice, Spectra-Physics, 800 nm, 100 fs, 1 kHz, 3.5 mJ/pulse), an optical parametric amplifier (TOPAS-C, Light Conversion), and the HELIOS spectrometer (Ultrafast Systems, LLC), for short timescale (100 fs – 3 ns) measurements. A fraction of the Solstice output (800 nm) was used to pump the TOPAS-C in order to produce the desired pump wavelength for exciting the sample (340 nm for $(Ga_{1-x}Zn_x)(N_{1-x}O_x)$ measurements and 300 nm and 450 nm for Ag-TiO_2 measurements). The pump pulse was focused through the sample after being directed through various neutral density filters, a depolarizer, and a synchronized 500 Hz chopper. The other fraction of the 800 nm Solstice output was used to generate the white-light continuum to be used for absorbance measurement as the probe pulse. A CaF_2 crystal was used to generate the white light continuum from 340-700 nm in some experiments, and a sapphire plate to generate a continuum from 450-800 nm in other experiments. Each respective use of white light probe will be specified in the Chapters to follow. The probe beam was focused onto the sample and overlapped with the pump pulse and the pump-probe time delay was controlled using a motorized

delay stage. Finally, the probe beam was detected by a CMOS sensor with and without excitation which resulted in the change in absorbance (ΔA).

Measurements for other experiments which will be specified in the next Chapters were also made from 100 fs – 8 ns using a HELIOS spectrometer (Ultrafast Systems, LLC) with a longer delay stage and a sapphire crystal to generate a white light continuum probe pulse (450 nm-800 nm) and a sapphire crystal was used to generate a near infrared (NIR) probe pulse (800-1600 nm). Signals in this spectrometer were also detected using a CMOS sensor and resulted in data represented as ΔA.

Long timescale TA measurements of 0.3 ns to 100 μs were performed using an EOS spectrometer (Ultrafast Systems, LLC). The pump pulse was again generated as described above, however was not chopped as it was using the HELIOS spectrometer. The white light probe beam (400-900 nm, 0.3 ns, 2 kHz) was generated using a Nd:YAG laser that was focused into a photonic crystal fiber. In the EOS spectrometer, the delay between the pump and the probe beams was controlled by an electronic delay generator (CNT-90, Pendulum Instruments). The probe beam was detected using the CMOS sensor.

All TA experiments were conducted at room temperature. The TA experiments for $(Ga_{1-x}Zn_x)(N_{1-x}O_x)$ in toluene were all carried out in an airfree (sealed under Ar) 2 mm quartz cuvette with Kontes valves. The samples were constantly stirred by a stir bar using a magnetic stirrer. All of the TA spectra were background subtracted, chirp-corrected using the instrument response function (IRF) determined from TA data of toluene, and time zero corrected. TA experiments for Ag-TiO_2 films were conducted in air. The film was checked for degradation between sample runs. All data was background subtracted and time zero corrected.

2.2.4 Photoluminescence Spectroscopy

Photoluminescence spectra were obtained using a Hitachi F-2500 Fluorescence Spectrophotometer with an excitation wavelength of 340 nm using 5 nm slit width, 700 V PMT voltage, and 0.08 s response.

2.3 ICP-OES

To determine the x value in $(Ga_{1-x}Zn_x)(N_{1-x}O_x)$, elemental analysis by Inductively coupled plasma-optical emission spectrometry) (ICP-OES) for Zn and Ga was conducted using ARL 3410+ inductively coupled optical emission spectrometer. Powder samples were prepared by placing a small spatula tip of powder in a vial. Solubilized liquid samples were prepared by measuring a 2 mL aliquot of known absorbance value from UV-VIS spectroscopy and then evaporating off the sample. All samples were digested in nitric acid prior to measurement. Samples were all analyzed in triplicate.

2.4 Transmission Electron Microscopy (TEM)

For transmission electron microscopy studies, the powder samples were prepared by dropping dilute suspensions of nanoparticles onto TEM grids. Solubilized samples in toluene were dropped directly onto the grids. TEM grids used were lacey carbon films supported by copper 300 mesh grids.

Low resolution TEM images were obtained using a FEI Tecnai Spirit BioTwin operating at 120kV. The instrument was equipped with a side-mount AMT (2k x 2k) CCD. Images were analyzed using ImageJ software.[44]

High resolution TEM (HRTEM) images were obtained using a FEI Technai F20 FEG TEM operating at 200 kV. This instrument was equipped with a bottom-mounted 4k x 4k Gatan

Ultrascan 895 CCD camera. HRTEM images were also acquired at 300 keV using FEI Titan Themis (S)TEM equipped with 4k x 4k Ceta camera.

2.5 X-ray Diffraction

Powder X-ray Diffraction (XRD) patterns for $(Ga_{1-x}Zn_x)(N_{1-x}O_x)$ were collected on a Rigaku Dmax diffractometer using a Cu Kα radiation source (λ=0.1540562 nm). Solid samples were prepared by dispersion in ethanol and drop casting onto a glass slide while heating. Solubilized samples were dropped directly onto the glass slide and heated to evaporate off the toluene. For preparation of the solubilized samples, the drop was followed using Ar through a needle in order to concentrate the sample to a small point on the glass slide. The XRD patterns were recorded from 2θ of 25 to 85° with a step size of 0.02°.

Chapter 3. Optical Properties of $(Ga_{1-x}Zn_x)(N_{1-x}O_x)$ Nanoparticles

3.1 Introduction

$(Ga_{1-x}Zn_x)(N_{1-x}O_x)$ is a solid solution of ZnO and GaN with an intriguing visible bandgap that is tunable with composition. While ZnO and GaN, the parent materials of $(Ga_{1-x}Zn_x)(N_{1-x}O_x)$ absorb ultraviolet (UV) light, the solid solution absorbs visible light. Originally, this material was synthesized in its bulk form and shown to have water splitting capability.[11,12,15,17,45] However, the quantum efficiency of water-splitting has never exceeded 20%.[23] Our group successfully synthesized $(Ga_{1-x}Zn_x)(N_{1-x}O_x)$ on the nanoscale as a means to improve catalytic activity.[25] Later, we discovered that the solid state synthesis method used to produce these particles on the nanoscale results in $(Ga_{1-x}Zn_x)(N_{1-x}O_x)$ particles with a heterogeneous distribution, with Zn and O localized in the center of the particle and Ga and N on the edge, when synthesized at 650 °C.[34] We also found that a homogenous distribution with all four composing elements evenly distributed around the particle results when particles are synthesized at 800 °C.[34] The optical properties of these materials are still not completely understood.

Theoretical predictions about the nature of visible absorption predict that orbital repulsion resulting from all four elements in the same crystal lattice results in a shift upwards of the valence band, narrowing the bandgap.[12,46-50] It has also been predicted that $(Ga_{1-x}Zn_x)(N_{1-x}O_x)$ is a direct bandgap absorber.[51,52] All of these properties are important for understanding how $(Ga_{1-x}Zn_x)(N_{1-x}O_x)$ behaves as a light absorber, and useful for future material synthesis.

In this chapter, we focus on studying the optical properties in $(Ga_{1-x}Zn_x)(N_{1-x}O_x)$ nanoparticles. In particular, we studied $(Ga_{1-x}Zn_x)(N_{1-x}O_x)$ synthesized at 650 °C and 800 °C to compare optical properties in the heterogeneous versus homogeneous particles, respectively.

Using diffuse reflectance spectroscopy to measure the absorbance of the particles and a band fluctuations model to determine the bandgap and Urbach energies in the particles, we sought to understand what differences in properties result from different elemental distributions.

3.2 Materials and Methods

3.2.1 Chemicals

Gallium acetylacetonate ($Ga(acac)_3$, 99.99%), zinc acetylacetonate hydrate ($Zn(acac)_2$, 99.995%), oleic acid (≥99.0%), oleylamine (70%), 1,2-hexadecanediol (90%), benzyl ether (98%), 3-mercaptopropionic acid (3-MPA, ≥99.0%), zinc chloride ($ZnCl_2$, ≥98%), tetramethylammonium hydroxide pentahydrate (≥97%), hexane (99%), toluene (99.5%), were purchased from SigmaAldrich. Sodium hydroxide (NaOH pellets, 99.3%), 2-propanol (99.9%) and methanol (99.9%) were purchased from Fisher Scientific. Ammonia (99.99%) was purchased from Airgas. 1,2-Ethanediol (99.8%) was purchased from Macron Fine Chemicals. Ethanol (95%) was purchased from Decon Laboratories. All chemicals used for the synthesis were purchased commercially and used without additional purification.

3.2.2 $(Ga_{1-x}Zn_x)(N_{1-x}O_x)$ Nanoparticle Synthesis

$(Ga_{1-x}Zn_x)(N_{1-x}O_x)$ nanocrystals were synthesized as previously published and described in Chapter 2.[25,34]

3.3 Characterization

3.3.1 Transmission Electron Microscopy

Elemental mapping using energy-dispersive X-ray spectroscopy in a scanning transmission electron microscope (STEM-EDS) was performed on FEI Titan and FEI Talos F200X microscopes which were equipped with a Super-X EDS system (four silicon drift detectors, SDDs), and were

operated at 80 and 200 kV, respectively. Analysis of STEM-EDS data was performed using Bruker Esprit software.

3.3.2 Diffuse Reflectance Spectroscopy

Diffuse reflectance (DR) spectra were recorded using a Shimadzu UV-3600 spectrophotometer and an Agilent Cary 60 spectrophotometer, both equipped with an integrating sphere. The presented absorbance spectra were acquired by converting the reflectance data to Kubelka-Munk plots using the Kubelka-Munk equation [$F(R_\infty = (1 - R_\infty)^2/2R_\infty;\ 2R_\infty =$ $R_{sample}/R_{reference}$], where $R_{reference}$ is measured using a 100% reflectance standard.

3.3.3 Photoluminescence Spectroscopy

Photoluminescence spectra were obtained using a Hitachi F-2500 Fluorescence Spectrophotometer with an excitation wavelength of 340 nm.

3.4 Results and Discussion

Samples of $(Ga_{1-x}Zn_x)(N_{1-x}O_x)$ nanoparticles synthesized at 650 °C have been previously studied and shown to have a considerable degree of compositional heterogeneity.[25,26,34] In particular, the four elements composing $(Ga_{1-x}Zn_x)(N_{1-x}O_x)$ nanoparticles were found to be unevenly distributed throughout the particles, where Ga and N are concentrated towards the edges of the particles, and Zn and O towards the center.[34] As the reaction temperature was increased to 800 °C, homogeneity in the particles increased, with all four elements being evenly distributed throughout the particles. This is shown in energy dispersive X-ray spectroscopy (EDS) elemental maps in Figure 3.1, for samples with x equal to approximately 0.35.[34] In the elemental maps, the elemental distributions are apparent, with particles synthesized at 800 °C having a more homogenous distribution of the elements, while the particles synthesized at 650 °C have a more “core-shell” like structure. Here,

we seek to understand how the optical properties in $(Ga_{1-x}Zn_x)(N_{1-x}O_x)$ nanoparticles are influenced by these differences in elemental distribution.

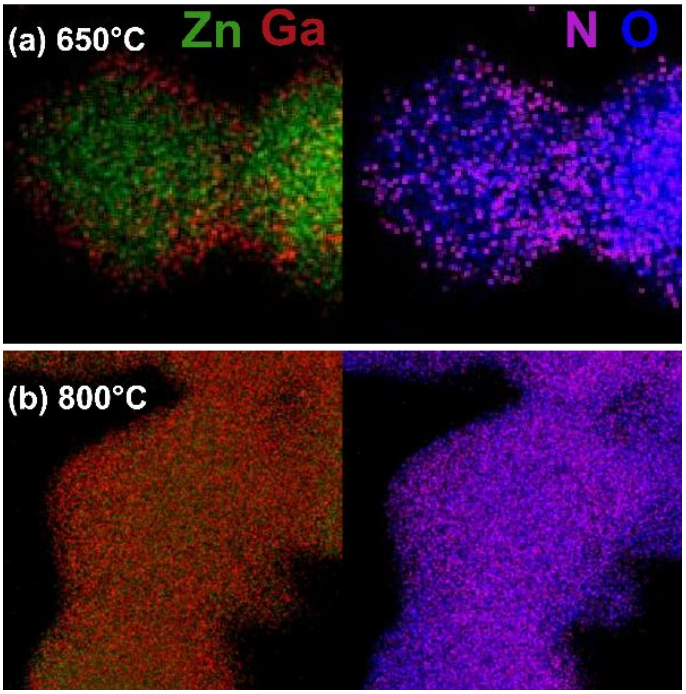

Figure 3.1. EDS elemental maps of $(Ga_{1-x}Zn_x)(N_{1-x}O_x)$ nanoparticles synthesized at 650 °C (a) and 800 °C (b) with x value approximately equal to 0.35. Adapted from *ACS Nano* **2017**, *11*, 8401-8412. © 2017 ACS Nano.

3.4.1 Steady-State Absorption Measurements

Here, we analyze the optical properties of the homogenous and heterogeneous nanoparticles using steady-state measurements of the solid samples. As synthesized, particles are in their solid powder form. Diffuse reflectance measurements were used in order to study the absorbance spectra of the particles obtained directly from synthesis in their powder form.

First, understanding the excited state behavior led us to propose a possible band diagram for $(Ga_{1-x}Zn_x)(N_{1-x}O_x)$ nanoparticles. As previously published, transient absorption analysis of a Zn rich sample with x=0.73 shows that the decay kinetics of the visible and UV-bleach are similar and thus share an electronic state.[35] The proposed band diagram for a Zn rich $(Ga_{1-x}Zn_x)(N_{1-x}O_x)$

is shown in Figure 3.2, where the valence band edge is composed of orbitals that result from the mixing of GaN and ZnO orbitals, while the conduction band edge arises from ZnO orbitals. This also agrees with theoretical predictions, where the visible absorption originates from a transition between a valence band that arises from mixing ZnO and GaN, and a conduction band that contains mostly Zn and O orbitals.[27,29,31] It is possible that a Ga rich particle would be composed of a conduction band that contains mostly Ga and N orbitals. This has also been theoretically explored.[29] The current proposed band diagram assumes a direct transition in $(Ga_{1-x}Zn_x)(N_{1-x}O_x)$. Spectral shape analyses have also suggested that $(Ga_{1-x}Zn_x)(N_{1-x}O_x)$ is a direct bandgap semiconductor.[51,52]

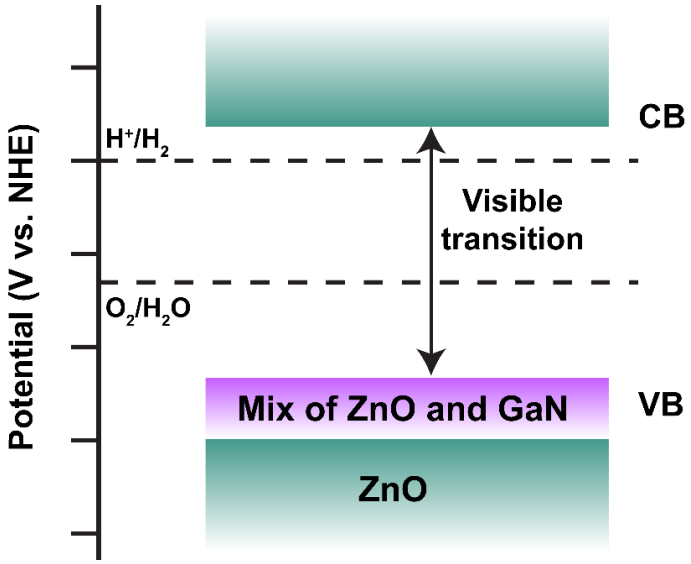

Figure 3.2. Proposed band diagram for a $(Ga_{1-x}Zn_x)(N_{1-x}O_x)$ nanoparticles with high x value (x>0.5) where the valence band (VB) is composed of ZnO orbitals and a mix of ZnO and GaN orbitals, and the conduction band (CB) orbitals are ZnO-like.

We had previously reported that $(Ga_{1-x}Zn_x)(N_{1-x}O_x)$ particles behave like direct bandgap semiconductors.[35] Both theoretical results using spectral shape analysis, and experimental values of molar absorptivity (ε) and absorption coefficient (α) led us to this conclusion.[29,53] $(Ga_{1-x}Zn_x)(N_{1-x}O_x)$ nanoparticles have large absorption coefficients and molar absorptivities. For example, sample $(Ga_{0.6}Zn_{0.4})(N_{0.6}O_{0.4})$ which is studied extensively using transient absorption (TA)

spectroscopy in Chapter 4, has an ε value of about 1,300 cm^{-1} M_{cation}^{-1} at 340 nm and an absorption coefficient of about $2.0x10^5$ cm^{-1}. The strength of absorption is comparable to that in bulk GaAs and theoretically predicted values for the direct bandgap absorption in $(Ga_{1-x}Zn_x)(N_{1-x}O_x)$.[54] Therefore, we think that there must be a direct transition in this material, rather than indirect or impurity-based transitions. However, upon further investigation, it remained possible that we could observe an indirect transition below the direct transition.

One method used to calculate bandgaps in semiconductors, from absorption spectroscopy, utilizes the Tauc equation given in equation (3.1), where α is the absorption coefficient, hν is the photon energy, n is a value of 2 or ½, A is a proportionality constant, and E_g is the bandgap energy.

$$(\alpha h\nu)^n = A\,(h\nu - E_g) \tag{3.1}$$

This equation assumes parabolic band dispersion to express the energy dependence of optical transition strengths. Values of n equal to 2 and ½, indicate whether the transition is direct or indirect, respectively. As a result, when plotting $(\alpha h\nu)^2$ and $(\alpha h\nu)^{1/2}$ vs hν, their linearity can determine the nature of transitions. Using the Kubelka-Munk equation, diffuse reflectance spectra collected for samples with x=0.38 (650 °C) and x=0.35 (800 °C) were transformed to absorption spectra. Using the absorption spectra, Tauc plots were constructed assuming direct and indirect absorption and are shown in Figure 3.3. Both the $(ah\nu)^2$ and the $(ah\nu)^{1/2}$ dependence on energy are linear. In fact, the $(ah\nu)^{1/2}$ plot appears to have a more distinct linear region than the $(ah\nu)^2$. This could indicate that $(Ga_{1-x}Zn_x)(N_{1-x}O_x)$ has an indirect transition, as well as a direct.

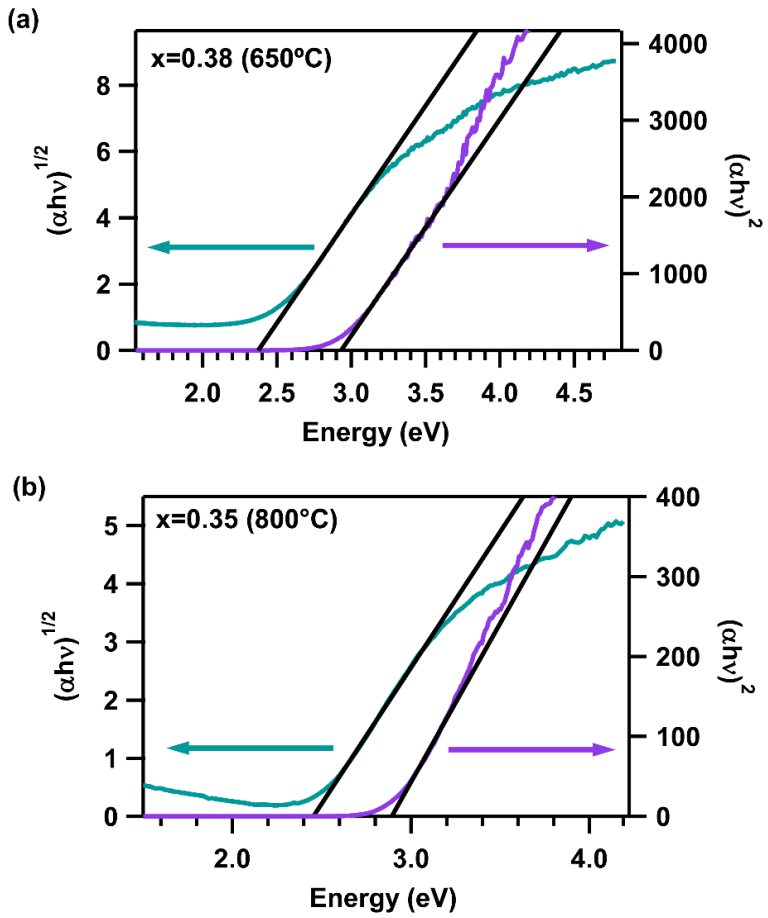

Figure 3.3. Tauc plots with linear fits for a direct $(\alpha h\nu)^2$ and indirect $(ah\nu)^{1/2}$ bandgap in $(Ga_{1-x}Zn_x)(N_{1-x}O_x)$ with x=0.38 synthesized at 650 °C (a) and with x=0.35 synthesized at 800 °C.

Linear fits were performed on the Tauc plot spectra, as indicated in Figure 3.3, for samples with varying composition and elemental distribution. Such linear fits yield the bandgap values for the direct and indirect transitions and are shown in Figure 3.3. From Figure 3.4, it is clear that in both the homogenous and heterogeneous samples (650 vs. 800 °C), the indirect transition is about 370 meV below the direct transition. We know that the direct transition must be responsible for the large absorption coefficient of the material, however, we do not have clear evidence whether there is in fact an indirect transition below it. We also note that for both bandgap measurements, we see the trend of decreasing bandgap with increasing x value, which has been previously reported for various $(Ga_{1-x}Zn_x)(N_{1-x}O_x)$ samples.[25,34] Theoretical predictions do not indicate the

presence of an indirect bandgap in $(Ga_{1-x}Zn_x)(N_{1-x}O_x)$, however, we pursued to understand if this was a possibility.

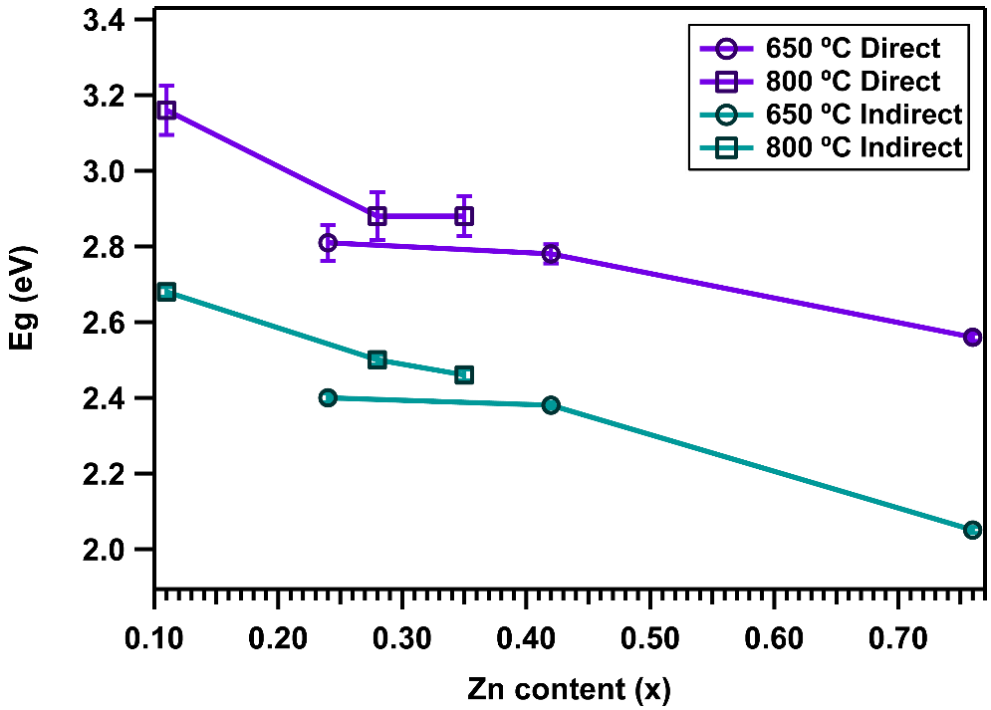

Figure 3.4. Values for direct (purple trace) and indirect (blue trace) bandgap obtained from Tauc plot fits of samples with various x values at 650 °C (circle markers) and 800 °C (square markers).

$(Ga_{1-x}Zn_x)(N_{1-x}O_x)$ particles exhibit negligible photoluminescence, as shown in Figure 3.5, where the particles in solution have less PL response than constituents in solution, including ODTMS and butylamine, which are used in the solubilization procedure. In a direct gap semiconductor, radiative recombination is expected, while in an indirect gap semiconductor, where emission requires a third, momentum conserving particle to be involved, the luminescence yield is smaller.[55] Relaxation in indirect semiconductors is usually dominated by nonradiative processes. However, as we will discuss in Chapters 4 and 5, we found that the nonradiative process of Auger recombination occurs in $(Ga_{1-x}Zn_x)(N_{1-x}O_x)$. In addition, we observe long-lived average carrier lifetimes, $<\tau>$, in $(Ga_{1-x}Zn_x)(N_{1-x}O_x)$, as was previously published for $(Ga_{0.73}Zn_{0.27})(N_{0.73}O_{0.27})$ and will be reported for sample $(Ga_{0.6}Zn_{0.4})(N_{0.6}O_{0.4})$ in Chapter 4.[35] The lifetime of carriers in indirect

materials is expected to be between 1 μs and many μs, while direct bandgap materials exhibit much faster recombination lifetimes in the sub-ns range.[55] This could potentially support the claim of an indirect transition.

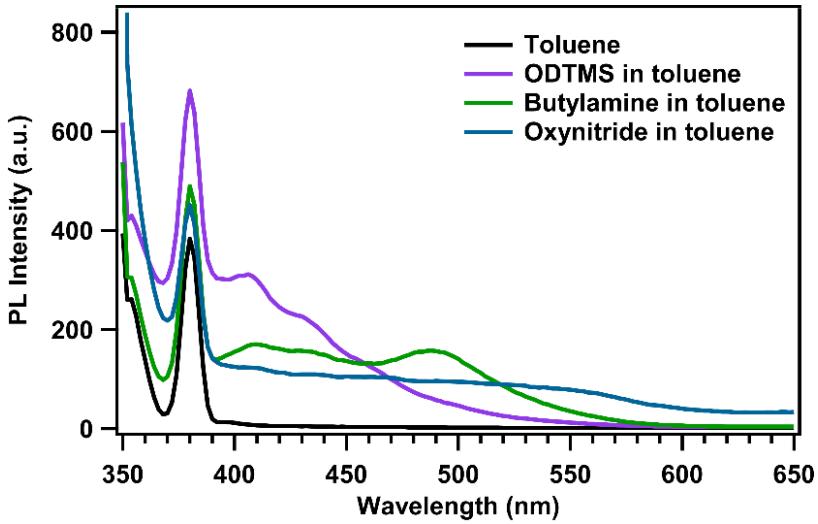

Figure 3.5. Photoluminescence (PL) spectra of $(Ga_{1-x}Zn_x)(N_{1-x}O_x)$ (blue trace) in toluene compared to other entities in solution, including ODTMS (purple trace) and butylamine (green trace). Sample was excited with 340 nm and peak at ~380 nm^{-1} is due to Raman scattering.

Given the Tauc plots and excited state decay information, we cannot conclusively confirm the presence of an indirect transition in the $(Ga_{1-x}Zn_x)(N_{1-x}O_x)$. It is often difficult to use a Tauc plot for determining the bandgap and nature of transitions. Finding an arbitrary linear region, in particular, can be difficult due to the possible overlap of the direct bandgap region with disorder induced localized states and extended states.[56,57] The typical shape of an absorption spectrum of a disordered system has three regions.[55] The first region is where the absorption is weak and is caused by impurities in an alloy or amorphous semiconductor, or free carrier absorption. The second is the Urbach tail region where the absorption coefficient increases exponentially as photon energy increases and can be attributed to inhomogeneity, defects, and disorder. Finally, the third region is the Tauc regime, where the absorption is comprised of transitions into extended states. Various alloy semiconductors such as $ZnSe_{1-x}Te_x$ and $CdS_{1-x}Se_x$ exhibit absorption spectra with

these three regions.[55] $(Ga_{1-x}Zn_x)(N_{1-x}O_x)$ also exhibit such behavior. Figure 3.6 shows the Kubelka Munk transformed diffuse reflectance spectrum of sample x=0.38 synthesized at 650 °C. The free carrier absorption, Urbach tail, and direct bandgap transition are labeled. From this spectrum, it is clear that the Urbach tail region and direct bandgap transition, or Tauc region, overlap. Mainly, it is not entirely clear where the Tauc region begins. Therefore, it is useful to use a different model, than to simply fit the linear region in a Tauc plot, in order to determine the bandgap and nature of the transition.

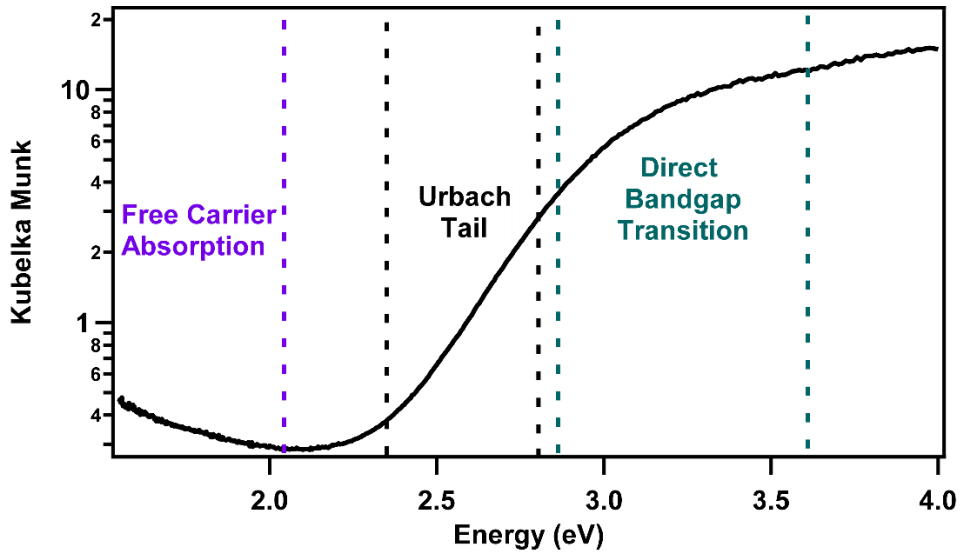

Figure 3.6. Diffuse reflectance transformed Kubelka Munk plot of $(Ga_{1-x}Zn_x)(N_{1-x}O_x)$ with x= 0.38 synthesized at 650 °C. The free carrier absorption, Urbach tail, and Direct Bandgap (Tauc) regions are labeled.

A model used by Guerra *et al* is shown in equation (3.2).[56] This model, called the band fluctuations model, includes both a direct bandgap fit to absorbance data, as well as a fit to the Urbach tail, which is present in our samples. In this model, α_0 contains the joint density of states term, and the electronic transition matrix element, β is the Urbach slope which defines how large the band fluctuations are (the reciprocal of β is taken as E_u or the Urbach energy), E_g is the direct bandgap, and $Li_{1/2}$ is the ½ order polylogarithm function.[56,58,59]

$$\alpha(\hbar\omega) = -\frac{\alpha_0}{\hbar\omega}\sqrt{\frac{\pi}{\beta}}\,\mathrm{Li}_{\frac{1}{2}}(-e^{\beta(\hbar\omega-E_g)}) \quad (3.2)$$

Using this band fluctuations model to fit absorbance data of various $(Ga_{1-x}Zn_x)(N_{1-x}O_x)$ samples, we can define the bandgap energy of the direct bandgap and the Urbach energy.

Figure 3.7 shows fits to equation (3.2) on diffuse reflectance transformed Kubelka Munk plots for samples with various x values, synthesized at 650 °C. These results clearly fit in the Urbach and Tauc regime. It is evident that as the x value, or ZnO content, increases, there is a second region in the spectrum that cannot be fit using this expression. This second transition in the UV region is a result of the inhomogeneity and more Zn content in the 650 °C synthesized samples. The second transition has ZnO band edge character. In order to understand how the inhomogeneity in $(Ga_{1-x}Zn_x)(N_{1-x}O_x)$ affects the Urbach energies, we also used the band fluctuations model to fit the absorbance of homogenous samples synthesized at 800 °C. The results are shown in Figure 3.8, where the band fluctuations model fits most compositions in the full spectral window. This is different from the 650 °C samples, where we observed the distinct UV transition. While it is difficult to directly compare the samples, because high Zn content compositions are not achievable at 800 °C, it is clear that the UV transition is not as prevalent in the homogeneous samples.

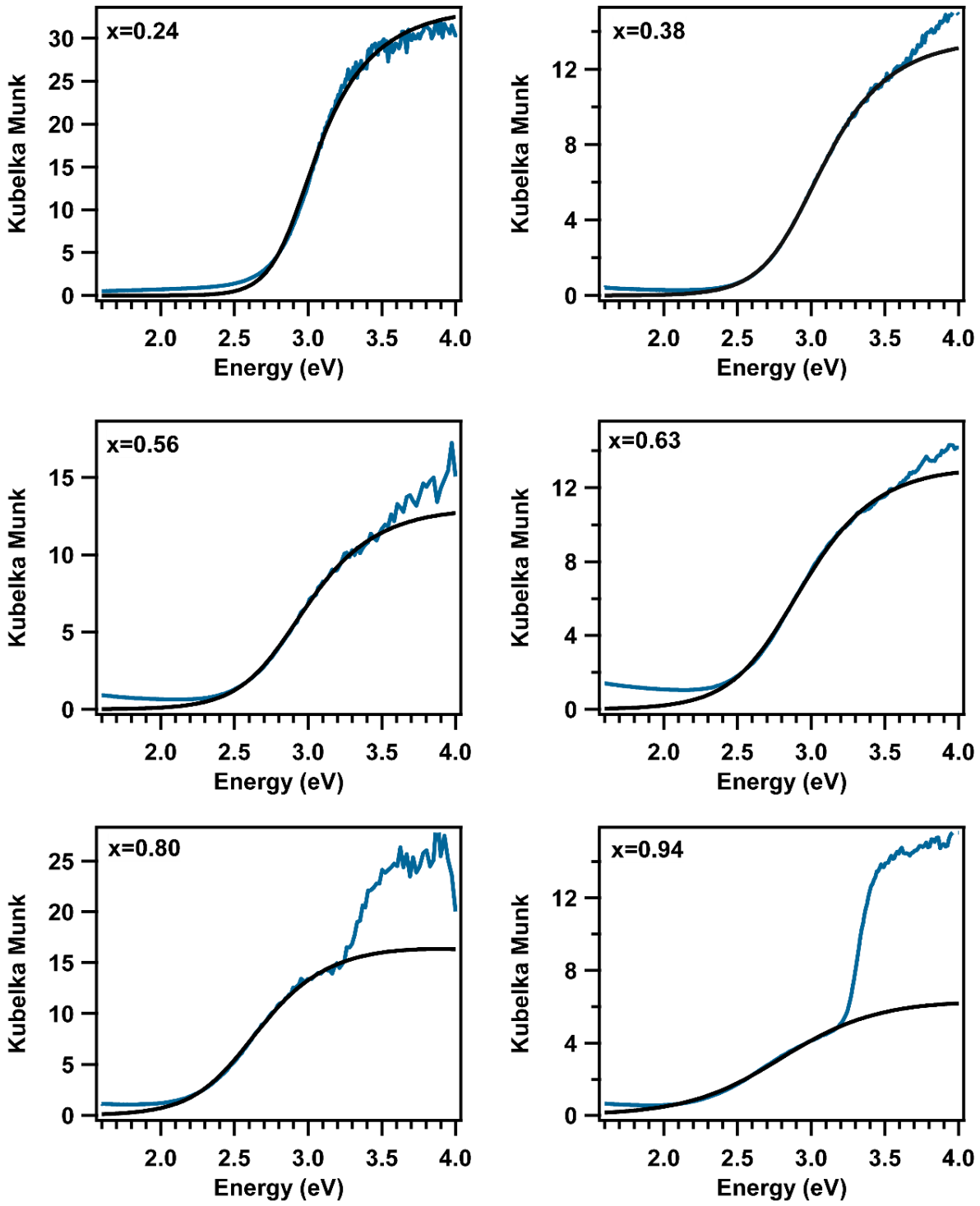

Figure 3.7. Diffuse reflectance transformed Kubelka Munk plots of various $(Ga_{1-x}Zn_x)(N_{1-x}O_x)$ nanoparticles with different x values synthesized at 650 °C. Fits to band fluctuations model given in equation (3.2) are shown in black and were performed below the UV (ZnO) transition region.

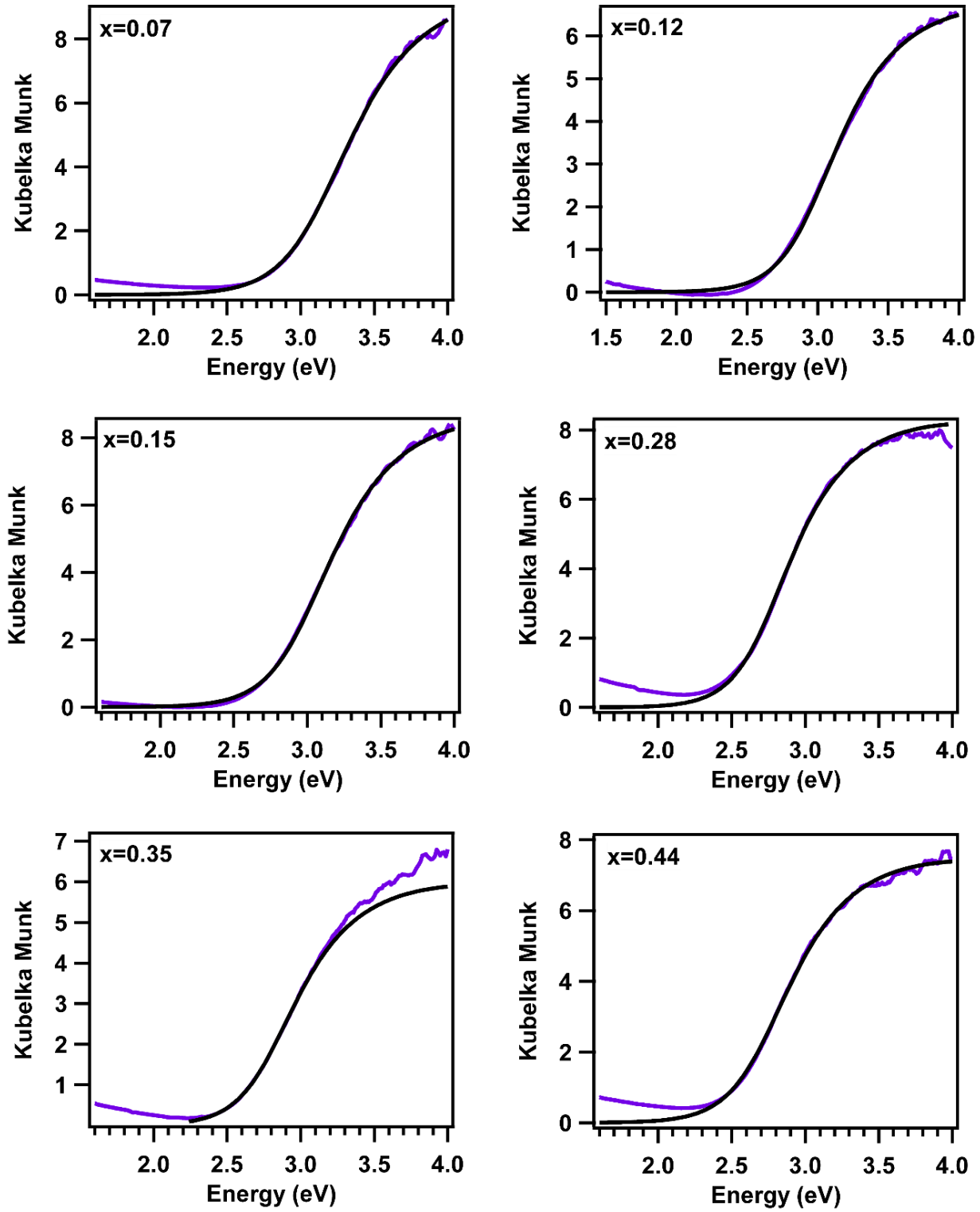

Figure 3.8. Diffuse reflectance transformed Kubelka Munk plots of various $(Ga_{1-x}Zn_x)(N_{1-x}O_x)$ nanoparticles with different x values synthesized at 800 °C. Fits to band fluctuations model given in equation (3.2) are shown in black.

The values obtained from fits to the band fluctuations model (equation (3.2)) for bandgap energy (E_g) and Urbach energy (E_u) were plotted in Figures 3.9 and 3.10, respectively. We find that the bandgap values exhibit a similar trend, that has been previously observed, where the bandgap decreases with increasing Zn content (x value).[25,34] The Urbach energies for homogenous samples synthesized at 800 °C seem to remain similar as x value increases and have an average Urbach energy of 0.16 eV. The samples synthesized at 650°C have a more prominent trend in Urbach energies, where the Urbach energy increases with increasing x value. The average Urbach energy for these samples is 0.18 eV. Values of 160 meV and 180 meV for homogenous and heterogeneous samples, respectively, are on the order of what we would expect from an alloyed system. Very large Urbach energies of 100s of meV are present in alloys such as InGaN.[30,32] On average, there does not appear to be a significant difference between the Urbach energies for homogenous vs. heterogeneous samples. However, the small increase in the Urbach tail for the heterogeneous samples, with increasing Zn content, could be a result of greater inhomogeneity as the ZnO content increases as well as an increase in crystal lattice strain. Therefore, we can conclude that the Urbach tail observed in both samples is due to disorder and defects in the particles and the increase in the Urbach energy observed for higher Zn content samples is due to the heterogeneity in the elemental distribution in the particles.

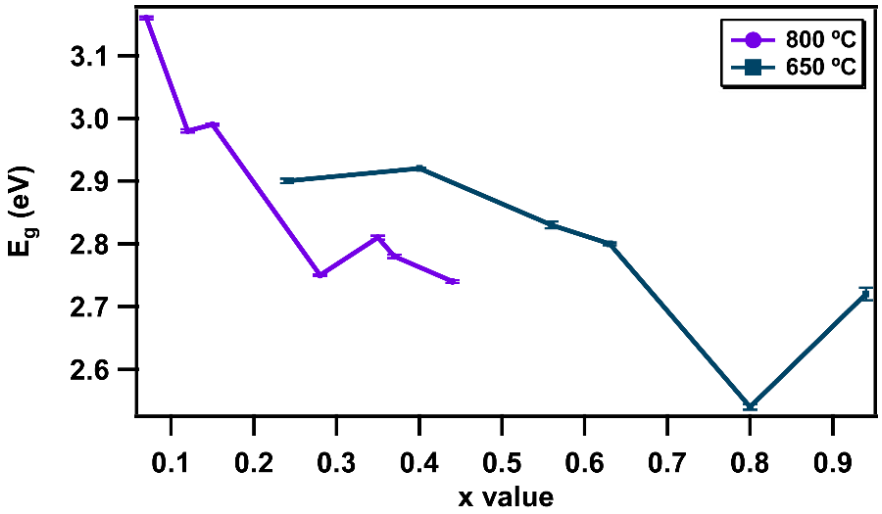

Figure 3.9. Trends in bandgap (E_g) values at various x values in $(Ga_{1-x}Zn_x)(N_{1-x}O_x)$ synthesized at 650 °C (blue squares) and 800 °C (purple circles). Error bars show error obtained from fits to band fluctuations model (equation (3.2)).

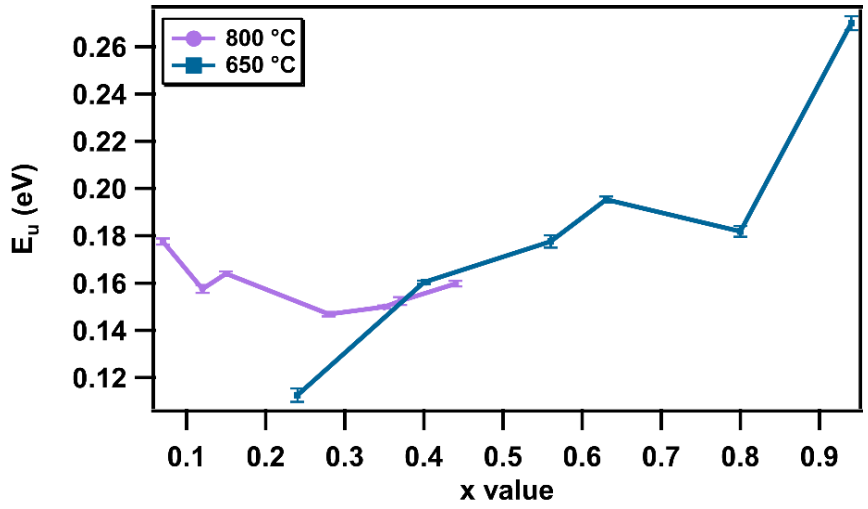

Figure 3.10. Trends in Urbach energies (E_u) at various x values in $(Ga_{1-x}Zn_x)(N_{1-x}O_x)$ synthesized at 650 °C (blue squares) and 800 °C (purple circles). Error bars show error obtained from fits to band fluctuations model (equation (3.2)).

3.5 Conclusions

Understanding optical properties of complex materials is important for their use in light absorption applications. $(Ga_{1-x}Zn_x)(N_{1-x}O_x)$, a solid solution of GaN and ZnO, has unique optical properties relevant to solar fuel generation. $(Ga_{1-x}Zn_x)(N_{1-x}O_x)$ nanoparticle optical properties were explored using various spectroscopic techniques. Upon analysis of Tauc plots, created for a direct

and indirect transition, it was not clear whether only a direct transition or both a direct and indirect transition occur. Perhaps an experimental technique, such as resonant inelastic X-ray scattering, could determine whether there is in fact an indirect transition below the strong direct transition, such as that observed in monoclinic $BiVO_4$.[60]

We also fit diffuse reflectance transformed Kubelka Munk plots to a band fluctuations model, where the transition is assumed to have both an Urbach tail and direct bandgap. The fits matched well with experimental data, so perhaps there is only a direct bandgap along with defect states, rather than an indirect bandgap. We determined that Urbach energies in $(Ga_{1-x}Zn_x)(N_{1-x}O_x)$ nanoparticles are similar for samples with different elemental distributions. However, particles with higher Zn content had larger Urbach energies, which could be explained by the increase in heterogeneity as more ZnO is added to the particles. Large Urbach energies of 100s of meV in both homogeneous and heterogeneous samples led to the conclusion that the Urbach tail is largely dominated by defects and disorder, which must be present in both types of particles.

Chapter 4. Excited-State Dynamics of $(Ga_{1-x}Zn_x)(N_{1-x}O_x)$ Nanocrystals

4.1 Introduction

Direct solar fuel generation utilizing semiconductor light absorbers is a promising strategy to address modern issues in energy production.[9,61] Unfortunately, suitable semiconductors for fuel production are rare, as they must combine properties of visible light absorption, resistance to photooxidation, catalytically suitable band potentials, and long-lived excited states.[62,63] Such requirements have revealed the need for new semiconductors with multinary compositions to control material stability and band gap.[64,65] However, many of the excited-state properties of such materials are still not well understood.[51] It is necessary to gain information about the excited-state behavior of multinary semiconductors in order to enhance their performance as viable sources of solar energy harvesters.

One intriguing material which meets the criteria for a strong candidate for solar fuel generation is $(Ga_{1-x}Zn_x)(N_{1-x}O_x)$. Nanocrystals of $(Ga_{1-x}Zn_x)(N_{1-x}O_x)$ have strong visible absorption, comparable to direct bandgap semiconductors, which can be tuned based on composition.[25,26,35] In other words, the x value, or ZnO content, determines the bandgap. $(Ga_{1-x}Zn_x)(N_{1-x}O_x)$ has been shown to be capable of splitting water into H_2 and O_2 under visible light illumination.[11-22,66] However, the quantum efficiency of water-splitting has never exceeded 20%, indicating significant energy-loss pathways present within the material.[23] It is important to learn what limits water-splitting quantum efficiency, whether it is a result of properties inherent to the material, such as fast carrier lifetimes, or properties such as defects which could potentially be controlled through synthetic methods. In order for water-splitting to occur in the $(Ga_{1-x}Zn_x)(N_{1-}$

$_xO_x$) nanocrystals upon excitation, the electron and hole need to be transferred to catalytic sites to perform their respective half reactions, where the electron produces H_2 and the hole, O_2. To have an efficient photocatalyst for water-splitting, the electron and hole transfer need to compete with fast recombination processes. Understanding the excited-state decay pathways available to these nanocrystals gives further insight into its ability to be used as a photocatalyst for water-splitting. In order to gain insight into why the $(Ga_{1-x}Zn_x)(N_{1-x}O_x)$ have such strong visible absorption, but poor photochemical quantum yield, it is necessary to understand their carrier dynamics. Transient absorption (TA) spectroscopy can be used to study the carrier dynamics, where the excited-state decay kinetics can be monitored upon excitation. By monitoring the behavior of excited-state carriers in $(Ga_{1-x}Zn_x)(N_{1-x}O_x)$, we can better understand how the electron and hole could be used for solar water-splitting.

Here, we report the excited-state dynamics of $(Ga_{1-x}Zn_x)(N_{1-x}O_x)$ nanocrystals with x=0.4. Using transient absorption spectroscopy, we monitor the decay kinetics of the visible absorption feature. We reveal a power dependent carrier filling which allowed us to explore properties about $(Ga_{1-x}Zn_x)(N_{1-x}O_x)$ nanocrystals that were previously unknown, including the reduced effective mass of the electron and hole. Furthermore, we explain the carrier decay kinetics using a model for recombination for short and long-lived decay components and determine recombination rate constants for trap mediated and Auger recombination. We believe that by studying the excited-state decay dynamics in this material, we can gain further insight into design of new and efficient materials for solar fuel generation.

4.2 Materials and Methods

4.2.1 Chemicals

Zinc acetylacetonate hydrate ($Zn(acac)_2$, 99.995%), gallium acetylacetonate ($Ga(acac)_3$, 99.99%], 1,2-hexadecanediol (90%), oleic acid (≥99.0%), oleylamine (70%), benzyl ether (98%), zinc chloride ($ZnCl_2$, ≥98%), 3-mercaptopropionic acid (3-MPA, ≥99.0%), tetramethylammonium hydroxide pentahydrate (≥97%), hexane (99%), toluene (99.5%), octadecyltrimethoxysilane (ODTMS, 90%), butylamine (99.5%), toluene (HPLC Plus, ≥99.0%), and methylene blue (≥82%) were purchased from SigmaAldrich. Sodium hydroxide (NaOH pellets, 99.3%), 2-propanol (99.9%) and methanol (99.9%) were purchased from Fisher Scientific. 1,2-Ethanediol (99.8%) was purchased from Macron Fine Chemicals. Ethanol (95%) was purchased from Decon Laboratories. Ammonia (99.99%) was purchased from Airgas. All chemicals were purchased commercially and used without additional purification.

4.2.2 $(Ga_{1-x}Zn_x)(N_{1-x}O_x)$ NC Synthesis

$(Ga_{1-x}Zn_x)(N_{1-x}O_x)$ nanocrystals were synthesized as previously described and outlined in full detail in Chapter 2.[25,26] A powder mixture of 3-MPA capped $ZnGa_2O_4$ and ZnO nanoparticles were placed into an alumina boat which was then placed into a tube furnace (Across International model STF 1200). The starting mixture of particles was heated to 650 °C under a constant flow of ammonia gas for 10 hours. The resulting product is a powder that was stored in a vial for future use.

4.2.3 $(Ga_{1-x}Zn_x)(N_{1-x}O_x)$ NC Solubilization

The synthesis method described produces particles as an insoluble powder. The particles were functionalized with octadecyltrimethoxysilane (ODTMS) ligands, as previously published and

described in Chapter 2, so that the particles were soluble in toluene.[35] ODTMS-$(Ga_{1-x}Zn_x)(N_{1-x}O_x)$ nanocrystals were dissolved in toluene and kept airfree for future use.

4.2.4 Characterization

Elemental analysis of Zn and Ga were obtained using an ARL 3410+ ICP-OES. UV-Vis absorption spectra were recorded using an Agilent 8453 UV-Vis spectrophotometer and diffuse reflectance spectra were collected on an Agilent Cary 60 spectrophotometer. Diffuse reflectance spectra were converted to a Kubelka-Munk plot using the equation [$F(R_\infty) = (1 - R_\infty)^2/2R_\infty$; $R_\infty = R_{sample}/R_{reference}$]. A 100 % reflectance standard Halon puck was used as the reference. Powder XRD patterns were collected on a Rigaku Dmax diffractometer using a Cu Kα radiation source (λ = 0.1540562 nm). The patterns were recorded from 25 to 80° 2θ using a step size of 0.02° 2θ. TEM images were obtained using a FEI Tecnai Spirit BioTwin and a FEI Technai F20 FEG TEM.

The transient absorption (TA) setup was previously described in full detail in Chapter 2 and previously published.[67] TA measurements were obtained using an amplified Ti:sapphire laser (Solstice, Spectra-Physics, 800 nm, 100 fs), an optical parametric amplifier (TOPAS-C, Light Conversion), and the HELIOS spectrometer (Ultrafast Systems, LLC), for short timescale (100 fs – 3 ns) measurements. A CaF_2 crystal was used to generate the white light continuum probe pulse (340-800 nm). For long timescale measurements (300 ps – 100 μs), the EOS spectrometer (Ultrafast Systems, LLC) was used. The TA experiments were all carried out in an airfree (sealed under Ar) quartz cuvette at room temperature, with constant stirring. Absorption spectra of the samples were collected before and after TA measurements and no substantial changes were observed (Figure 4.1). All of the TA spectra were background subtracted, chirp-corrected using

the instrument response function (IRF) determined from TA data of toluene, and time zero corrected.

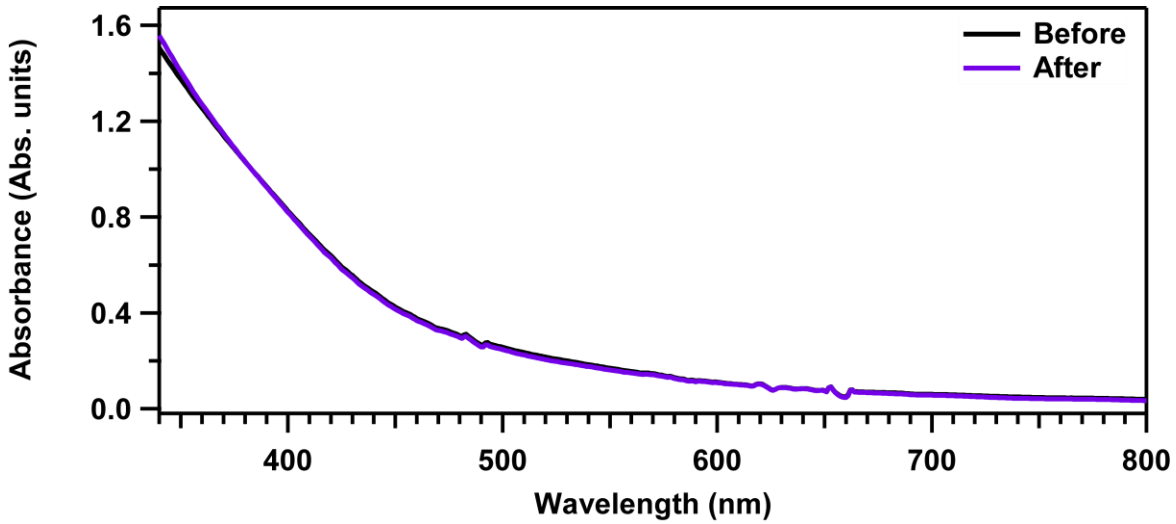

Figure 4.1. UV-Vis absorption spectra of $(Ga_{0.6}Zn_{0.4})(N_{0.6}O_{0.4})$ nanoparticles recorded before and after Transient Absorption measurements. The sample was exposed to illumination by the laser for the course of about 8 hours during TA measurements and no substantial change was observed in the absorption spectra.

4.3 Results and Discussion

In this chapter, we focus on studying $(Ga_{1-x}Zn_x)(N_{1-x}O_x)$ nanocrystals synthesized at 650 °C with an x value of 0.4. Such particles have been shown to have strong visible absorption. Particles are synthesized as an insoluble powder. In order to perform absorption experiments, particularly transient absorption spectroscopy, the particles were solubilized using surface functionalization with octadecyltrimethoxysilane (ODTMS) ligands, as previously published.[35] The steady state absorption spectrum of the solubilized $(Ga_{0.6}Zn0_{0.4})(N_{0.6}O_{0.4})$ nanoparticles is shown in Figure 4.2a, where the broad visible absorption is evident. Powder X-ray diffraction (XRD) shows characteristic peaks of a wurtzite crystal structure with peak positions between reference patterns for ZnO and GaN peaks, as we normally observe (Figure 4.2b).[25,26,34,35]

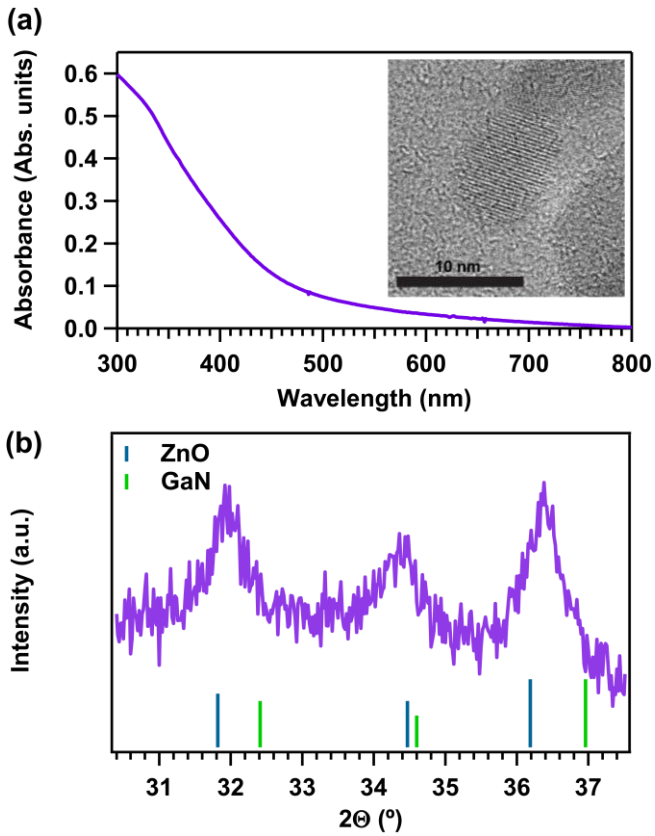

Figure 4.2. (a) Absorption spectrum of solubilized $(Ga_{0.6}Zn_{0.4})(N_{0.6}O_{0.4})$ nanoparticles. Inset: HRTEM image. (b) XRD after solubilization with ZnO (blue, JCPDS #05-0664) and GaN (green, JCPDS #2-1078) reference peaks.

Characterization by low-magnification transmission electron microscopy (TEM) is shown in Figure 4.3, for solubilized particles, with diameters of 16.2 ± 6.7 nm. The particles exhibit a broad size distribution, as we have previously reported.[25,26,34,35]

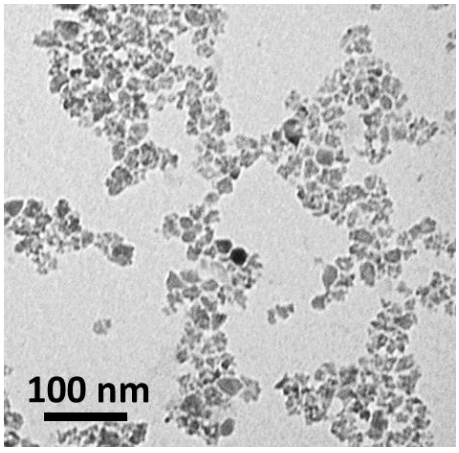

Figure 4.3. TEM image of solubilized $(Ga_{0.6}Zn0_{0.4})(N_{0.6}O_{0.4})$ nanoparticles.

Scherrer analysis of the XRD peaks (Table 4.1) yields an average crystallite size of 13.0 ± 3.7 nm. This is in agreement with the average diameter measured using the low-magnification TEM images. Finally, high resolution transmission electron microscopy (HRTEM) indicates that the particles are single crystalline, as shown in the inset of Figure 4.2a.

Table 4.1. Crystallite and nanoparticle sizes measured using Scherrer analysis of XRD and TEM measurements, respectively.

Scherrer Analysis (XRD)				TEM
(100) peak (nm)	**(002) peak (nm)**	**(101) peak (nm)**	**Average crystallite size (nm)**	**Average particle size (nm)**
13.8	9.1	16.3	13.1 ± 3.7	16.2 ± 6.7

4.3.1 TA Spectrum and Kinetic Decay

In order to understand the excited state dynamics of solubilized $(Ga_{0.6}Zn_{0.4})(N_{0.6}O_{0.4})$ nanoparticles, we performed transient absorption spectroscopy studies. Figure 4.1 shows that the nanoparticle solution was stable during TA experiments, where the UV-Vis absorption did not change after TA measurements. We observed the behavior of the decay kinetics in the visible region of the spectrum after excitation at 340 nm, which is well above the band edge of the nanoparticles (E_g ~2.8 eV). The TA signal of $(Ga_{0.6}Zn_{0.4})(N_{0.6}O_{0.4})$, pumped with 500 uW power, at various time delays after the pump pulse, is shown in Figure 4.4a. We observe a broad bleach in the visible part of the spectrum and find that the bleach exhibits a subtle shift to higher wavelengths over time. The inset of Figure 4.4a shows the bleach maximum center position as a function of time. We will call this position λ_{max}. The λ_{max} is marked at various time delays, showing the shift to higher wavelengths. As discussed below, this shift is due to Auger recombination of

multiple carriers. If carriers are excited well above the band-edge, as they recombine via Auger recombination, the λ_{max} position shifts over time.

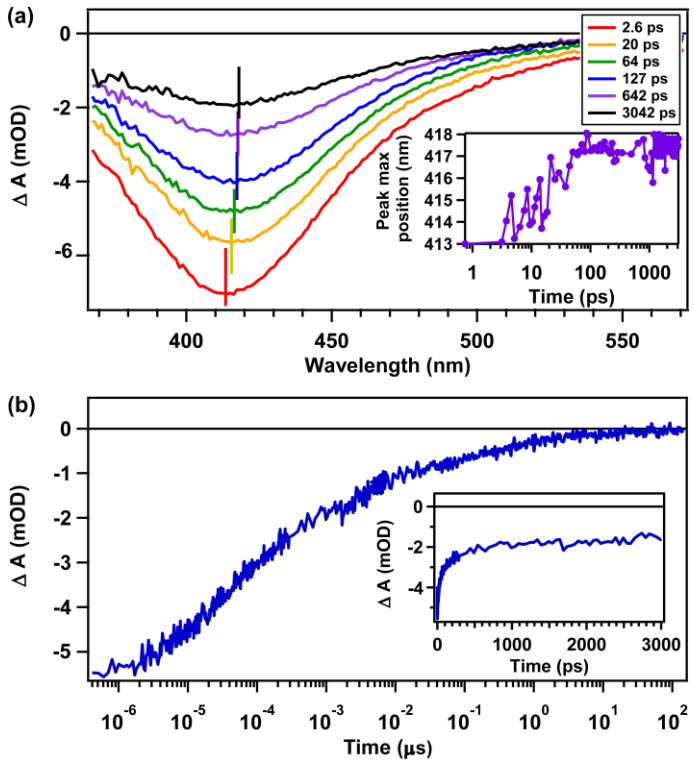

Figure 4.4. (a) TA spectrum of $(Ga_{0.6}Zn_{0.4})(N_{0.6}O_{0.4})$ with bleach max (λ_{max}) position at different pump-probe delay times. Inset: λ_{max} is plotted as a function of time delay which shows the peak shifting over time. (b) Early (0 – 3 ns) and late time (3 ns – 100 μs) kinetics at λ_{max} are presented together to yield the resulting kinetic trace for the full time window of 0 to 100 μs. Inset: Early time kinetics from 0 to 3 ns.

We also monitor the decay kinetics at the λ_{max} position, as shown in Figure 4.4b, where short time measurement (0-3 ns) and long time measurement (300 ps – 100 μs) are stitched together. The decay kinetics observed show the recovery of the photoinduced bleach as the charge carriers recombine. By monitoring the bleach recovery of the visible transition, we can study the recombination of carriers in $(Ga_{1-x}Zn_x)(N_{1-x}O_x)$. An initial sharp decrease in the signal that is short-lived, can be seen in the inset of Figure 4.4b. Such a fast decrease in signal, along with the peak shift over time, is indicative of a fast carrier recombination process resulting from carrier accumulation. There is also a longer lived decay component that does not reach zero until about

20 μs. These short and long-lived components were previously reported for a sample of $(Ga_{1-x}Zn_x)(N_{1-x}O_x)$ with an x value of 0.73.[35] We wanted to gain a better understanding of what these short and long-lived components in the visible decay were due to and how they relate to recombination in the particles.

4.3.2 Band Filling and Burstein-Moss Effect

We performed a power dependence study, where the sample was excited at a range of pump powers corresponding to initial carrier densities from 4.5×10^{17} to 2.1×10^{20} carriers/cm^3. The average number of carriers per particle, <N>, and initial carrier densities, N_0, at various pump powers, are shown in Table 4.2.

Table 4.2. Average number of carriers per particle, <N> and initial carrier density, N_0 as a function of pump power.

Power (uW)	**<N> carriers/particle**	**Initial Carrier Density N_0 (carriers/cm^3)***
7	1	4.5×10^{17}
10	2	9.0×10^{17}
30	7	3.1×10^{18}
70	16	7.2×10^{18}
100	23	1.0×10^{19}
300	68	3.1×10^{19}
500	114	5.1×10^{19}
700	159	7.1×10^{19}
900	205	9.2×10^{19}
1100	250	1.1×10^{20}
1800	409	1.8×10^{20}
2100	478	2.1×10^{20}

*Using volume of particle = 2.23×10^{-18} cm^3

These values were calculated using experimental parameters, which include the spot size of the laser pump pulse, sample path length, and concentration of nanocrystal solution. Upon excitation with higher powers, a greater carrier density is excited within the particles. This increase in carrier density causes a blueshift of the visible bleach, which is shown in Figure 4.5a. Figure 4.5b shows the bleach position shifting to lower wavelengths, with increasing numbers of carriers per particle, along with an increase in the peak width (FWHM). The peak broadening, with a carrier-density-dependent blueshift, is indicative of charge carrier accumulation. A dynamic Burstein-Moss shift is used to explain this bandgap shift to higher energies.[68-71] The Burstein-Moss theory says that as more photogenerated carriers fill sites at the conduction and valence band-edges due to higher excitation energies, additional bleaching must effect higher energy optical transitions. In other words, when high carrier densities are generated in $(Ga_{0.6}Zn_{0.4})(N_{0.6}O_{0.4})$, their presence leads to a seemingly larger bandgap. We can confidently assign the negative TA feature to ground-state bleaching and the blue-shift of the bleach to state filling at the band-edges.

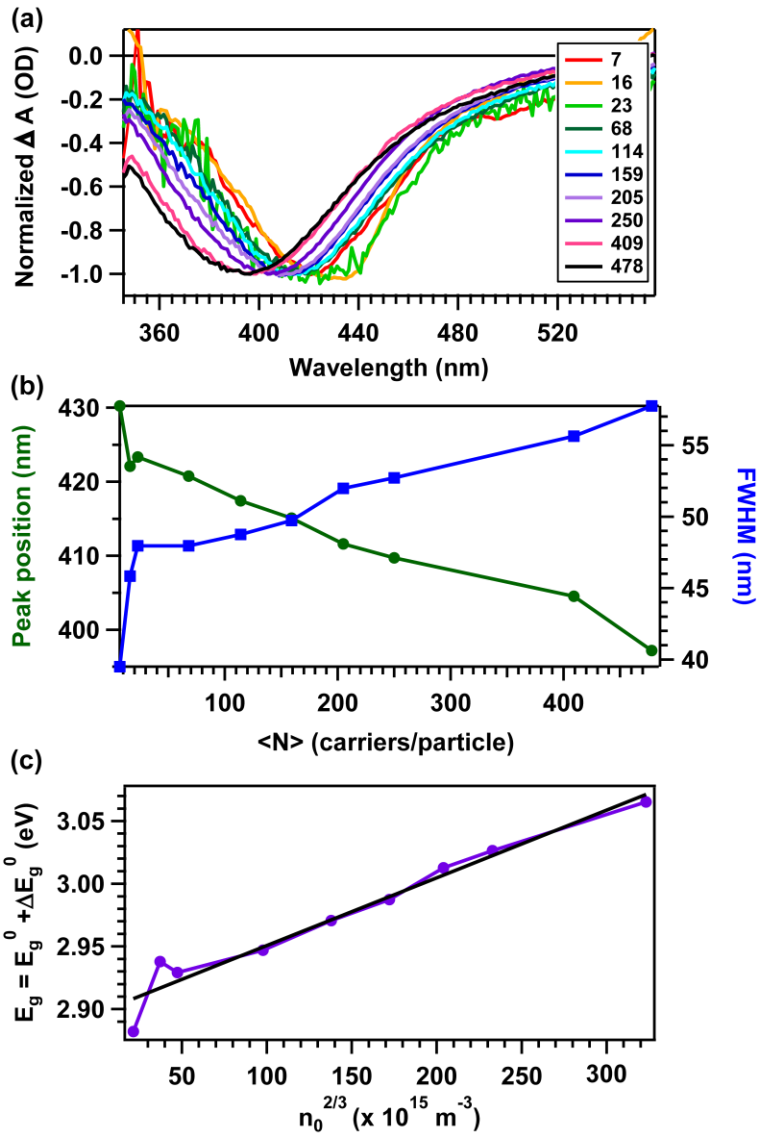

Figure 4.5. (a) TA spectra of $(Ga_{0.6}Zn_{0.4})(N_{0.6}O_{0.4})$ pumped at 340 nm using various pump powers, at a 5 ps time delay. The values in the legend are <N>, or carriers per particle at each pump power. (b) Peak position and FWHM of visible bleach at various pump powers, shown as carriers/particle. (c) Bandgap as a function of $n_0^{2/3}$ where n_0 is initial carrier density.

Knowing that $(Ga_{0.6}Zn_{0.4})(N_{0.6}O_{0.4})$ nanoparticles exhibit this Burstein-Moss shift, we can determine the reduced effective mass of excited state carriers. The Burstein-Moss shift is described using equation (4.1)[72]

$$\Delta E_g^{BM} = \frac{\hbar^2}{2m_{eh}^*}(3\pi^2 n)^{2/3} \tag{4.1}$$

where ΔE_g^{BM} is the change in the optical bandgap caused by the Burstein-Moss band filling, ħ is the reduced Planck constant, n is the carrier density, and m_{eh}^* is the reduced effective mass of the electron and hole. We don't know the exact value of the intrinsic bandgap of the nanoparticles. However, we can treat the bleach position as the optical bandgap which includes the sum of the intrinsic bandgap and the change in the optical bandgap due to the carrier-induced shift. To date, there are no experimental reports of the effective masses of either the electron or hole in $(Ga_{1-x}Zn_x)(N_{1-x}O_x)$ nanoparticles. We assume here that both the electron and hole contribute to the dynamic band filling effect. With this, we plotted the optical bandgap (position of λ_{max} at various powers) as a function of $n_0^{2/3}$, which is shown in Figure 4.5c. The linear proportionality further indicates agreement with the Burstein-Moss theory.

From the slope, we determined the reduced effective mass to be 6.2×10^{-31} kg, or $0.68m_0$, which is larger, but on the order of the reduced effective mass in Si, which is about $0.56m_0$, where m_0 is the free electron rest mass of 9.109×10^{-31} kg.[73] The reduced effective mass of the electron and hole in bulk GaN and ZnO is around $0.2m_0$.[55,74-76] The effective masses of the electron and hole respectively are $0.22m_0$ and $0.8m_0$ in GaN, and $0.28m_0$ and $0.5m_0$ in ZnO.[55] Such effective masses would lead us to believe that the reduced effective mass of carriers in $(Ga_{1-x}Zn_x)(N_{1-x}O_x)$ to be around $0.2m_0$. Hybrid density functional theory calculations also predict a high valence band maximum effective mass, but a lower conduction band minimum effective mass with an overall effective mass of ~$0.2m_0$ for bulk $(Ga_{1-x}Zn_x)(N_{1-x}O_x)$.[77] However, we clearly observe that nanoscale $(Ga_{0.6}Zn_{0.4})(N_{0.6}O_{0.4})$ has both carriers with large effective masses. We know that with a reduced effective mass of $0.68m_0$, the conduction band effective mass cannot be $0.2m_0$ because this would yield a negative valence band effective mass, which is not feasible. Knowing that the carriers in $(Ga_{0.6}Zn_{0.4})(N_{0.6}O_{0.4})$ are heavy, we have more information about band edge properties.

For example, we know that the curvature of the bands must be small. These properties result in carriers with low mobilities. Carriers which do not move and accelerate easily, are hindered in their effectiveness in solar energy applications. This new result could potentially help us explain the ability of $(Ga_{1-x}Zn_x)(N_{1-x}O_x)$ particles to be efficient for use as a water-splitting photocatalyst.

4.3.3 Power Dependent Kinetics

Monitoring the bleach position as a function of pump power led us to understand carrier accumulation in the particles. Next, we focused on studying the decay kinetics as a function of pump power. The results of the kinetic power dependence study are shown in Figure 4.6 (Kinetics on log scale are shown in Figure 4.7), where kinetics are observed at the λ_{max} position over time at various pump powers.

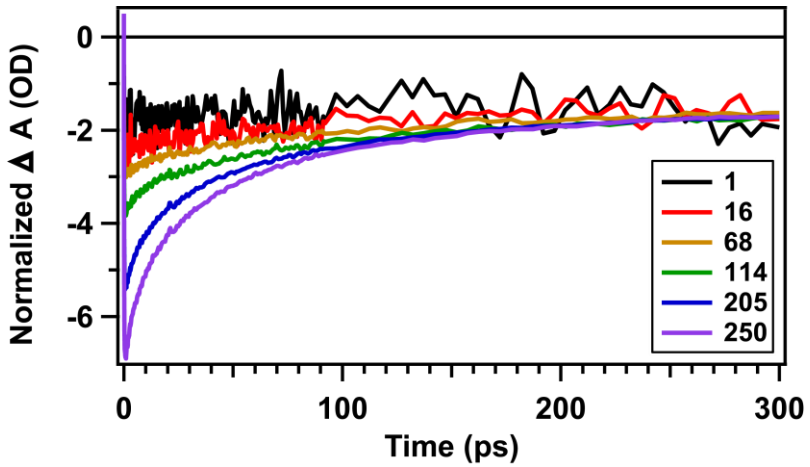

Figure 4.6. Pump power dependence of TA kinetics of $(Ga_{0.6}Zn_{0.4})(N_{0.6}O_{0.4})$ nanocrystals pumped at 340 nm. Kinetics at λ_{max} are normalized at 3 ns at several pump powers. The values in the legend are given as number of carriers per particle. This data suggests that the TA kinetics are in fact dependent on pulse energy.

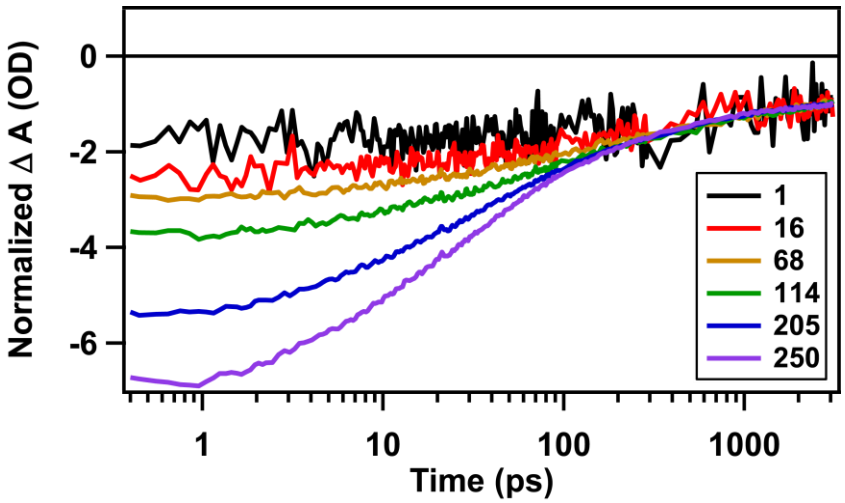

Figure 4.7. Decay kinetics at λ_{max} normalized at 3 ns at various numbers of carriers/particle (shown in legend).

To confirm that nonlinear excitation such as two-photon absorption did not occur in this experiment, the intensity as a function of pump power was plotted in Figure 4.8. The linear proportionality indicates that the carriers were generated through a one photon process and that nonlinear excitation processes were not involved.

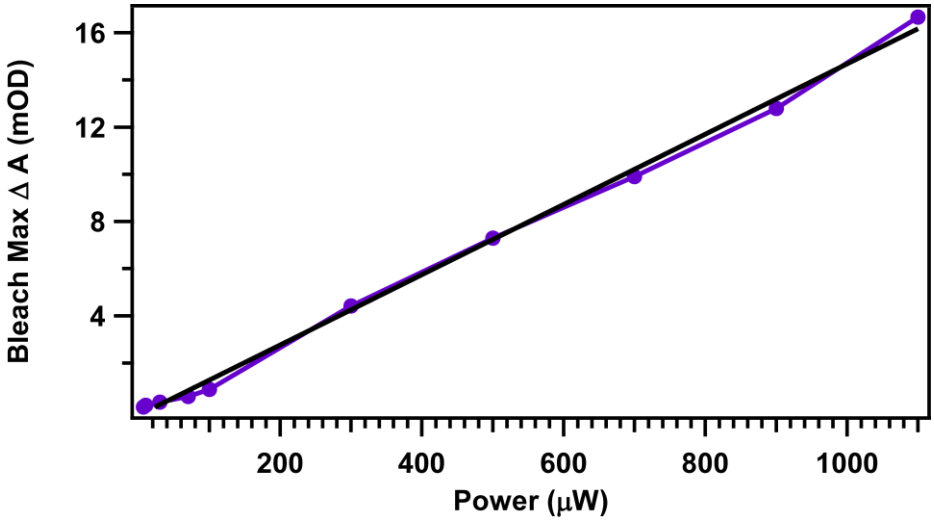

Figure 4.8. Bleach max (λ_{max}) intensity as a function of pump power.

There is a clear power dependence, where the carriers decay faster in the sample when pumped at higher intensities (higher number of carriers per particle). In particular, Figures 4.6 and 4.7 indicate

that the short lived decay component, previously mentioned, goes away with decreasing pump power. Since the short lived component goes away as pump power decreases, the short component decay must be due to a carrier density dependent process. The average number of carriers per particle is greater than 1 at all pump powers greater than 7 uW, as we showed in Table 4.1. Since multiple carriers are being excited per particle and the decay is carrier dependent, we proposed that the short component is due to a quick process such as cooling/relaxation back to the band edge, trapping, or Auger recombination. We find that the long component decay does not depend on pump power, which is shown in Figure 4.9. Since the power dependence of the decay kinetics is only observed in the early time window, we focus first on exploring the short component kinetics with a decay model.

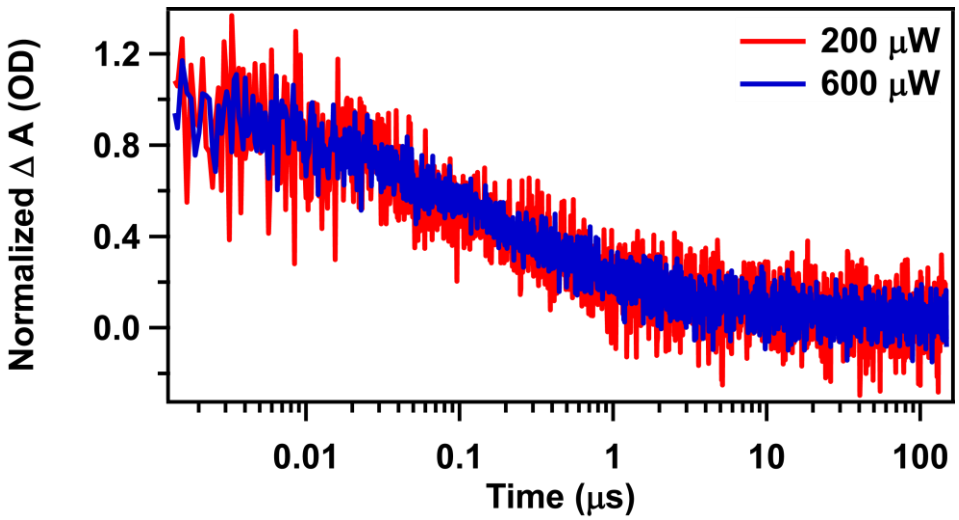

Figure 4.9. Decay kinetics of the long component (up to 100 μs) at two different pump powers. There was no difference observed in the decay kinetics at the different pump powers indicated, so there is no power dependence in the longer timescale of the decay.

4.3.4 Short Component Decay

In order to gain a more quantitative understanding of the decay kinetics in $(Ga_{1-x}Zn_x)(N_{1-x}O_x)$ nanoparticles, we fit to a model that can explain the recombination kinetics of the fast component in the decay. Upon photoexcitation, carrier density N_0 is created. After photoexcitation, the carrier

density N relaxes back to zero. Equation (4.2) can be used to describe this process of free carrier recombination, where A represents the Shockley-Read or trap mediated recombination rate constant, B represents the nongeminate radiative recombination rate constant (luminescence), and C represents the Auger recombination rate constant.[69,78-80]

$$\frac{\mathrm{d}N}{\mathrm{d}t} = -\mathrm{A}N - \mathrm{B}N^2 - \mathrm{C}N^3 \tag{4.2}$$

Again, we are first focused on modeling the carrier density dependent kinetics on the short timescale from 0 to 3 ns. In order to do this, the short component needed to be extracted from the full decay. This was done by subtracting the long-lived signal as a y-offset from the decay trace. The resulting kinetics are the short component of the visible bleach.

When solving expression (4.2) numerically, and fitting N vs. t, for the decay kinetics of the short component, we found that there is no significant change in the fit with and without the second term (B). Geminate (band-edge) recombination in the $(Ga_{1-x}Zn_x)(N_{1-x}O_x)$ sample does not occur on this short timescale and therefore, it would make sense that the second term involving B, can be neglected. This results in recombination equation (4.3).

$$\frac{\mathrm{d}N}{\mathrm{d}t} = -\mathrm{A}N - \mathrm{C}N^3 \tag{4.3}$$

When solving equation (4.3) for N, where N is the carrier density evolving from N_0 (initial carrier density), and t is the time, expression (4.4) is obtained.

$$N = \sqrt{\frac{\mathrm{A}\frac{{N_0}^2}{\mathrm{C}N_0^2+\mathrm{A}}\mathrm{e}^{-2\mathrm{A}t}}{1-\mathrm{C}\frac{N_0^2}{\mathrm{C}N_0^2+\mathrm{A}}\mathrm{e}^{-2\mathrm{A}t}}} \tag{4.4}$$

Fitting kinetic decays of $(Ga_{0.6}Zn_{0.4})(N_{0.6}O_{0.4})$ to expression (4.4) gives us recombination rate constants for A and C. Knowing these rate constants allows us to determine the lifetimes with which these processes occur in the $(Ga_{0.6}Zn_{0.4})(N_{0.6}O_{0.4})$ nanocrystals. We were able to

successfully globally fit the short component of the decay to expression (4.4), as shown in Figure 4.10 for various carrier densities. Therefore, we know that this short-lived decay component is due to trap mediated and Auger recombination.

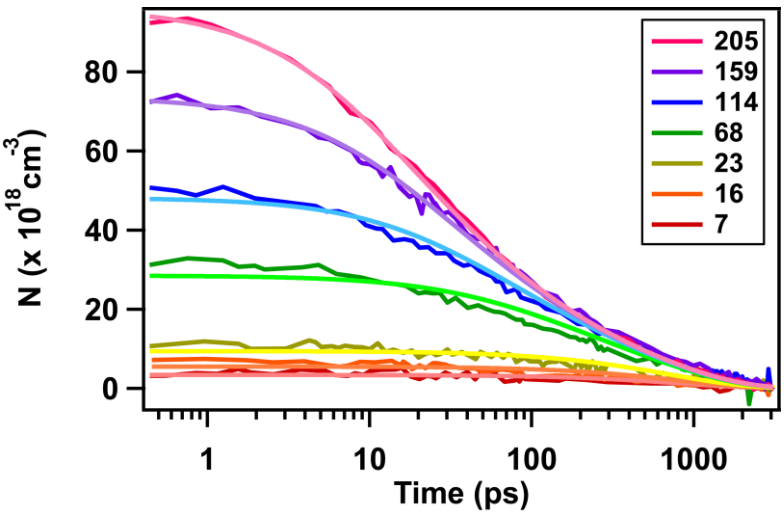

Figure 4.10. Power dependent kinetics (short component) globally fit to expression (4.4). Values in legend are number of carriers per particle generated at increasing pump powers.

The rate constants for trap mediated and Auger recombination were obtained by globally fitting the short component decay at various pump powers. Values of 1.18 (± 0.05) × 10^{9} s^{-1} and 5.6 (± 0.2) × 10^{-30} cm^{6} s^{-1} correspond to the trap mediated and Auger recombination rate constants respectively. Literature values for various semiconductor systems have been reported with values of trap mediated recombination constants between 10^{6} – 10^{9} s^{-1} and values of Auger recombination rate constants of 10^{-28} – 10^{-30} cm^{6} s^{-1}.[81-85] The values we report here are in agreement with the literature. Rate constants for trap mediated and Auger recombination correspond to lifetimes of trap mediated recombination of about 900 ps, and of Auger recombination, being a power dependent process, ranging from 20 – 4,000 ps as pump power decreases. The results are summarized in Table 4.3. These lifetimes are on the order of what we would expect for trap mediated and Auger recombination in semiconductor nanocrystals.[86] In colloidal quantum dots, fast Auger recombination times below 1 ns are observed.[87-89] In bulk GaSb, the Auger

recombination lifetime is slower than for GaSb quantum wells, but still on the order of a few ps to 100s of ns.[90] Therefore, we conclude that the short component decay in the $(Ga_{1-x}Zn_x)(N_{1-x}O_x)$ is due to trap mediated and Auger recombination. Next, we move forward to understanding the long-lived component in the decay.

Table 4.3. Values for trap mediated and Auger recombination lifetimes at various pump powers.

Pump Power (μW)	Trap mediated recombination lifetime (ps)	Auger recombination lifetime (ps)
70	847	3,463
100	847	1,676
300	847	192
500	847	68
700	847	35
900	847	21

4.3.5 Long Component Decay

In $(Ga_{1-x}Zn_x)(N_{1-x}O_x)$ decay kinetics, we observe long-lived average carrier lifetimes, $<\tau>$. To calculate $<\tau>$ in $(Ga_{0.6}Zn_{0.4})(N_{0.6}O_{0.4})$, equation (4.5) was used, where the short and long timescale kinetics were combined and the TA signal was integrated.[91]

$$<\tau> = \frac{\int_0^\infty t\Delta A(t)\,dt}{\int_0^\infty \Delta A(t)\,dt} \tag{4.5}$$

The value of $<\tau>$ obtained for sample x=0.40, has an average of about 50 μs. Clearly, this is a long average lifetime for a semiconductor, where average lifetimes are usually in the sub-ns range for direct bandgap semiconductors.[55,92] We wanted to use a model that would allow us to explain the long-lived lifetime in the oxynitride samples.

In order to fit the decay kinetics of the long-lived decay component out to about 100 μs, we used a stretched exponential (4.6). A fit to a stretched exponential is shown in Figure 4.11a, with fit results summarized in Table 4.4. Often in the literature, a fit to a stretched exponential decay indicates a broad distribution of trap states or trap-limited recombination.[60,93-99]

$$f(t) = A * e^{-\left(\frac{t}{\tau}\right)^{\beta}} \quad (4.6)$$

The long-lived component therefore could be due to one carrier decaying while the other was trapped. The bleach decay that lives after fast Auger recombination and trap mediated recombination occurs could be monitoring the carrier that was not trapped. We also find that the end of the long time decay can be fit to a power law (equation (4.7)), as shown in Figure 4.11b, with fit results summarized in Table 4.5.

$$f(t) = A * t^{-\alpha} \quad (4.7)$$

A power law decay is often attributed to trap-limited recombination as well.[100-102] Again, an electron or hole is temporarily unavailable due to it being trapped and therefore recombination cannot occur. Both the stretched exponential fit and the power law decay support the idea that the long-lived component is due to trap-limited recombination. We find that the power law decays with an exponent of 0.31. This value less than 1 is typically indicative of trapping-detrapping mediated recombination.[99,102,103] James Durrant *et al* found that a bulk film of GaN:ZnO also exhibits a power law decay with an exponent of 0.33.[102] This is in agreement with the value we obtain for nanoscale particles in solution. Durrant *et al* attribute this value to a wide distribution of trap states.[102] In particular, they find that these trap states are deep hole trap states. It is possible that nanoscale $(Ga_{1-x}Zn_x)(N_{1-x}O_x)$ also exhibit such deep hole trap states, which would explain this long-lived component. In addition, deep hole trap states would explain the low water-splitting quantum efficiencies observed in these materials.

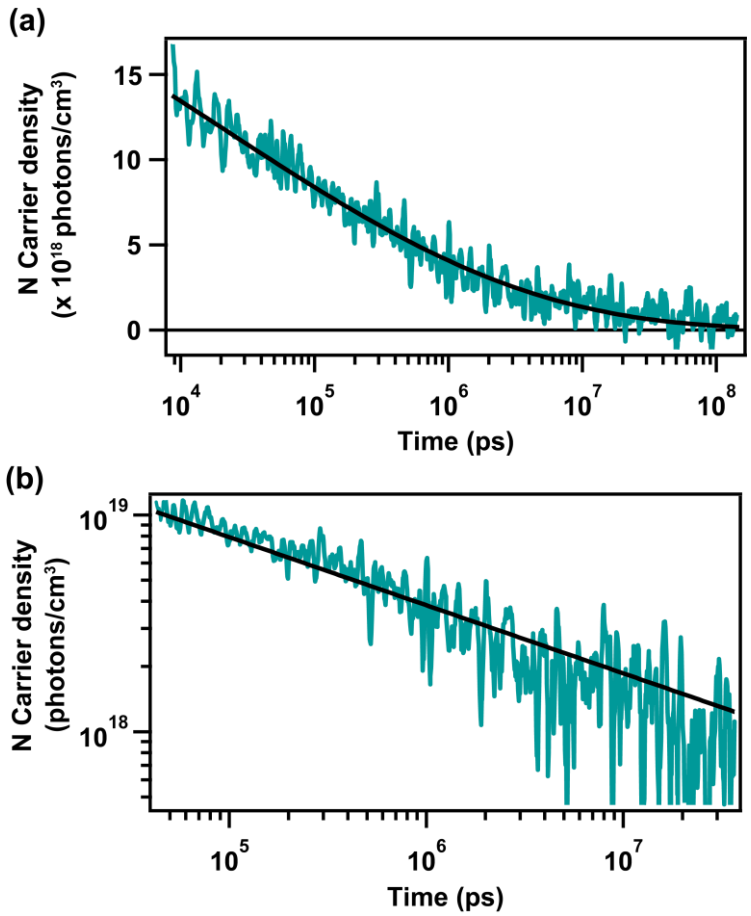

Figure 4.11. (a) EOS (long time) kinetics fit to a stretched exponential. (b) End of long component decay fit to a power law.

Table 4.4. Fit values obtained from stretched exponential decay (equation (4.6)).

Fit parameter	Value
A	$3.3\ (\pm\ 0.2) \times 10^{19}$
β	0.18 ± 0.01
τ	$1.8\ (\pm\ 0.5) \times 10^{4}$ ps

Table 4.5. Fit values obtained from power law decay (equation (4.7)).

Fit parameter	Value
A	$2.9\ (\pm\ 0.1) \times 10^{20}$
α	0.314 ± 0.003

4.4 Conclusions

Characterization of the excited state behavior in $(Ga_{1-x}Zn_x)(N_{1-x}O_x)$ nanocrystals is important for gaining an understanding of the behavior of the carriers upon illumination and how this impacts their ability to be used for solar water-splitting. We used femtosecond transient absorption spectroscopy to study the charge carrier dynamics in a sample of $(Ga_{1-x}Zn_x)(N_{1-x}O_x)$ nanocrystals with an x value of 0.4. We found an increase in the energy of the band-edge transition with an increase in carrier density to be in agreement with the Burstein-Moss theory, which says that band filling occurs as a result of carrier accumulation. Using this theory, we calculated the reduced effective mass of the electron and hole to be $0.68m_0$. The reduced effective mass of electrons and holes in nanoscale $(Ga_{1-x}Zn_x)(N_{1-x}O_x)$ has not been previously measured using experimental results. Such a high effective mass could result in low carrier mobilities which in turn would impact their effectiveness in water-splitting. We also determined that carriers initially decay via fast processes of Auger recombination and trap mediated recombination with rate constants of 5.6 (± 0.2) × 10^{-30} cm^6 s^{-1} and 1.18 (± 0.05) × 10^9 s^{-1} respectively. On the longer timescales with an average lifetime of 50 μs, we find that the decay is due to a trap-limited recombination. The information obtained here represents significant insights into the hitherto unknown electronic structure of $(Ga_{1-x}Zn_x)(N_{1-x}O_x)$, and will aid in further studies to explore its promising optical properties and utility as a photocatalyst.

Chapter 5. Further Investigation of Excited-State Dynamics in Various $(Ga_{1-x}Zn_x)(N_{1-x}O_x)$ Nanoparticles with Different Elemental Distributions

5.1 Introduction

Solar fuel generation is a desirable approach for harvesting renewable energy.[1] Various semiconductor light absorbers have promising characteristics for use in solar fuel generation.[61] Such characteristics include, the ability to absorb visible light in order to utilize the solar spectrum, suitable band potentials for catalysis, resistive to photooxidation, and long-lived excited states.[62,63] The necessity of controlling band gap and chemical stability has revealed the need for new semiconductors with multinary compositions.[64,65] There has been a lot of development of new ternary and quaternary mixed semiconductors in the solution phase.[104-106] In addition, solid state reactions have provided the possibility for more compositional complexity in such materials.[107-109] As more of these nanoscale solid-state reactions continue to emerge, it is necessary to understand how the elemental distribution in the resulting materials affects materials properties. In particular, understanding how the materials behave in their excited-state upon illumination is important for insights into future applications.

In this Chapter, we further investigate the properties of $(Ga_{1-x}Zn_x)(N_{1-x}O_x)$ nanoparticles. In this material, the x value controls the visible bandgap.[25,26] We have also discovered that synthesis temperature impacts the elemental distribution in these particles.[34] Previous studies discussed in Chapter 4 were conducted on samples synthesized at 650 °C. We found that such particles have heterogeneous distributions of the four elements; Zn, O, Ga, and N. In particular, using EDX analysis, we determined that particles synthesized at 650 °C have ZnO localized in the

core of the particle, and GaN on the edges.[34] By increasing the synthesis temperature to 800 °C, we were able to achieve a more homogenous distribution of the elements.[34]

Here, we seek to understand how the composition and the distribution of Ga, Zn, O, and N in $(Ga_{1-x}Zn_x)(N_{1-x}O_x)$ nanoparticles affects their excited-state behavior. In particular, we apply the recombination expression discussed in Chapter 4 to determine the trap mediated and Auger recombination rate constants and determine how the increased homogeneity changes the recombination dynamics. We also observe the excited-state behavior of a sample of small aggregated particles that results from the nitridation of the $ZnGa_2O_4$ precursor in the synthesis of $(Ga_{1-x}Zn_x)(N_{1-x}O_x)$ nanoparticles.[34] Furthermore, we present new transient absorption data of $(Ga_{0.6}Zn_{0.4})(N_{0.6}O_{0.4})$ nanoparticles probed in the near infrared (NIR). NIR spectra provide information about free carriers in the particles. Finally, we use an electron scavenger experiment, where methylene blue (MB) was used as an electron acceptor in TA measurements, of $(Ga_{1-x}Zn_x)(N_{1-x}O_x)$ nanoparticles, to determine the nature of excited-state transitions. In particular, we gained insight into whether the signals observed in TA spectroscopy are due to electrons or holes.

5.2 Materials and Methods

5.2.1 Chemicals

All chemicals were purchased commercially and used without additional purification.

Zinc acetylacetonate hydrate ($Zn(acac)_2$, 99.995%), gallium acetylacetonate ($Ga(acac)_3$, 99.99%], 1,2-hexadecanediol (90%), oleic acid (≥99.0%), oleylamine (70%), benzyl ether (98%), zinc chloride ($ZnCl_2$, ≥98%), 3-mercaptopropionic acid (3-MPA, ≥99.0%), tetramethylammonium hydroxide pentahydrate (≥97%), hexane (99%), toluene (99.5%), octadecyltrimethoxysilane (ODTMS, 90%), butylamine (99.5%), toluene (HPLC Plus, ≥99.0%), and methylene blue (≥82%) were purchased from SigmaAldrich. Sodium hydroxide (NaOH pellets, 99.3%), 2-propanol

(99.9%) and methanol (99.9%) were purchased from Fisher Scientific. 1,2-Ethanediol (99.8%) was purchased from Macron Fine Chemicals. Ethanol (95%) was purchased from Decon Laboratories. Ammonia (99.99%) was purchased from Airgas.

5.2.2 $(Ga_{1-x}Zn_x)(N_{1-x}O_x)$ NC Synthesis

$(Ga_{1-x}Zn_x)(N_{1-x}O_x)$ nanocrystals were synthesized as previously described in Chapter 2.[25] The resulting product is a powder that was stored in a vial for future use.

5.2.3 Nitrided $ZnGa_2O_4$ Synthesis

We synthesized particles using the same technique as described for synthesizing $(Ga_{1-x}Zn_x)(N_{1-x}O_x)$ nanocrystals at 650 °C.[25] However, for this synthesis, ZnO nanoparticles were not added to the alumina boat. Only $ZnGa_2O_4$ nanoparticles were put in the tube furnace and heated at 650 °C with constant NH_3 flow for 10 hours to result in "nitrided $ZnGa_2O_4$".[34]

5.2.4 $(Ga_{1-x}Zn_x)(N_{1-x}O_x)$ NC Solubilization

The synthesis method described produces particles as an insoluble powder. In order to perform absorption experiments, the particles were solubilized using surface functionalization with octadecyltrimethoxysilane (ODTMS), as previously published and described in detail in Chapter 2.[35]

5.2.5 Electron Scavenger Experiment Sample Preparation

Methylene blue was used as an electron scavenger in solution with $(Ga_{1-x}Zn_x)(N_{1-x}O_x)$. A small amount of methylene blue powder was dropped into the toluene solution of $(Ga_{1-x}Zn_x)(N_{1-x}O_x)$ particles and sonicated. The solution was placed in an airfree cuvette for transient absorption studies. UV-Vis absorption spectra indicated the presence of methylene blue in solution with the nanocrystals.

5.3 Characterization

5.3.1 UV-VIS Absorption Spectroscopy

UV-Vis absorption spectra were recorded using an Agilent 8453 UV-Vis spectrophotometer and an Agilent Cary 60 spectrophotometer.

5.3.2 Elemental Analysis

Elemental analysis of Zn and Ga were obtained using an ARL 3410+ ICP-OES.

5.3.3 TA Spectroscopy

The transient absorption (TA) setup was previously described in full detail in Chapter 2.[67] TA measurements were obtained using an amplified Ti:sapphire laser (Solstice, Spectra-Physics, 800 nm, 100 fs), an optical parametric amplifier (TOPAS-C, Light Conversion), and the HELIOS spectrometer (Ultrafast Systems, LLC), for short timescale (100 fs – 3 ns) measurements. A CaF_2 crystal was used to generate the white light continuum probe pulse (340-700 nm). For long timescale measurements (300 ps – 100 μs), the EOS spectrometer (Ultrafast Systems, LLC) was used. Measurements were also made from 100 fs – 8 ns using a sapphire crystal to generate the white light continuum probe pulse (450 nm-800 nm) and a sapphire crystal was used to generate the near infrared (NIR) probe pulse (800-1600 nm). The TA experiments were all carried out in an airfree (sealed under Ar) quartz cuvette at room temperature, with constant stirring. All of the TA spectra were background subtracted, chirp-corrected using the instrument response function (IRF) determined from TA data of toluene, and time zero corrected.

5.4 Results and Discussion

The excited-state behavior for $(Ga_{1-x}Zn_x)(N_{1-x}O_x)$ with x=0.4 synthesized at 650 °C was described in the previous chapter. Here, we reveal the effects of composition (x value) and elemental distribution on the recombination dynamics in various $(Ga_{1-x}Zn_x)(N_{1-x}O_x)$ nanoparticles

synthesized at 650 and 800 °C. We studied samples synthesized at 800 °C with values of x equal to 0.39 and 0.50 and compared them with the x=0.40 sample synthesized at 650 °C, which was fully characterized in Chapter 4. The x values reported are for the ensemble of particles in solution after they were solubilized. Particles needed to be surface functionalized with octadecyltrimethoxysilane (ODTMS) ligands in order for them to be soluble in toluene and usable in absorption experiments. The solubilization technique has been previously published.[35]

Figure 5.1 shows the UV-Vis absorption spectra of solubilized samples with x=0.40 (650 °C), x=0.39 (800 °C), and x=0.50 (800 °C). From these spectra, it is not apparent that there is a change in the optical properties of the particles when synthesized at different temperatures. The spectral shapes of all three samples are very similar and so it appears as though the distribution of the elements throughout the particles does not significantly change the optical properties of the material. However, we do note that the sample synthesized at 650 °C appears to have an additional UV transition that is present between 300 and 350 nm. This is similar to the UV transition observed in diffuse reflectance spectra discussed in Chapter 3. Here, we focus on comparing the excited-state properties in these samples.

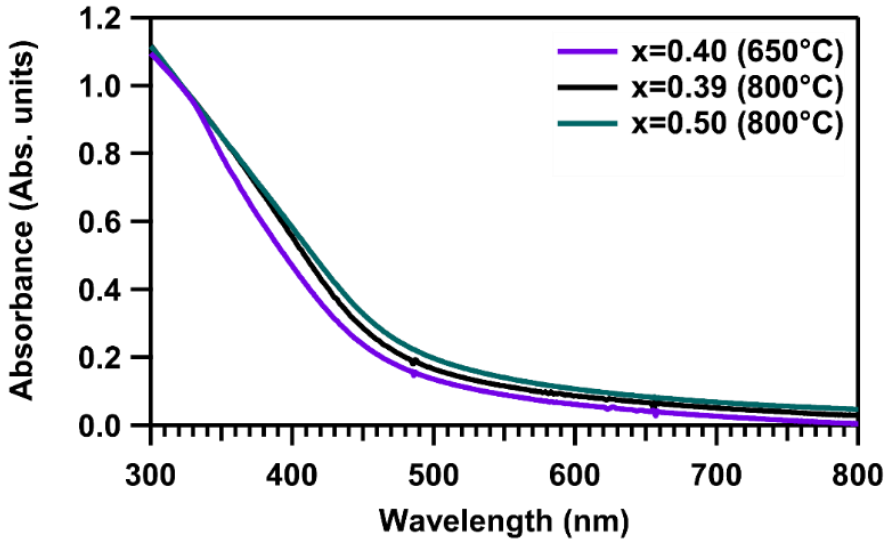

Figure 5.1. UV-VIS absorption spectra of $(Ga_{1-x}Zn_x)(N_{1-x}O_x)$ solubilized in toluene after synthesis at 650 °C (x=0.40) and 800 °C (x=0.39 and 0.50). The spectra are normalized at 320 nm.

5.4.1 Visible TA Spectroscopy Comparing Homogenous and Heterogeneous Particles

First, we observe the transient absorption spectra for the x=0.40 sample synthesized at 650 °C and x=0.39 and 0.50 samples synthesized at 800 °C. Figure 5.2 shows the transient absorption spectra at various time delays for these three samples. Just as with the steady-state spectra, the time resolved spectra also appear to have similar spectral shapes, with a broad visible bleach that appears to redshift over time. As discussed in the previous chapter, this shift is due to Auger recombination of multiple carriers. The similar spectral shapes and shifting in the homogenous samples is indicative of excited-state carrier behavior that is similar to the heterogeneous sample. In order to more quantitatively understand how the excited-state behavior in the homogenous samples compared to the heterogeneous, we applied the kinetic model used in Chapter 4 to carrier density-dependent decay dynamics.

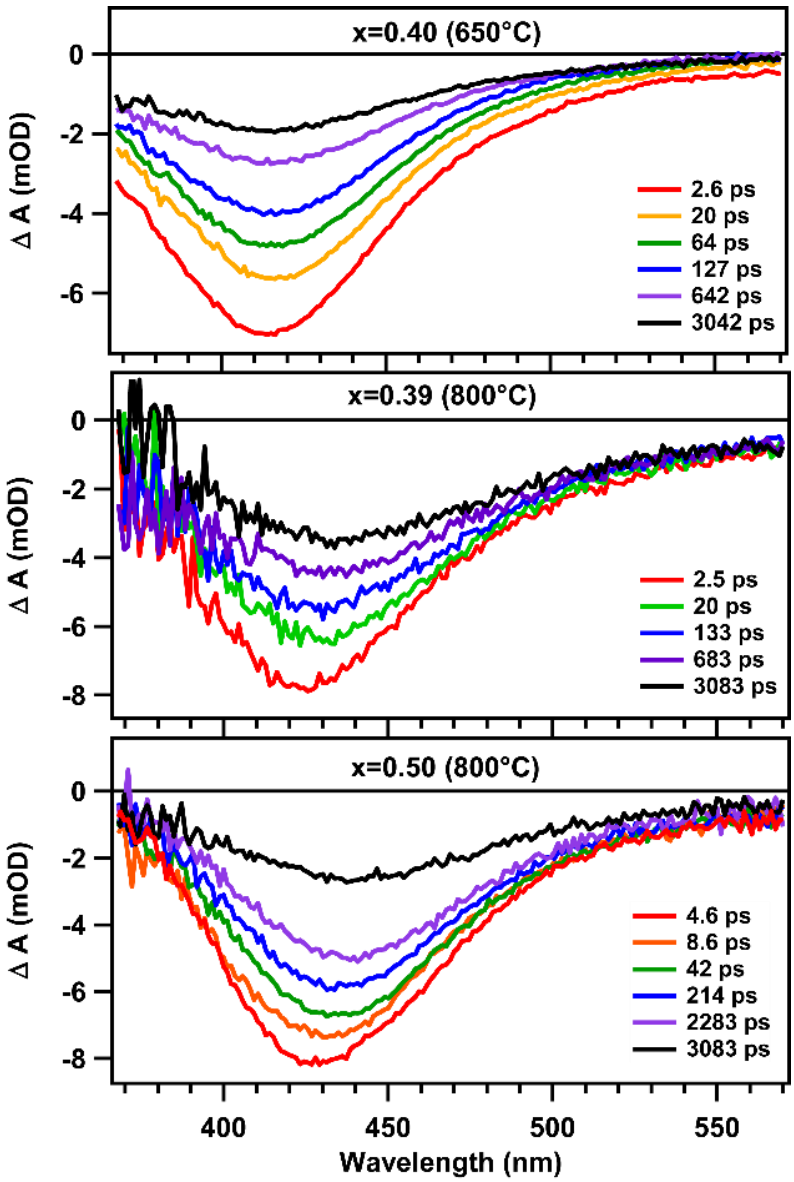

Figure 5.2. Transient absorption spectra for x=0.40 (650 °C) (top), x=0.39 (800 °C) (middle), and x=0.50 (800 °C) (bottom). Values in the legends are the various time delays at which the spectra were extracted.

Just as for the heterogeneous sample studied in Chapter 4, we extracted the short component decay kinetics at various numbers of carriers per particle at the bleach maximum position, which we define here as λ_{max}. Figure 5.3 shows the carrier density-dependent decay kinetics in the homogenous samples with x=0.39 and 0.50. We know there is a dependence on carrier density, because the decay is faster with increasing carrier density, or more carriers per

particle. This increase in decay rate with increasing carrier density is again indicative of a carrier density dependent process like Auger recombination.

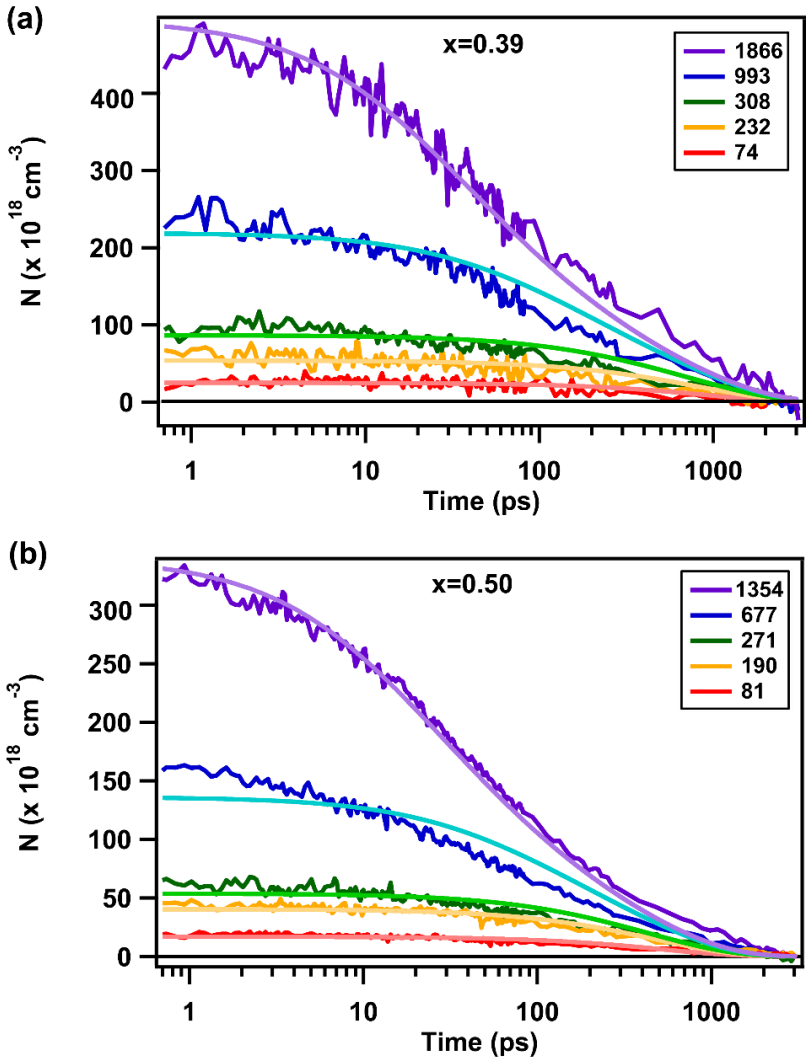

Figure 5.3. Extracted short component decay kinetics at various carrier densities for homogeneous samples x=0.39 (a) and x=0.50 (b). The respective global fits to carrier recombination expression given in equation (5.3) are shown. Values for number of carriers per particle for each decay trace are given in the legends.

As discussed in Chapter 4, we can use the expression in equation (5.1) to represent the decay of excited carriers in the $(Ga_{1-x}Zn_x)(N_{1-x}O_x)$ nanoparticles at early times in their decay (between 0 and 3 ns). After photoexcitation, carrier density N relaxes to zero from N_0 (initial carrier density). Equation (5.1) is used to describe the process of free carrier recombination, where A is

the trap mediated recombination rate constant, B is the nongeminate radiative recombination rate constant, and C is the Auger recombination rate constant.[69,78-80] We neglected the second term because radiative recombination is not observed on the short timescale we are interested in. The resulting expression is shown in equation (5.2). When solving equation (5.2) for N, where N is the carrier density evolving from N_0 as a function of time, expression (5.3) is obtained.

$$\frac{dN}{dt} = -AN - BN^2 - CN^3 \tag{5.1}$$

$$\frac{dN}{dt} = -AN - CN^3 \tag{5.2}$$

$$N = \sqrt{\frac{A\frac{{N_0}^2}{CN_0^2+A}e^{-2At}}{1-C\frac{N_0^2}{CN_0^2+A}e^{-2At}}} \tag{5.3}$$

We globally fit the short component decay in homogenous samples x=0.39 and 0.50 to expression (5.3). Global fits yielded results for the trap mediated (A) and Auger (C) recombination rate constants in these samples. The short time decay kinetics for samples with x=0.39 and 0.50, synthesized at 800 °C, and their fits, are shown above in Figure 5.3. The fits are similar to those obtained for heterogeneous sample with x=0.40, as was shown in Chapter 4. The resulting values for the trap mediated recombination rate constants (A) are 1.02 (±0.07) × 10^9 s^{-1} and 1.90 (±0.09) × 10^9 s^{-1} for homogenous samples with x=0.39 and 0.50, respectively. These values for trap mediated recombination rate constants are very similar to the value obtained for heterogeneous sample with x=0.40, which has a trap mediated recombination rate constant of 1.18 (± 0.05) × 10^9 s^{-1}. Next, we compare the Auger recombination rate constants. The values obtained for samples x=0.39 and x=0.50, respectively, are 9.80 (±16.90) × 10^{-32} cm^6s^{-1} and 3.17 (± 1.38) × 10^{-31} cm^6s^{-1}. The value for heterogeneous sample x=0.40 for Auger recombination rate constant was 5.6 (± 0.2) × 10^{-30} cm^6 s^{-1}. More or less, these values are within error of one another.

Therefore, the elemental distribution in the particles does not have a major effect on the recombination dynamics upon excitation. The values for trap mediated and Auger recombination rate constants for the three samples studied here are summarized in Table 5.1. It is certainly interesting that the elemental distribution in the $(Ga_{1-x}Zn_x)(N_{1-x}O_x)$ nanoparticles does not change the recombination rate constants for the short component decay. Other work being currently explored in our group on the comparison of electronic structure to absorbance spectra has led to conclusions that homogeneous particles have only one absorption feature in their electronic and optical absorbance spectra, while heterogeneous particles contain two features; a visible and a UV. We observed this subtle UV feature in Figure 5.1, and in the diffuse reflectance spectra, a much more prominent UV feature was observed in heterogeneous samples, in Chapter 3. It appears as though these differences in steady-state measurements between the homogeneous and heterogeneous particles, do not have a significant influence on the excited-state properties.

Table 5.1. Trap mediated (A) and Auger (C) recombination rate constants obtained from globally fitting short component decay kinetics at various carrier densities in $(Ga_{1-x}Zn_x)(N_{1-x}O_x)$ heterogeneous sample x=0.40 and homogenous samples x=0.39 and x=0.50.

Sample	Trap mediated recombination (A)	Auger recombination (C)
x=0.40 (heterogeneous)	$1.18 (\pm 0.05) \times 10^{9}\ s^{-1}$	$5.6 (\pm 0.2) \times 10^{-30}\ cm^{6}\ s^{-1}$
x=0.39 (homogeneous)	$1.02 (\pm 0.07) \times 10^{9}\ s^{-1}$	$9.80 (\pm 16.90) \times 10^{-32}\ cm^{6} s^{-1}$
x=0.50 (homogeneous)	$1.90 (\pm 0.09) \times 10^{9}\ s^{-1}$	$3.17 (\pm 1.38) \times 10^{-31}\ cm^{6} s^{-1}$

5.4.2 TA Spectroscopy of Nitrided $ZnGa_2O_4$ Nanoparticles

Previous work with samples synthesized at 650 °C led to the conclusion that $(Ga_{1-x}Zn_x)(N_{1-x}O_x)$ nanoparticle samples synthesized at 650 °C contain additional small aggregated particles (~ 5 nm diameter).[34] It was proposed that these small aggregated particles arise from the nitridation of

$ZnGa_2O_4$ that was not in direct contact with ZnO during $(Ga_{1-x}Zn_x)(N_{1-x}O_x)$ nanoparticle synthesis. In order to study the behavior of such small aggregated particles that contribute to the ensemble measurements of $(Ga_{1-x}Zn_x)(N_{1-x}O_x)$, we performed the synthesis procedure of nitriding $ZnGa_2O_4$ nanoparticles without the presence of ZnO. The resulting particles were in fact smaller than the typical $(Ga_{1-x}Zn_x)(N_{1-x}O_x)$ nanoparticles. A TEM image is shown in the inset of Figure 5.4a, where small agglomerated particles are evident with diameters of ~5 nm. The XRD pattern shown in Figure 5.4b exhibits a broadening of the typical wurtzite peaks of GaN and ZnO, which are shown for reference. It was not clear whether the broadening was due to small particle size or a mixture of spinel and wurtzite crystal structures. Previous elemental maps of these particles indicated a uniform distribution of Zn, Ga, O, and N.[34] Therefore, this sample nitrided at 650 °C, has elemental distribution similar to $(Ga_{1-x}Zn_x)(N_{1-x}O_x)$ nanoparticles synthesized at 800 °C. Our goal was to determine how the optical and excited-state properties in this material behaved compared to the other $(Ga_{1-x}Zn_x)(N_{1-x}O_x)$ nanoparticles we studied. The nitrided $ZnGa_2O_4$ particles were solubilized, just as previously described for $(Ga_{1-x}Zn_x)(N_{1-x}O_x)$ nanoparticle solubilization. The resulting absorbance spectrum is shown in Figure 5.4a, where the broad visible absorption is still clearly evident. Next, we studied the material using TA spectroscopy.

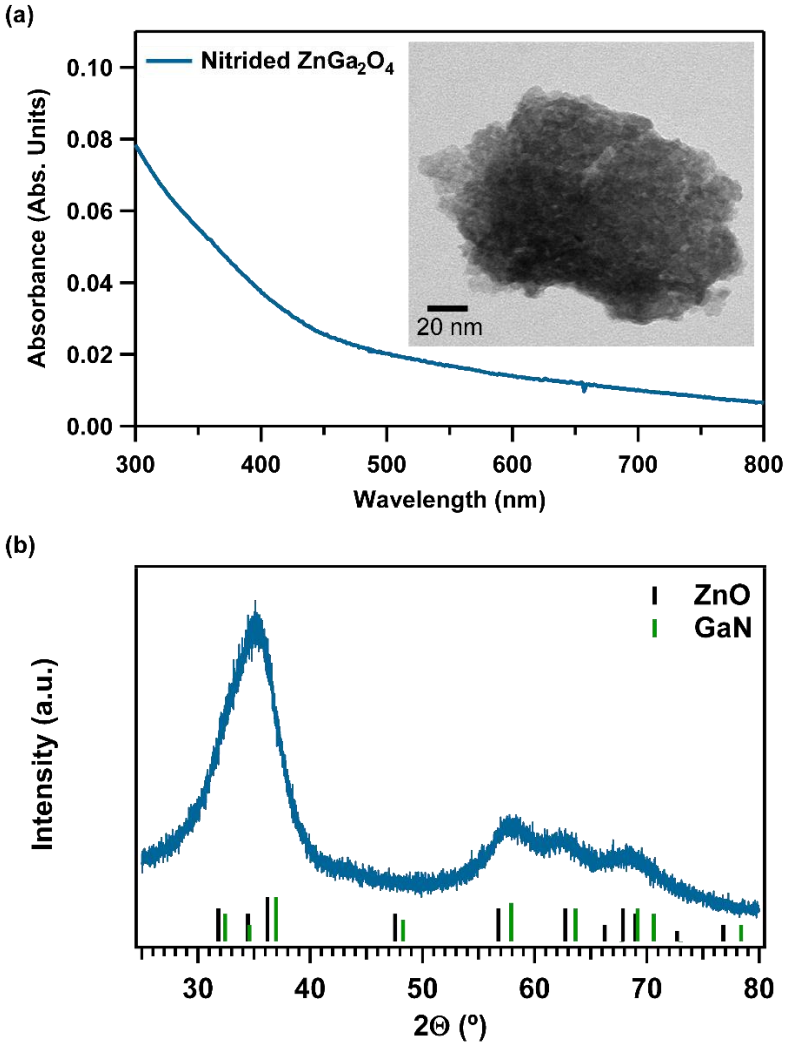

Figure 5.4. Absorbance of nitrided $ZnGa_2O_4$ in toluene (a) and low-magnification TEM image of nitrided $ZnGa_2O_4$ (inset). (b) Powder XRD pattern of nitrided $ZnGa_2O_4$. The verticle lines represent reference diffraction patterns of GaN (green, JCPDS #2–1078) and ZnO (black, JCPDS, #38–1240).

The TA spectrum of nitrided $ZnGa_2O_4$ is shown at various time delays in Figure 5.5. The spectral shape for the excited state absorption data also resembles that of the homogenous and heterogeneous $(Ga_{1-x}Zn_x)(N_{1-x}O_x)$ nanoparticles. It is interesting that these small aggregated particles, with a potentially different crystal structure, still exhibit such similar optical properties to the wurtzite $(Ga_{1-x}Zn_x)(N_{1-x}O_x)$ nanoparticles. Next, we sought to understand how the nitrided $ZnGa_2O_4$ decay kinetics compared to $(Ga_{1-x}Zn_x)(N_{1-x}O_x)$ nanoparticle decay kinetics. Just as for

previous samples, the short component of the decay was extracted at λ_{max} for various numbers of carriers per particle.

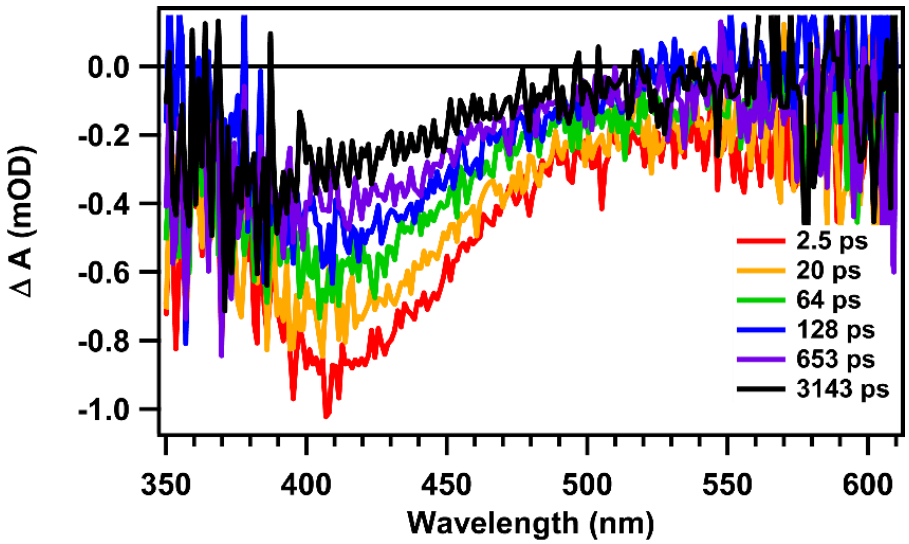

Figure 5.5. TA spectra of nitrided $ZnGa_2O_4$ at various time delays. Time delays are given in the legend from 2.5 to 3,143 ps.

Figure 5.6 shows the carrier density-dependent decay kinetics at λ_{max} for various numbers of carriers per particle. The carrier density vs. time traces of the short component were fit to equation (5.3). The fit results are also shown in Figure 5.6. Global fit results yield values for trap mediated recombination (A) and Auger recombination (C) rate constants. The values of A and C obtained from global fit are 3.40 (± 0.28) × 10^9 s^{-1} and 2.75 (± 13.9) × 10^{-29} cm^6 s^{-1}. These values are still very similar to those obtained for the previous samples. The Auger recombination rate constant appears larger, but within error it is still the same as the other values. The trap mediated recombination rate constant is larger than for the other samples. The initial lifetime of the trap mediated recombination is 294 ps in the nitrided $ZnGa_2O_4$ and was between 800 and 900 ps in the $(Ga_{1-x}Zn_x)(N_{1-x}O_x)$ samples. Trap mediated recombination occurs faster in these small aggregated particles. Perhaps this could be a result of faster trapping and potentially a greater amount of defects. We also note that the x value or Zn content is much smaller (~0.2) in this sample than the

previous samples studied. Perhaps higher Zn content allows for a longer trap mediated recombination lifetime. We have gained a better understanding of how elemental distribution does not play a major role in the recombination dynamics of $(Ga_{1-x}Zn_x)(N_{1-x}O_x)$, however, the exact role of composition (x value) in the excited-state dynamics of these materials remains to be determined.

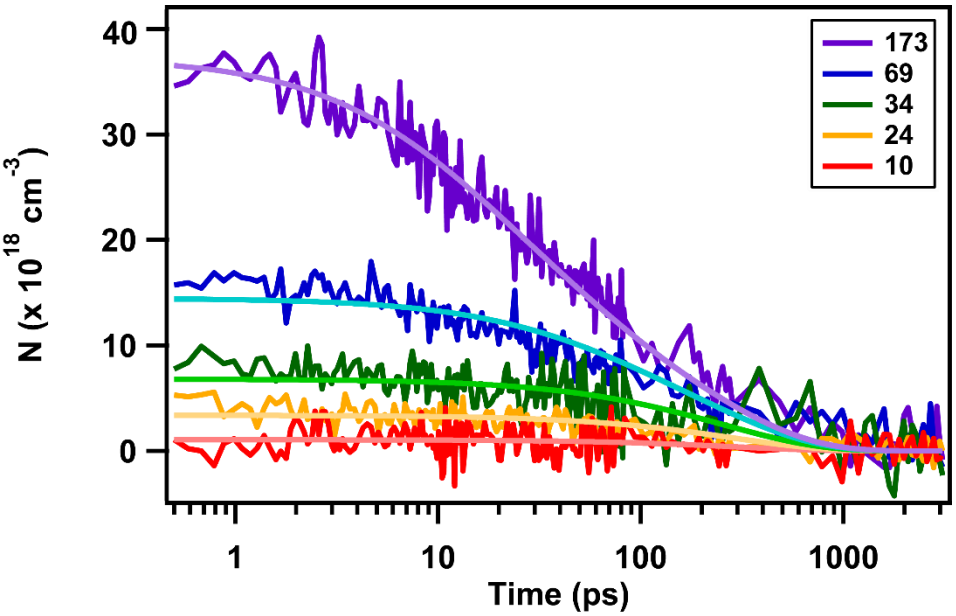

Figure 5.6. Extracted short component decay kinetics at various carrier densities for nitrided $ZnGa_2O_4$. The respective global fits to carrier recombination expression given in equation (5.3) are shown. Values for number of carriers per particle for each decay trace are given in the legend.

5.4.3 TA Spectroscopy of $(Ga_{1-x}Zn_x)(N_{1-x}O_x)$ Probed in the NIR

In order to gain more information about carriers in the excited-state of $(Ga_{1-x}Zn_x)(N_{1-x}O_x)$, we used a NIR probe to monitor the signal of free carriers generated in $(Ga_{0.6}Zn_{0.4})(N_{0.6}O_{0.4})$. NIR positive signals are often attributed to the generation of free carriers.[110-112] In particular, an increase in the absorption with increase of probe wavelength is indicative of free carrier absorption.[111,112] We observe such behavior in our NIR TA spectrum, which is shown in Figure 5.7 at various time delays after pumping with 340 nm. The peak around 1,360 nm is due to scattering that comes from the fourth harmonic generation of the signal from the OPA which is used to create the pump

wavelength of 340 nm. Studying the decay kinetics of the free carriers in the NIR could lend to a greater understanding of the carrier decay in the visible bleach that we have previously studied.

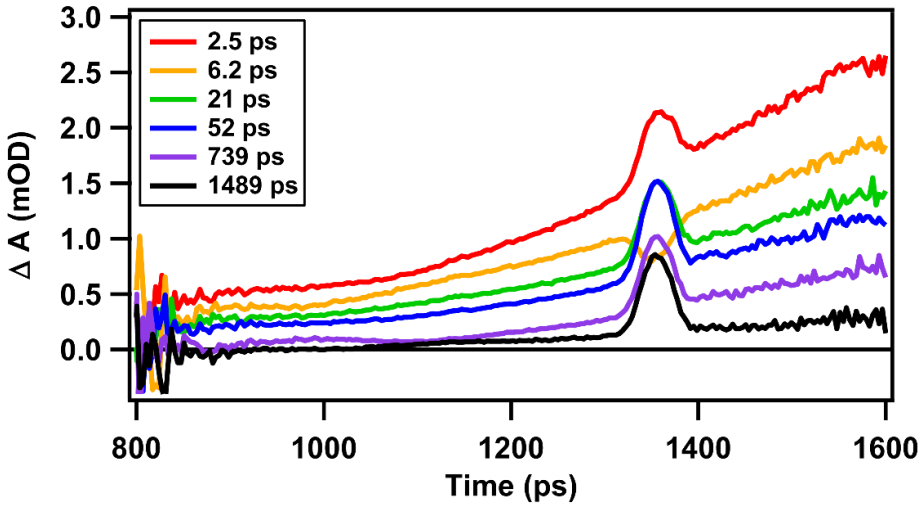

Figure 5.7. NIR TA spectra of $(Ga_{0.6}Zn_{0.4})(N_{0.6}O_{0.4})$ nanoparticles at various time delays. Time delays are shown in the legend.

The full spectrum obtained for $(Ga_{0.6}Zn_{0.4})(N_{0.6}O_{0.4})$ probed in the visible and NIR is shown in Figure 5.8. Again, we observe a broad bleach in the visible part of the spectrum and a positive feature in the NIR. The decay kinetics of the positive feature in the NIR (1200 nm) and the bleach maximum position (440 nm) are shown in the inset of Figure 5.8. Both decay traces exhibit an initial sharp decrease in signal. However, the NIR trace decays to zero in about 2 ns, while the visible has a longer lived decay component that has not reached zero by 8 ns. It appears as though the short component in the visible bleach has a very similar decay to the free carriers observed in the NIR. In fact, the NIR kinetics exhibit a power dependence that is very similar to the power dependence observed at the visible bleach. This is shown in Figure 5.9. Perhaps the free carriers observed in the NIR spectrum also recombine via trap mediated and Auger recombination. In the next section, we use electron scavenger experiments to gain more insight into the nature of these NIR signals.

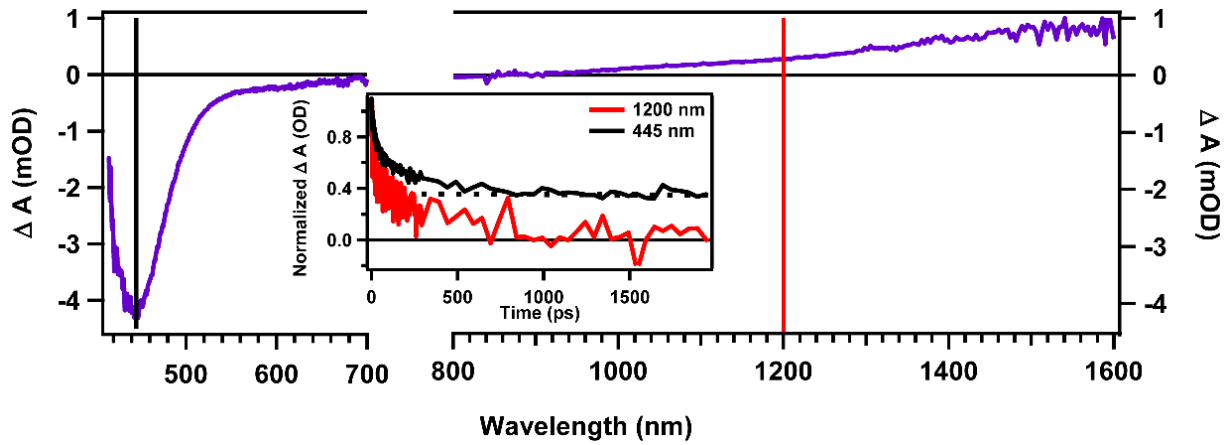

Figure 5.8. Full TA spectrum of $(Ga_{0.6}Zn_{0.4})(N_{0.6}O_{0.4})$ nanoparticles, where visible bleach and positive NIR feature are present. The inset shows normalized decay kinetics probed at the bleach (black) and in the NIR (red).

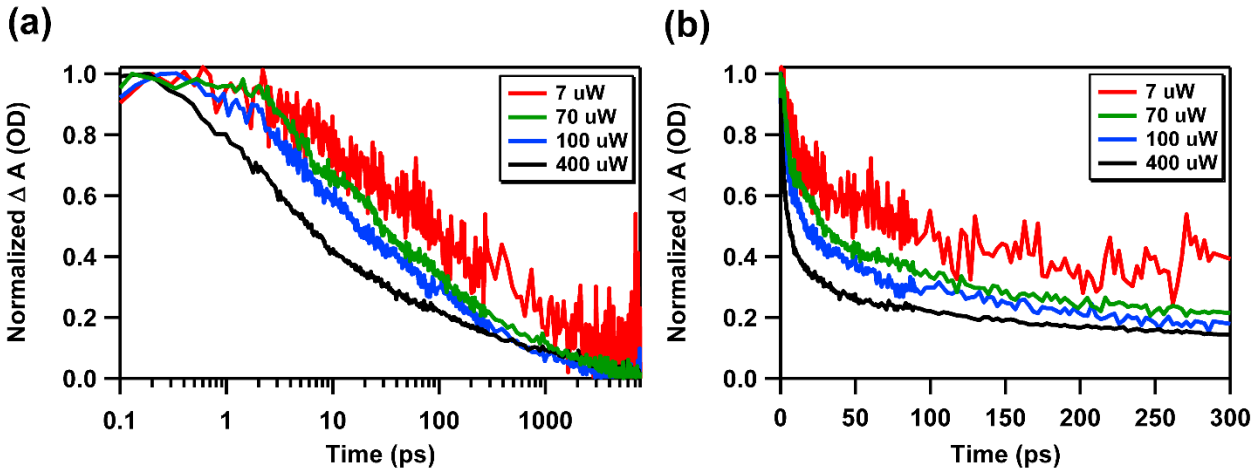

Figure 5.9. Power dependent kinetics of sample $(Ga_{0.6}Zn_{0.4})(N_{0.6}O_{0.4})$ probed at 1200 nm at various pump powers on a log scale (a) and zoomed in linear scale (b). Pump power values are shown in the legend.

5.4.4 Scavenger Experiments

In order to further understand the signals observed from TA spectroscopy and determine which carriers the signals are due, we performed an electron scavenger experiment, with methylene blue as the scavenger. Methylene blue (MB) is a commonly used electron acceptor.[113-116] To determine whether TA signals of $(Ga_{1-x}Zn_x)(N_{1-x}O_x)$ arise from electrons, holes, or both, we combined MB in solution with the nanoparticles (in toluene) to monitor the signal once electrons were scavenged.

We measured the UV-VIS absorption spectra with and without the addition of electron scavenger to verify the presence of methylene blue in solution with the oxynitride nanocrystals, as shown in Figure 5.10. A peak between 600 and 700 nm is indicative of the methylene blue species in solution.[114,115]

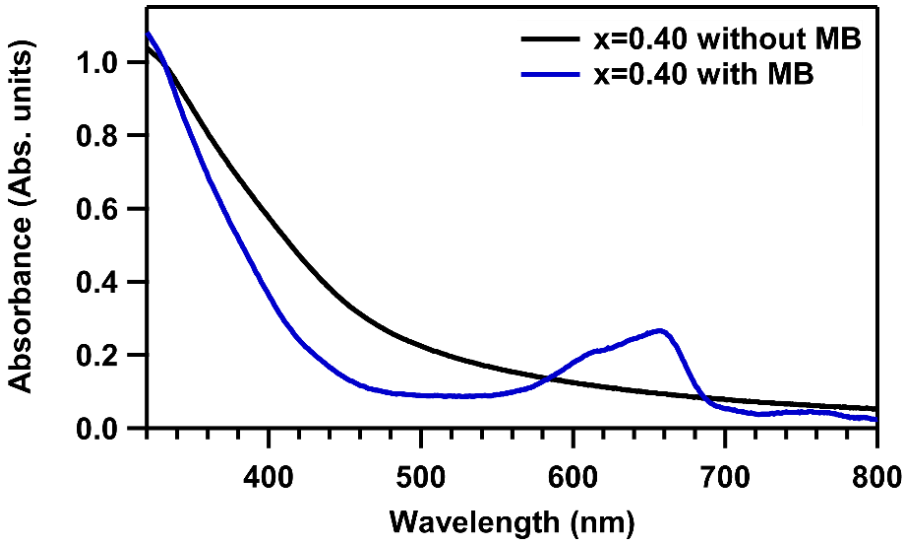

Figure 5.10. UV-VIS absorbance spectrum of $(Ga_{0.6}Zn_{0.4})(N_{0.6}O_{0.4})$ nanoparticles with methylene blue in toluene.

The TA spectra with and without addition of electron scavenger are shown in Figure 5.11a and the kinetics at oxynitride bleach maximum are shown in Figure 5.11b. In the TA spectrum with MB, we observed a small additional bleach at 670 nm. It is difficult to conclude whether this bleach is in fact due to electron transfer to MB, or simply noise from the probe signal in the experiment. However, this bleach resembles that of MB in MB-CdTe QD complexes.[113] We also find that the oxynitride bleach decays faster with the addition of MB. A faster decay with the removal of electrons indicates that the visible bleach signal has contributions from electrons. With addition of electron scavenger, it appears that the long-lived component disappears. Therefore, it is possible that the long-lived signal discussed in Chapter 4 is due to holes.

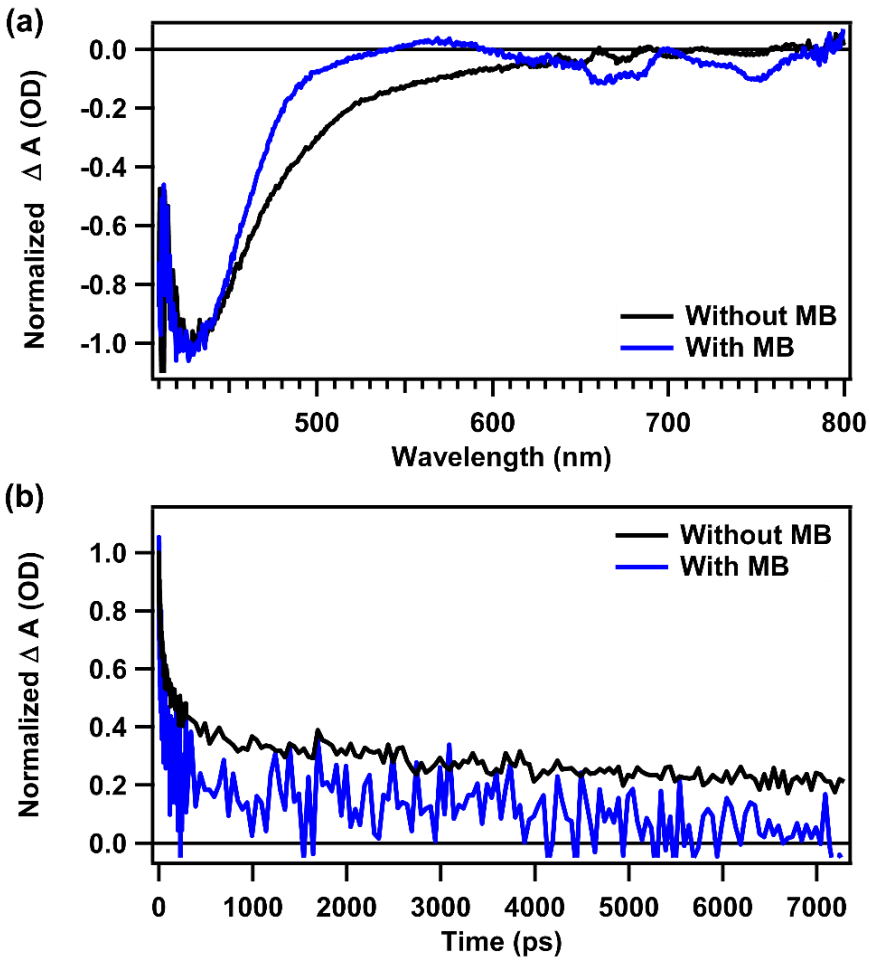

Figure 5.11. TA spectra of $(Ga_{0.6}Zn_{0.4})(N_{0.6}O_{0.4})$ with (blue) and without (black) addition of MB as an electron scavenger. (a) Bleach at 440 nm is due to oxynitride and bleach at 670 nm could be due to MB. (b) Bleach kinetics probed at 440 nm (oxynitride bleach maximum) with (blue) and without (black) addition of MB.

We also monitored the kinetics probed in the NIR with the addition of an electron scavenger (MB) and found that the decay kinetics do not change. Therefore, the signal probed in the NIR is more likely due to holes than electrons. When monitoring the decay kinetics of the NIR signal, the short component of the visible bleach, and the visible bleach kinetics with addition of MB, we found that they are all very similar, as presented in Figure 5.12. Knowing that the NIR signal matches the short component of the visible kinetics and the signal with the electron removed, the short component in the visible kinetics could also be due to hole signal. Therefore, the long-

lived signal could be due to the decay of an electron in the bleach. Our current hypothesis is that the NIR signal is due to one carrier, the hole, which gets trapped, and the other carrier, the electron, remains as the long-lived bleach signal as it decays. The assignment of the long-lived signal to a single carrier decay, after the trapping of the hole, is in accordance with the assignment of the long-lived signal to a trap-limited recombination, as discussed in Chapter 4. More experiments and analysis need to be performed in order to more conclusively assign all of these signals. For example, a hole scavenger experiment should also be performed. In addition, an electron scavenger experiment with an electron acceptor that is soluble in toluene, but still accepts electrons from the oxynitride would be beneficial. It is difficult to interpret the noisy signals that result from scattering due to MB not being completely in solution in our current experiments.

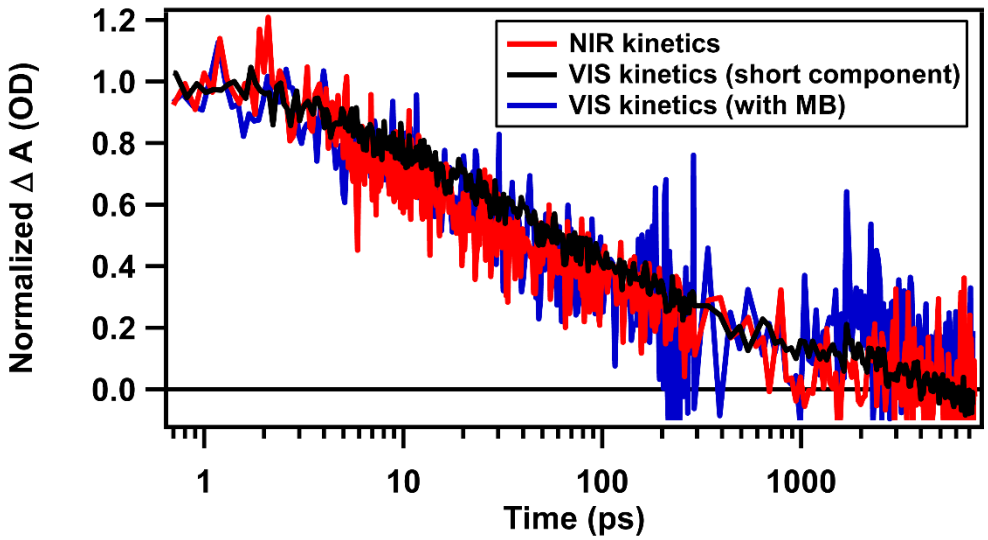

Figure 5.12. Normalized decay kinetics probed in the NIR (1200 nm), visible bleach kinetics probed at 440 nm with MB (blue), decay kinetics of the extracted short component without MB (black).

5.5 Conclusions

New multinary complexes are continuing to emerge for use in applications for solar fuel generation. Many of these complexes are synthesized using solid-state methods, such as the

synthesis of $(Ga_{1-x}Zn_x)(N_{1-x}O_x)$ nanoparticles. With new materials synthesized with increased compositional complexity, many properties of these materials, such as excited-state behavior, are not well understood. We used femtosecond transient absorption spectroscopy to understand the carrier dynamics in various $(Ga_{1-x}Zn_x)(N_{1-x}O_x)$ nanoparticles. First, we found that particles with different elemental distributions did not have largely different decay dynamics. In particular, we fit carrier density-dependent kinetics to a recombination model, which resulted in determination of the trap mediated and Auger recombination rate constants in these particles. The values for the recombination rate constants obtained were all within error of one another for both homogeneous and heterogeneous samples. Another sample studied here was nitrided $ZnGa_2O_4$, which behaves similarly to $(Ga_{1-x}Zn_x)(N_{1-x}O_x)$ nanoparticles, but particles have smaller size and a crystal structure that might be the combination of wurtzite and spinel, as opposed to just wurtzite. We found that these particles still have very similar decay dynamics to other $(Ga_{1-x}Zn_x)(N_{1-x}O_x)$ nanoparticles, with a somewhat faster trap mediated recombination lifetime.

We also studied TA spectra of $(Ga_{1-x}Zn_x)(N_{1-x}O_x)$ probed in the NIR and used methylene blue as an electron scavenger to determine the nature of TA signals. We found that upon addition of electron scavenger, visible decay kinetics resemble the fast component described here and in detail in Chapter 4. In addition, the free carrier NIR decay kinetics also match this decay. Therefore, we predict that the short component decay signal is due to holes, while the long-lived decay is due to electrons. In particular, the free carrier signal observed in the NIR is due to a hole that gets trapped, and subsequently, the electron signal remains in the bleach and decays. This supports the assignment of the long-lived signal to a trap-limited recombination, as we discussed in Chapter 4. Many details of the excited-state dynamics in these complex materials remain to be determined.

Chapter 6. Transient absorption investigation of electron transfer during photochromism in mesoporous TiO_2 filled with silver nanoparticles.

6.1 Introduction

Photochromism of silver species associated with titania is a well-known phenomenon.[117-119] Upon illumination, the material changes color. Conventional photochromic materials usually respond to one wavelength, but Ag-TiO_2 exhibits multicolor photochromism.[120,121] In other words, the color change varies depending on the wavelength of illumination. This improves the number of possible applications with Ag-TiO_2, including smart windows and rewritable color paper.[122] Further applications with metal nanoparticles embedded in a semiconductor include solar fuel generation, photovoltaics, and photocatalysis.[41,123,124] Three phenomena are discussed for the interactions between NPs and semiconductors (SCs): plasmon induced charge separation (PICS), also called Direct Electron Transfer (DET),[125] the co-catalysis effect, and the plasmonic nanoantenna effect.[42] Understanding and identifying precisely which phenomenon occurs during the photochromism process is often an open challenge. PICS can be observed under visible illumination, where silver nanoparticles interact with light due to their surface plasmon resonance (SPR). The creation of hot electrons with enough energy to cross the Schottky barrier allows good charge separation,[126] with electrons in TiO_2 and holes in Ag. When silver is oxidized to Ag^+, sample bleaching is observed. Under UV light, the co-catalysis effect is mainly observed, where electrons from the valence band (VB) of titanium dioxide are excited to the conduction band (CB) and then migrate to Ag NPs, allowing a reduction of the present Ag^+ species.[127] The plasmonic nanoantenna effect occurs when plasmonic NPs and semiconductor are not in direct contact but at a small distance (around 10 nm)

from each other. The localized surface plasmon resonance (LSPR) of NPs enables a transfer of electromagnetic energy back and forth at a short distance around the NPs.[128]

Distinction between these three phenomena often depends on the different excitation wavelengths used and the distances between plasmonic NPs and the semiconductor. However, the distinction between these processes is often misunderstood.[42] We proposed here to use transient absorption (TA) spectroscopy to distinguish which process is observed in the interaction of Ag nanoparticles and TiO_2. TA spectroscopy is a method used to observe the evolution of electrons and holes in photoexcited materials.[128,129] In this method, the sample is pumped with short pulses of light, and the kinetics of the evolution of excited species can be monitored by the change in absorption at a specific wavelength (UV or visible) as a function of the time delay between pump and probe pulses. Following the evolution of the electron and/or hole decays should give an idea of which of the three phenomena, discussed above, are involved. In PICS, an electron transfer is expected from Ag NPs to TiO_2 upon visible light illumination. For the co-catalysis effect, the inverse transfer is expected under UV light illumination. Finally, for the plasmonic nanoantenna effect, no transfer should be observed.

The study of Ag-TiO_2 films is relatively scarce using TA spectroscopy. A number of studies on TiO_2 films have been made by Durrant and Tachiya. The impact of morphology and phase of TiO_2 on its photo activity has been largely studied.[130-133] The identification of holes and electrons, free or trapped, has been possible using chemical scavengers.[134,135] Signals due to holes are situated around 500 nm, whereas trapped electron signals are found around 800 nm and free electrons after 1000 nm.

Studies of colloidal solutions of NPs (Ag or Au) have shown mechanisms involved in plasmonic relaxation. After excitation, SPR lifetime is ruled by 4 processes; electron dephasing

(10-100 fs), electron-electron scattering (100-1000 fs), electron-phonon scattering (1-10 ps) and heat transfer (10-100ps).[136] Contact between NPs and a SC add another potential mechanism for electron relaxation, i.e charge transfer.[137]

The combination of TiO_2 with Au NPs has been investigated in films and colloid solutions.[125,137-139] The Tachiya team has worked on studying the electron transfer from gold nanodots to TiO_2, which is observed due to a strong intraband absorption in the IR region.[140] The usual spectral feature observed after exciting TiO_2-Au (film or colloidal) with 400 nm, is a positive absorption band centered near 480 nm followed by a negative absorption band (bleach) around 550 nm.[137] The peak at 480 nm corresponds to the well-established interband transition region of gold NPs. The bleaching at 550 nm is consistent with the depletion of plasmon electrons.

While TA spectra of Au-TiO_2 have been somewhat extensively studied, TA spectra of Ag-TiO_2 films still require more investigation. One of the closest studies involved the deposition of Ag or Au nanoparticles on an alumina substrate that were monitored using femtosecond TA spectroscopy.[141] Ag NPs exhibit a transient response, with a bi exponential decay: one fast (1.5ps) corresponding to electron-phonon interactions and a long one (75ps) corresponding to a slower phonon-phonon interaction. Kamat *et al* studied Ag@TiO_2 core-shell composite clusters after UV irradiation using nanosecond laser flash photolysis probed on the microsecond time scale. They found that upon excitation of the TiO_2 shell, charge transfer to the Ag core was complete within the laser pulse duration of a few nanoseconds.[142]

Here, we choose to focus on studying the TA spectra of an Ag-TiO_2 film. We can study the transient absorption time profiles from a few picoseconds to 3 nanoseconds with a laser pulse resolution of 100 femtoseconds. Studying the decay dynamics on this shorter timescale, we sought to quantify the electron transfer that occurs during photochromism in the film of mesoporous TiO_2

filled with silver nanoparticles. We observed the TA spectra of an Ag-TiO_2 film after UV illumination (300 nm) and visible illumination (450 nm). We were able to quantify the electron transfer from TiO_2 to silver upon UV illumination as occurring within 2 ps. We also observed a strong interaction between Ag nanoparticles and TiO_2 upon visible illumination. We could not conclusively quantify the electron transfer from Ag to TiO_2 after visible illumination, but we had data to support a direct electron transfer mechanism.

6.2 Materials and Methods

6.2.1 Materials

A polyethylene oxide-polypropylene oxide-polyethylene oxide block copolymer, Pluronic® P-123 ($(EO)_{20}$-$(PO)_{70}$-$(EO)_{20}$), tetraorthobutyltitanate ($Ti(OBu)_4$, TBT), silver nitrate ($AgNO_3$), formaldehyde (CH_2O) were all purchased from Sigma Aldrich and used as received. HCl 37% was purchased from Carlo Erba.

6.2.2 Synthesis of Ag-TiO_2 films

The synthesis of Ag-TiO_2 films is described in full detail in Chapter 2.

6.2.3 Characterization

Scanning electron microscopy (SEM) images were obtained using a Zeiss Merlin Compact SEM with an in-lens detector at a low acceleration voltage of 5 kV. Energy dispersive X-ray analysis (EDX) was used to determine the amount of silver within the TiO_2 film.

Transmission electron microscopy (TEM) was performed on a JEOL 2100F field emission instrument operating at 200 keV. In a typical procedure, TiO_2 -Ag film fragments of non-controlled thickness were stripped off by scratching the samples with a razor blade and were then deposited on a carbon-coated copper grid.

UV-Vis spectroscopy measurements were performed with a Safas UVmc spectrometer measuring absorbance from films under direct incidence. Scans were measured between 300 and 1000 nm, with a 2 nm resolution.

6.2.4 Transient Absorption Spectroscopy

The transient absorption (TA) setup was previously described in full detail in Chapter 2 and previously published.[67] TA measurements were obtained using an amplified Ti:sapphire laser (Solstice, Spectra-Physics, 800 nm, 100 fs), an optical parametric amplifier (TOPAS-C, Light Conversion), and the HELIOS spectrometer (Ultrafast Systems, LLC), for measurements of the short timescale of 100 fs to 3 ns. A sapphire plate was used to generate the white light continuum probe pulse (450-800 nm). The TA experiments were all carried out at room temperature. All of the TA spectra were background subtracted and time zero corrected.

6.3 Results and Discussion

6.3.1 Characterization of the Samples

Here, we focus on studying Ag-TiO_2 films prepared on a quartz substrate using transient absorption spectroscopy. The films were prepared on quartz due to its optical clarity. In other words, the quartz does not absorb the wavelengths of interest necessary for visible absorption experiments. Steady state absorption spectra of TiO_2 and Ag-TiO_2 on quartz are shown in Figure 6.1a. Below 400 nm, the TiO_2 ultraviolet (UV) absorption is evident in both traces with and without silver nanoparticles. The Ag-TiO_2 absorption exhibits a broad peak between 400 and 600 nm with a maximum at 490 nm. This broad absorption is due to a surface plasmon resonance effect from silver NPs inside TiO_2 and is dependent on the particle size, shape, and particle substrate.[143] As previously determined, this broadened and red-shifted plasmon band, in relation to silver NPs in silica or water, is observed due to the high dielectric constant of TiO_2.[142,144] The broad peak width

in the absorption spectrum is also attributed to a large size distribution of the NPs.[119,144,145] This broad distribution is also observed in TEM and SEM images shown in Figure 6.1c and Figure 6.1d, respectively. XRD in Figure 6.1b shows peaks characteristic of Ag and TiO_2. In particular, the peaks at 34º and 52º are characteristic of Ag-TiO_2.[146]

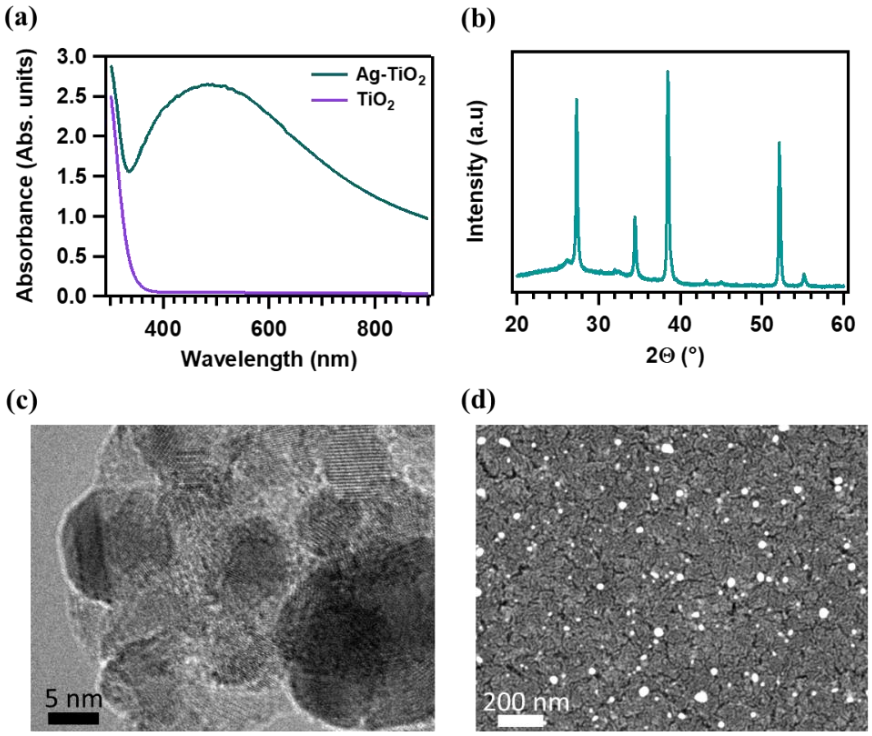

Figure 6.1. (a) Absorbance spectra of TiO_2 on quartz and Ag-TiO_2 film on quartz. (b) XRD pattern of Ag-TiO_2 film. (c) TEM image of Ag nanoparticles on mesoporous TiO_2. (d) SEM image of Ag nanoparticles (bright, white spots) on worm-like mesoporous TiO_2 surface.

6.3.2 TAS Results: Excitation with UV Light

First, we focused on studying the electron transfer from TiO_2 to silver in the Ag-TiO_2 film upon excitation with UV light. UV light allows for the excitation of an electron into the conduction band of TiO_2 which could then transfer into the silver NPs. Samples for these experiments were all pumped with 300 nm. There was no TA response from the quartz substrate (Figure 6.2).

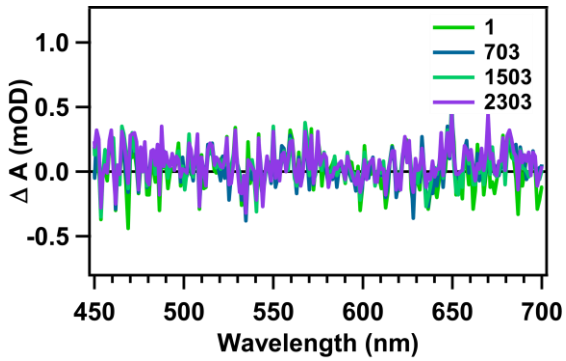

Figure 6.2. Transient absorption spectrum of bare quartz substrate, at various time delays, pumped at 300 nm. There is no signal from quartz upon UV illumination.

In order to better understand the transient absorption response from Ag-TiO_2, we first sought to observe the TA spectra of TiO_2 alone, pumped at 300 nm. Decay kinetics were independent of pump power below 100 uW (Figure 6.3). Experiments were carried out with a 300 nm excitation wavelength with 90 uW pump power, to maximize signal-to-noise, without introducing power dependent effects.

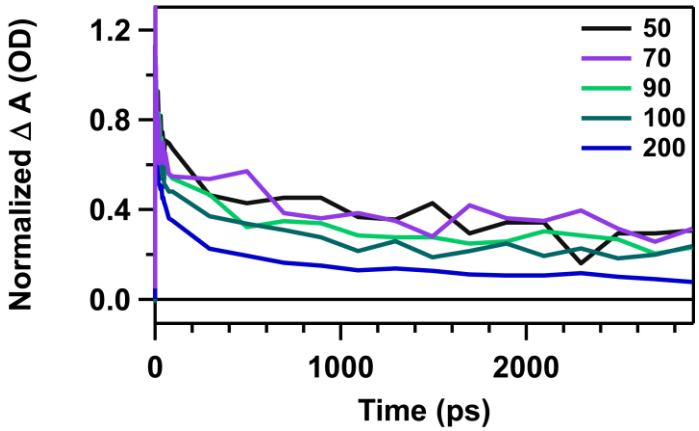

Figure 6.3 Normalized power dependent kinetics of TiO_2 on quartz pumped at 300 nm and probed at 620 nm. Pump power values in legend are given in uW. A pump power dependence is observed at pump power greater than 100 uW, therefore experiments were conducted at 90 uW pump power.

Figure 6.4a shows a broad positive feature between 450 and 700 nm as it decays over time, which agrees with previously observed TA spectra of TiO_2.[147] The decay kinetics did not appear to change between 450 and 700 nm. Understanding the signal produced by carriers in TiO_2 upon excitation with UV light is important to realizing the spectral differences upon addition of Ag NPs.

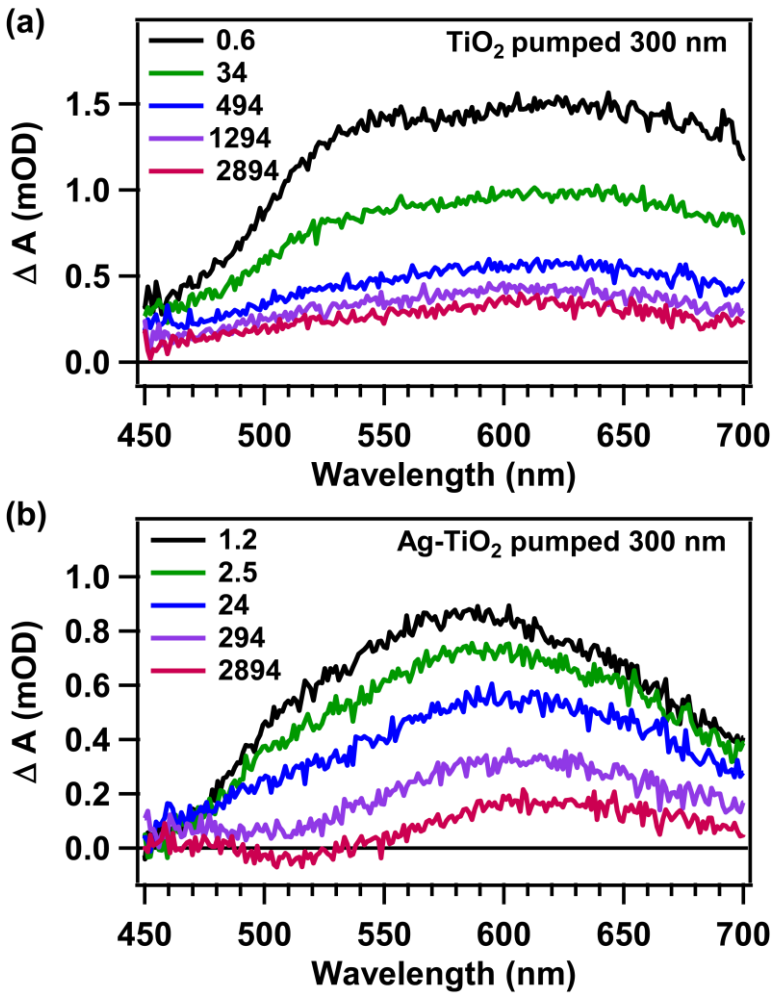

Figure 6.4 TA spectra of TiO_2 (a) and Ag-TiO_2 (b), pumped at 300 nm, at various time delays. Time delays are shown in the legend in ps.

In the presence of Ag NPs, the TA signal changes, as evidenced by the TA spectra in Figure 6.4b, where there is a new feature present at 520 nm. Data was collected with a pump power of 90 uW at 300 nm, just as for the TiO_2 spectra. The difference observed in the spectra with addition of Ag NPs could be a result of electron transfer from the conduction band in TiO_2 to the Ag NPs. Signal from Ag only on quartz substrate, pumped with 300 nm, was negligible, as shown in Figure 6.5, meaning that Ag NPs do no absorb UV light. Therefore, in order to have a change in signal with Ag NPs incorporated in TiO_2, electrons must be transferring from TiO_2 to the Ag NPs. To examine

the difference in the spectra with and without Ag NPs, we performed a Global Fitting analysis to extract information about the various contributions in the Ag-TiO_2 spectrum.

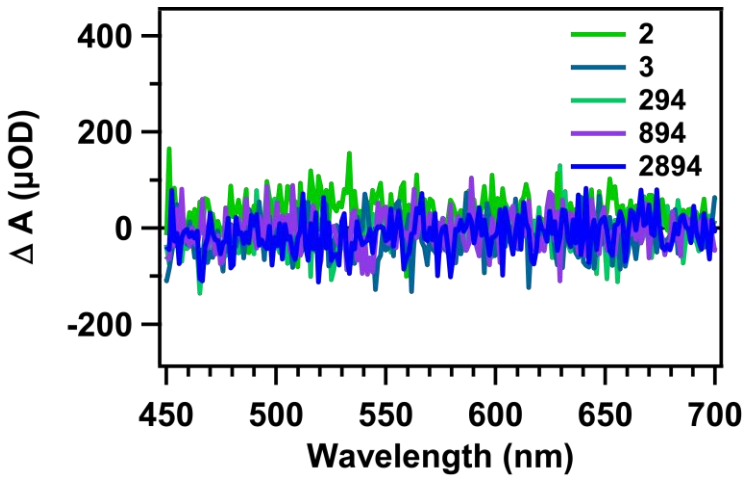

Figure 6.5. Ag nanoparticles alone on quartz, pumped at 300 nm. There is no signal from Ag upon UV illumination, indicating that Ag nanoparticles are not excited by 300 nm light. Values in legend are time delays given in ps.

Global fitting the decay kinetics at multiple probe wavelengths, of the Ag-TiO_2 data, to multiple exponentials, ultimately yielded spectral shapes which resembled the TiO_2 only spectrum, and an additional spectral shape that we would ultimately assign to the spectrum due to electrons transferred to Ag. Knowing that the contributions to the spectra shown in Figure 6.4b were solely due to the signal from TiO_2 (as observed in Figure 6.4a) and a contribution from Ag NPs, we could isolate the spectral shape of the electron transferred to Ag. By subtracting the TiO_2 spectrum from the Ag-TiO_2 spectrum, we obtain the resulting spectrum (purple) shown in Figure 6.6. The purple trace, which we believe is the spectrum due to the electrons in Ag, very closely resembles the spectral shape of electrons transferred to Au in TiO_2-Au nanocomposites.[137] This spectral feature indicates that upon UV light excitation, TiO_2 transfers its conduction band electron to Ag in the Ag-TiO_2 film.

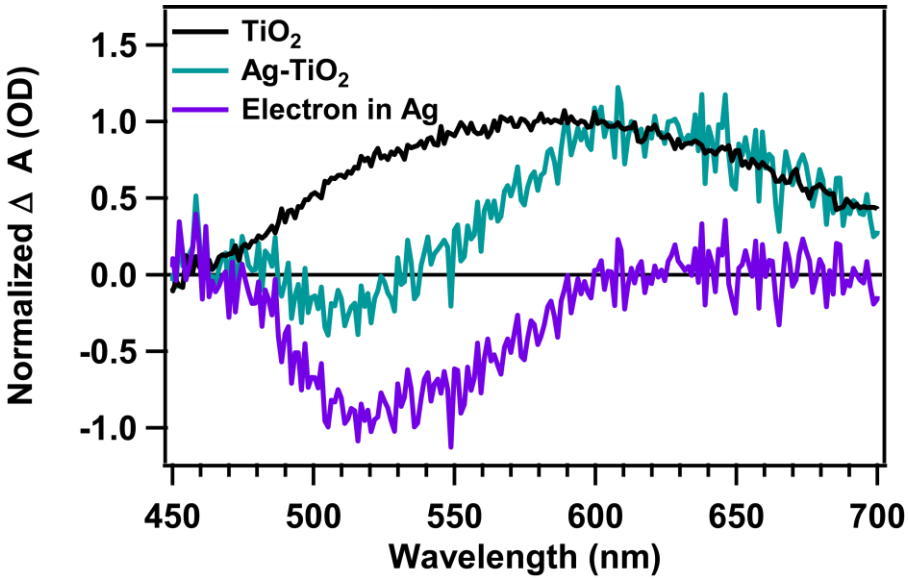

Figure 6.6. Spectral shapes of TiO_2 (black), Ag-TiO_2 (green/blue), and electron in Ag (purple). The purple trace was obtained by subtracting the experimental Ag-TiO_2 spectrum from the TiO_2 spectrum at 3 ns time delay.

To quantify the timescale of electron transfer from TiO_2 to Ag NPs, we used the extracted spectral shape of the electron in Ag and TiO_2 only, shown in Figure 6.6, and fit them to Gaussians. The spectral shape for the electron in Ag was fit with a single Gaussian, and the TiO_2 spectrum was fit to two Gaussians. The fit results are shown in Figure 6.7 and the fit parameters are summarized in Tables 6.1 and 6.2, for electron in Ag and TiO_2, respectively.

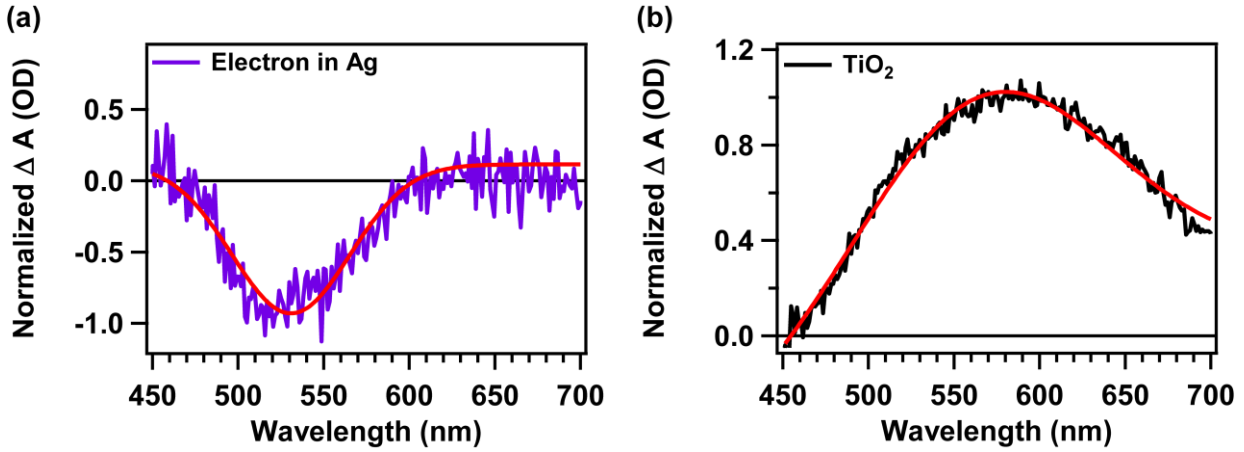

Figure 6.7. Extracted spectral shape of electron in Ag fit to a single Gaussian (a) and TiO_2 spectrum excited with 300 nm, at 3 ns, fit to two Gaussians, where fits are shown in red.

Table 6.1. Fit parameters for a single Gaussian fit to the extracted spectrum of the electron in Ag, as shown in Figure 6.7a. A is the intensity, x_0 the Gaussian position, width the FWHM, and y_0 is the y offset.

Fit parameter	Value
A	-1.03 ± 0.03
x_0	530.8 ±0.9 nm
width	49.2 ± 2.2 nm
y_0	0.1 ± 0.03

Table 6.2. Fit parameters to a double Gaussian fit to the TiO_2 spectrum excited at 300 nm, as shown in Figure 6.7b. A is the intensity, x_0 the Gaussian position, width the FWHM, and y_0 is the y offset. Values for each labeled 1 and 2 are for each Gaussian.

Fit parameter	Value
A_1	1.2 ± 0.5
x_01	563.040 ± 0.005 nm
$width_1$	182.28 ± 0.002 nm
A_2	0.9 ± 0.4
x_{02}	774.100 ± 0.002 nm
$width_2$	396.210 ± 0.001 nm
y_0	-0.6 ± 0.7

Using Global Fit analysis, the TA spectra of Ag-TiO_2 were fit to equation (6.1), where A and B are coefficients for the single Gaussian fit of the electron transfer to Ag and the double Gaussian fit of TiO_2 respectively, x_i is the position, and w_i is the full width at half maximum (FWHM).

$$f(x) = A(e^{(\frac{x-x_1}{w_1})^2} + y_1) + B(B1 * e^{(\frac{x-x_2}{w_2})^2} + B2 * e^{(\frac{x-x_3}{w_3})^2} + y2) \quad (6.1)$$

Using parameters for the position and FWHM obtained from Gaussian fits of each spectral shape (results from Tables 6.1 and 6.2), while letting the coefficients A and B vary and linking the position and FWHM of each spectral component (i.e. ET and TiO_2 spectra), we could obtain the contribution of each component to the spectrum over time. Plotting the A and B coefficients as a function of time yielded kinetic traces for both the decay of TiO_2 and the electron transferring into

Ag. Figure 6.8a shows the decay of the TiO_2 component, and Figure 6.8b, the rise of the Ag component, as the electron is transferred.

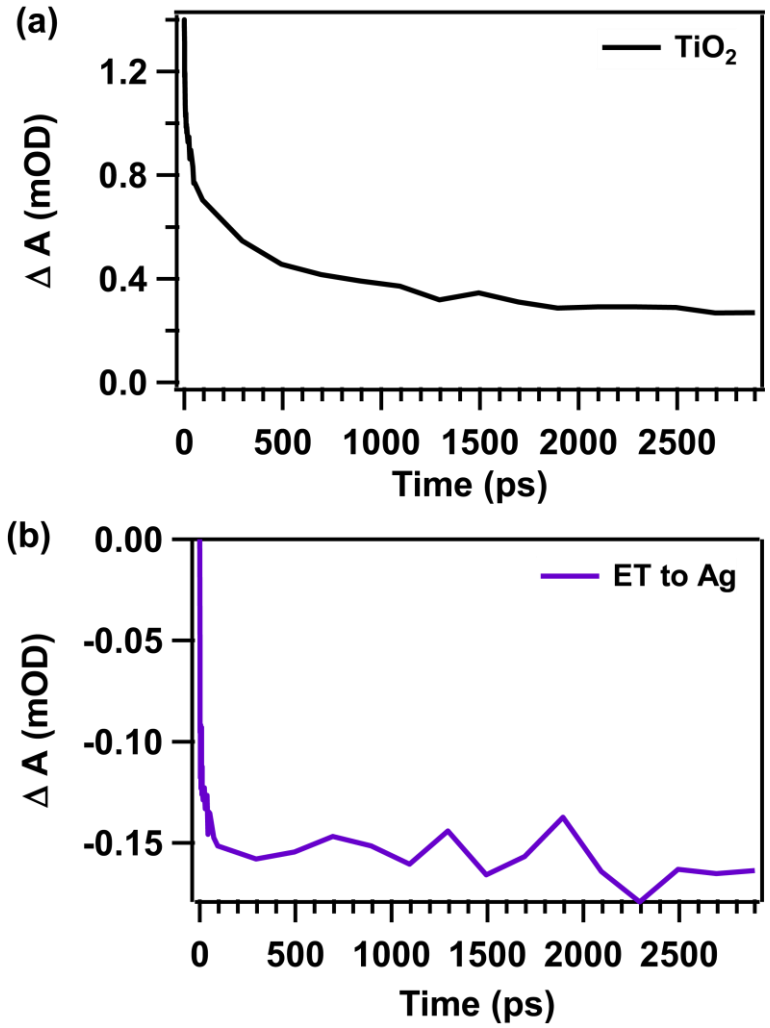

Figure 6.8. TiO_2 decay component obtained from global fitting analysis (a) and the global fit extracted rise of the Ag component as the electron is transferred from TiO_2 to Ag (b).

The electron transfer kinetic trace was fit to an exponential rise (equation (6.2)). The TiO_2 decay kinetic trace was fit to a multi-exponential decay (equation (6.3)), where i=3

$$F_{ET}(t) = 1 - e^{-\frac{t}{\tau_{ET}}} \tag{6.2}$$

$$F_{TiO2}(t) = \sum_{i=1}^{3} A_i e^{-t/\tau_i} \tag{6.3}$$

The value obtained for the fit of the electron transfer rise is approximately 2 ps. Therefore, the electron transfer to Ag NPs upon excitation of TiO_2 with UV light is approximately 2 ps. The fits to equations (6.2) and (6.3) are shown in Figures 6.9a and 6.9b, respectively. The fit results are summarized in Tables 6.3 and 6.4.

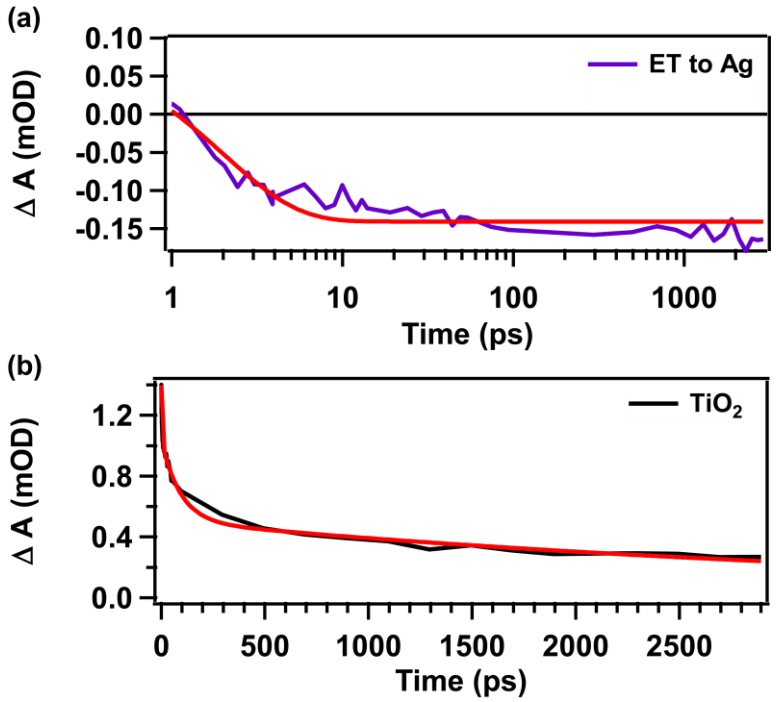

Figure 6.9. Rise of electron transfer to Ag, fit to an exponential rise expression as shown in equation (6.2) (a) and three exponential decay fit to the TiO_2 decay (b). Fits are shown in red.

Table 6.3. Fit parameters and values obtained from exponential rise equation (6.2) to kinetic rise of electron transferring to Ag from TiO_2, as shown in Figure 6.9a. A is a prefactor. Value of τ is the time it takes for electron to transfer into Ag from TiO_2 upon excitation with UV light.

Fit parameter	Value
A	$-1.41\ (\pm 0.03) \times 10^{-4}$
τ	2.03 ± 0.32 ps

Table 6.4. Fit parameters and values obtained from triple exponential decay equation (6.3) for decay of TiO_2, as shown in Figure 6.9b. Values of τ are decay times and A values are prefactors.

Fit parameter	Value
A_1	0.001 ± 2.160
τ_1	2.87 ± 0.35 ps
A_2	6 (± 343) × 10^{-4}
τ_2	90.93 ± 9.05 ps
A_3	5 (± 7) × 10^{-4}
τ_3	3897 ± 361 ps

To verify that the Global Fitting method used to determine the electron transfer time was self-consistent, we performed the Global Fit analysis on decay kinetics and obtained spectral shapes which matched those of TiO_2 and electron in silver spectra (Figure 6.10).

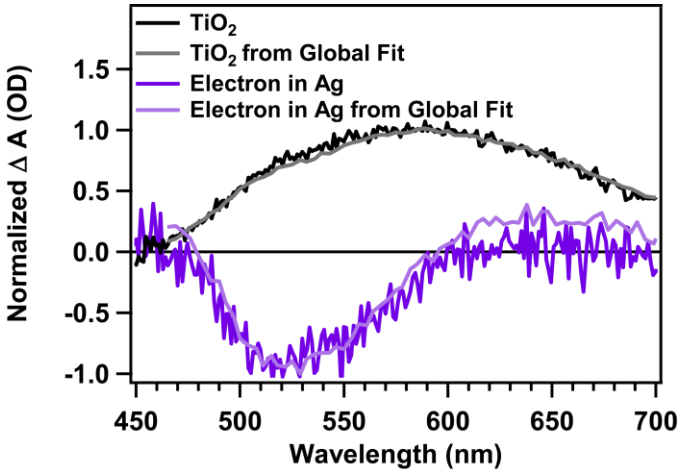

Figure 6.10. Comparison of spectral shapes obtained from experiment for TiO_2 (black) and electron in Ag (dark purple) with the spectral shapes obtained from global fit analysis for TiO_2 (gray) and electron in Ag (light purple).

Finally, Figure 6.11 compares the decay of TiO_2 only to the extracted kinetics of TiO_2 with the presence of Ag. We find that the decay with Ag NPs is faster than without. This faster decay upon addition of Ag to TiO_2 and excitation with UV light is suggestive of electron transfer from TiO_2 to Ag.

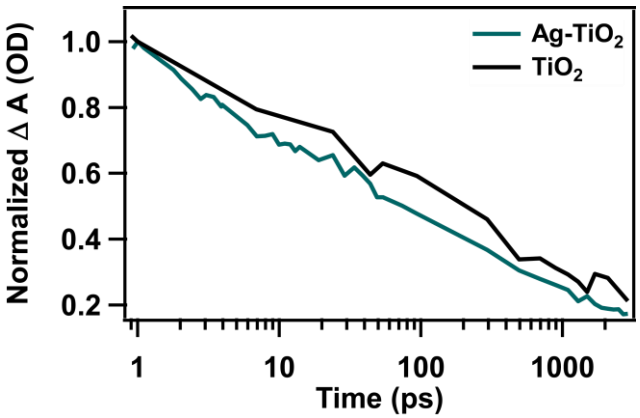

Figure 6.11. Decay of TiO_2 only, determined by excitation with 300 nm and extracted kinetics of TiO_2 only, in the presence of Ag. Faster decay of TiO_2 in the presence of Ag (blue trace) is indicative of electron transfer from TiO_2 to Ag.

By taking the quotient of the decay traces, we can observe where the decay is changing and where it is essentially the same (when the quotient trace is a constant value and levels off). The quotient of the two decay traces (Figure 6.12) indicates that the electron transfer occurs at 2.7 ps. This is within error of the value of 2 ps obtained from the exponential rise fit to the electron transfer kinetic trace. Thus, we confidently determined that upon UV illumination of an Ag-TiO_2 film, the electron transfer from TiO_2 to the Ag NPs occurs in approximately 2 ps. Such electron transfer supports the co-catalysis effect, where electrons are excited from the valence band to conduction band of TiO_2 and then electrons that accumulated in the TiO_2 conduction band transfer over to a co-catalyst, which in this case is Ag.[42] Other work studying Ag-TiO_2 systems found electron transfer from TiO_2 to Ag, but could only determine that it occurred within a ns, due to the time resolution of the experiment.[142]

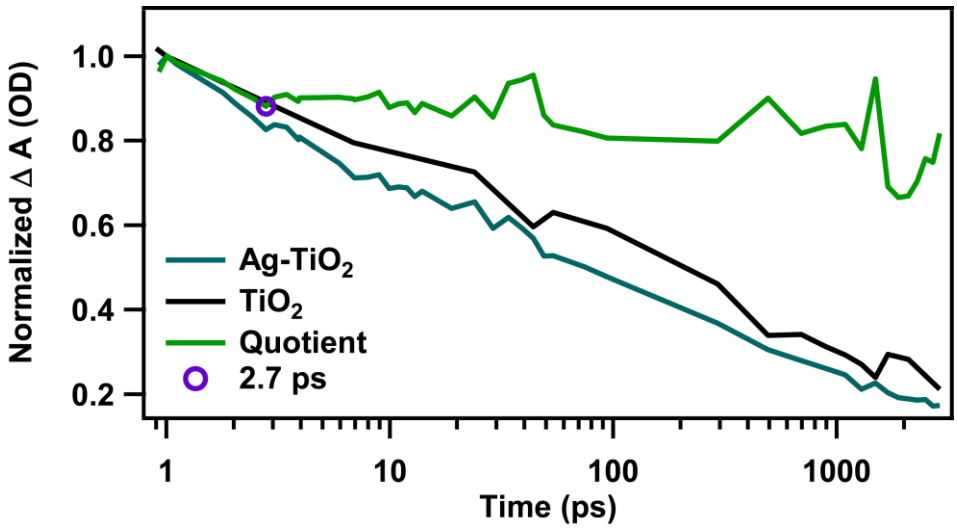

Figure 6.12. The quotient (green trace) of the decay of TiO_2 with (blue trace) and without Ag nanoparticles (black trace) is shown. Where the quotient levels out is marked with a purple circle which indicates the approximate time of electron transfer at 2.7 ps.

6.3.3 Excitation with Visible Light

When studying the TiO_2 film with Ag NP incorporation, we discovered that upon excitation with UV light, electron transfer from TiO_2 to Ag occurs in 2 ps. Next, we studied the behavior of the Ag-TiO_2 film with visible light illumination. To date, visible excitation of Ag NPs incorporated in TiO_2 has not been studied using transient absorption spectroscopy. In order to excite the SPR in Ag nanoparticles without exciting TiO_2, we chose to illuminate the sample with 450 nm. The quartz substrate and TiO_2 without Ag NPS exhibit no TA signal upon excitation with 450 nm, which is shown in Figure 6.13.

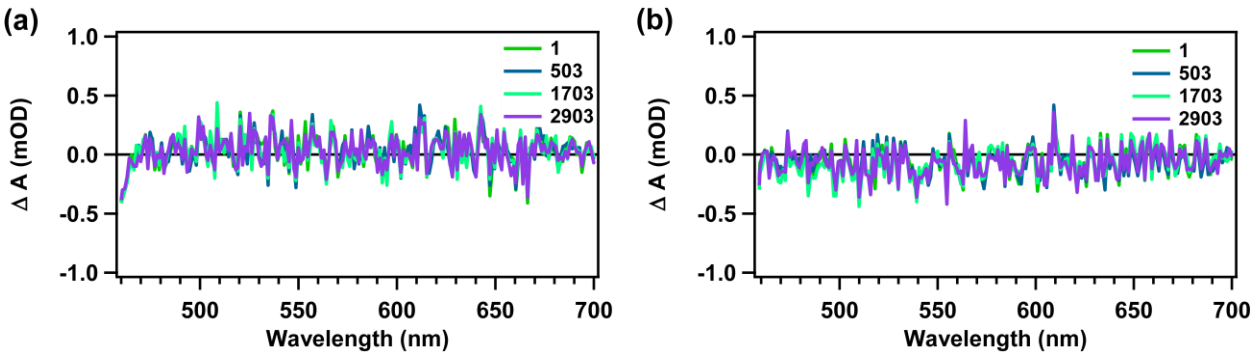

Figure 6.13. TA spectra at various time delays of quartz substrate alone pumped with 450 nm (a) and TiO_2 only on quartz pumped with 450 nm (b). The lack of signal is indicative of the fact that neither quartz nor TiO_2 are excited by visible illumination.

We observed the TA spectra of Ag-TiO_2 with 450 nm excitation at various time delays, as shown in Figure 6.14. A negative feature between 450 and 550 nm was assigned to the plasmon bleach from Ag nanoparticles. This bleach feature is similar to that seen in Au-TiO_2 systems pumped in the visible region and also the plasmon bleach observed in Ag@TiO_2 core-shell composite clusters after UV irradiation.[142]

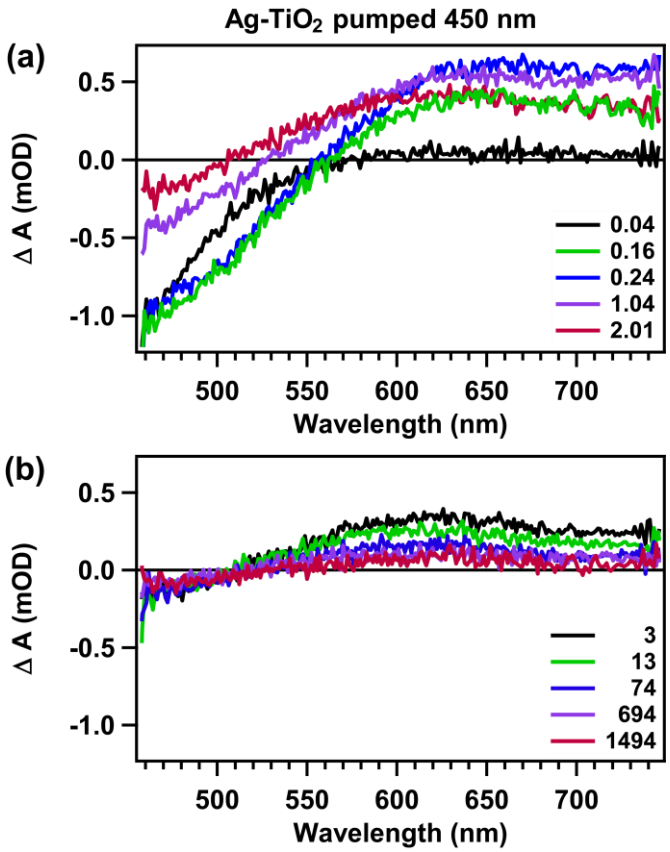

Figure 6.14. TA spectra of Ag-TiO_2 film pumped with visible light (450 nm) at short time delays from 0.04 to 2.01 ps (a) and longer time delays from 3 to 1494 ps.

A positive feature between 550 and 750 nm was also present in the TA spectrum. This positive feature rises within the first ps, which is evident when observing the spectra at various time delays in Figure 6.14a. This signal then decays, which is evident from the spectra in Figure 6.14b. Because this positive signal rises after the negative Ag plasmon signal, it is likely that the positive signal is due to the electrons trapped within TiO_2. In particular, the positive feature that is observed upon visible illumination, directly matches the TiO_2 feature observed upon UV illumination of the Ag-TiO_2 film, which is shown in Figure 6.15. This positive feature from 550 to 700 nm has been attributed to residual electrons trapped within TiO_2 nanoparticles.[142] Upon visible excitation (450 nm), electrons in TiO_2 are not excited, as we showed in Figure 6.13. Therefore, it appears that in order for the positive signal to be present in the TA spectrum of Ag-

TiO_2 excited with 450 nm, the electron must have transferred to TiO_2 to show this trapped electron signal.

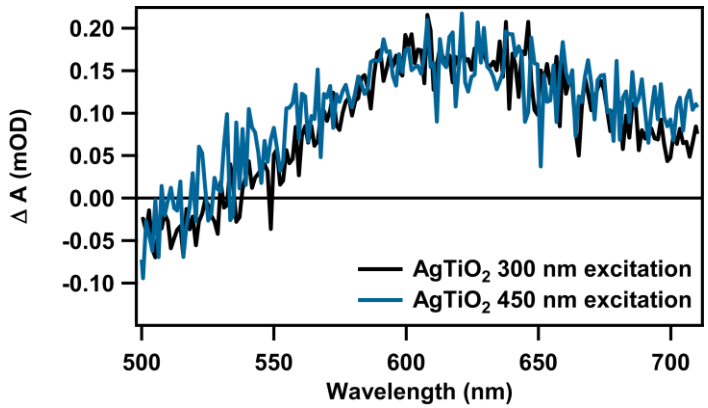

Figure 6.15. TA spectrum of Ag-TiO_2 with visible illumination (blue trace) and UV illumination (black trace). Similar spectra indicate that the positive feature in the visible excited trace could be due to electrons transferred from Ag to TiO_2.

However, it is more difficult to quantify the electron transfer from Ag to TiO_2 than from TiO_2 to Ag. This is because of the contribution that comes from exciting Ag with 450 nm light. Upon visible illumination, Ag behavior differs in the presence of a semiconductor like TiO_2 due to the formation of a Schottky barrier between the metal and semiconductor.[139] Therefore, comparing the TA spectra of Ag with and without TiO_2 is not as simple as the comparison when exciting TiO_2 alone with 300 nm and then with addition of Ag. Figure 6.16 shows the TA spectrum of Ag nanoparticles alone on the quartz substrate, excited with 450 nm. The positive induced absorption at 500 nm resembles the spectrum for Ag nanoparticles supported by Alumina.[141]

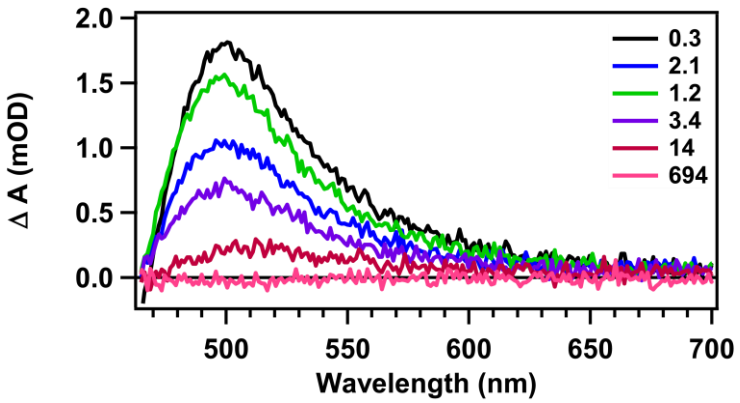

Figure 6.16. TA spectra at various time delays of Ag nanoparticles alone on quartz substrate at various time delays. Photoinduced absorption peak is evident at 500 nm. Values in legend are time delays given in ps.

We observed the decay of the induced absorption feature, which is shown in Figure 6.17. A biexponential decay fit of this kinetic trace yielded a fast component of 2.7 ± 0.1 ps and a long component of 58 ± 46 ps. These values are also in agreement with values obtained in the Ag nanoparticles supported by Alumina.[141] The fast component was attributed to electron-phonon interactions and the long component to slower phonon-phonon interactions. These processes must also be occurring in the Ag-TiO_2 samples. A global fit was performed to extract out contributions from Ag only and contributions from the electron transfer, however this did not yield useful results because the spectral shapes obtained did not have distinct features. It is possible that the electron transfer it too fast to observe in the timescale of the measurement.

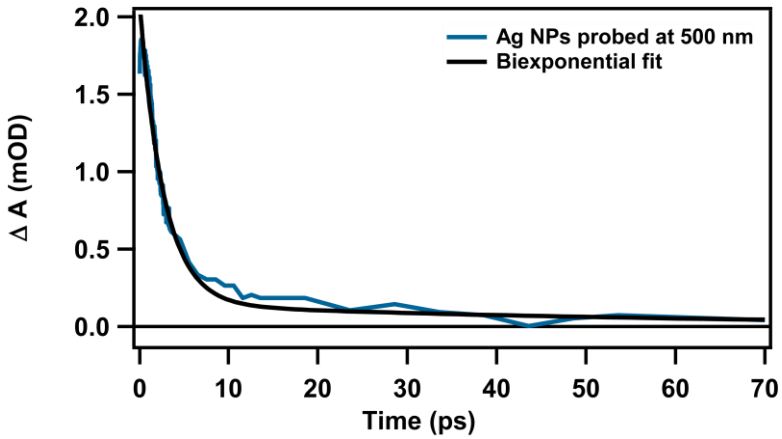

Figure 6.17. Decay kinetic trace of the induced absorption feature at 500 nm for Ag NPs only excited at 450 nm. Black trace shows a biexponential fit to the decay trace (blue).

It is also possible that the shape of the Ag-TiO_2 transient absorption spectrum, excited at 450 nm, is a result of a strong blue shift of the Ag SPR bleach due to the interaction of Ag nanoparticles with TiO_2. For Au nanoparticles in TiO_2, the plasmon band was approximated by a Gaussian function and the temporal evolution of the transient absorption spectra was approximated by a difference of Gaussian functions in order to observe spectral changes due to the shift of the Gaussian peak, as shown in equation (6.4).[130]

$$\Delta A(\omega, t) = \frac{P_{abs}(t)}{\sqrt{2\pi\omega(t)^2}} \exp\left(-\frac{1}{2}\frac{(\omega-\Omega_{SPR}(t))^2}{\omega(t)^2}\right) - \frac{P^0_{abs}}{\sqrt{2\pi\omega_0^2}} \exp\left(-\frac{1}{2}\frac{(\omega-\Omega^0_{SPR})^2}{\omega_0^2}\right) \quad (6.4)$$

In this equation ω_0 and $\omega(t)$ are bandwidth, $\Omega_{SPR}{}^0$ and $\Omega_{SPR}(t)$ are central frequencies or positions of the SPR band, and $P^0{}_{abs}$ and $P_{abs}(t)$ are the plasmon peak intensity, before and after laser excitation, respectively. We measured the absorbance of Ag-TiO_2 before excitation to include as constant fit parameters and the values after excitation were variables for fitting. The results of fitting the transient absorption spectrum at early time delays to equation (6.4) are shown in Figure 6.18. The fits accurately modeled the experimental results.

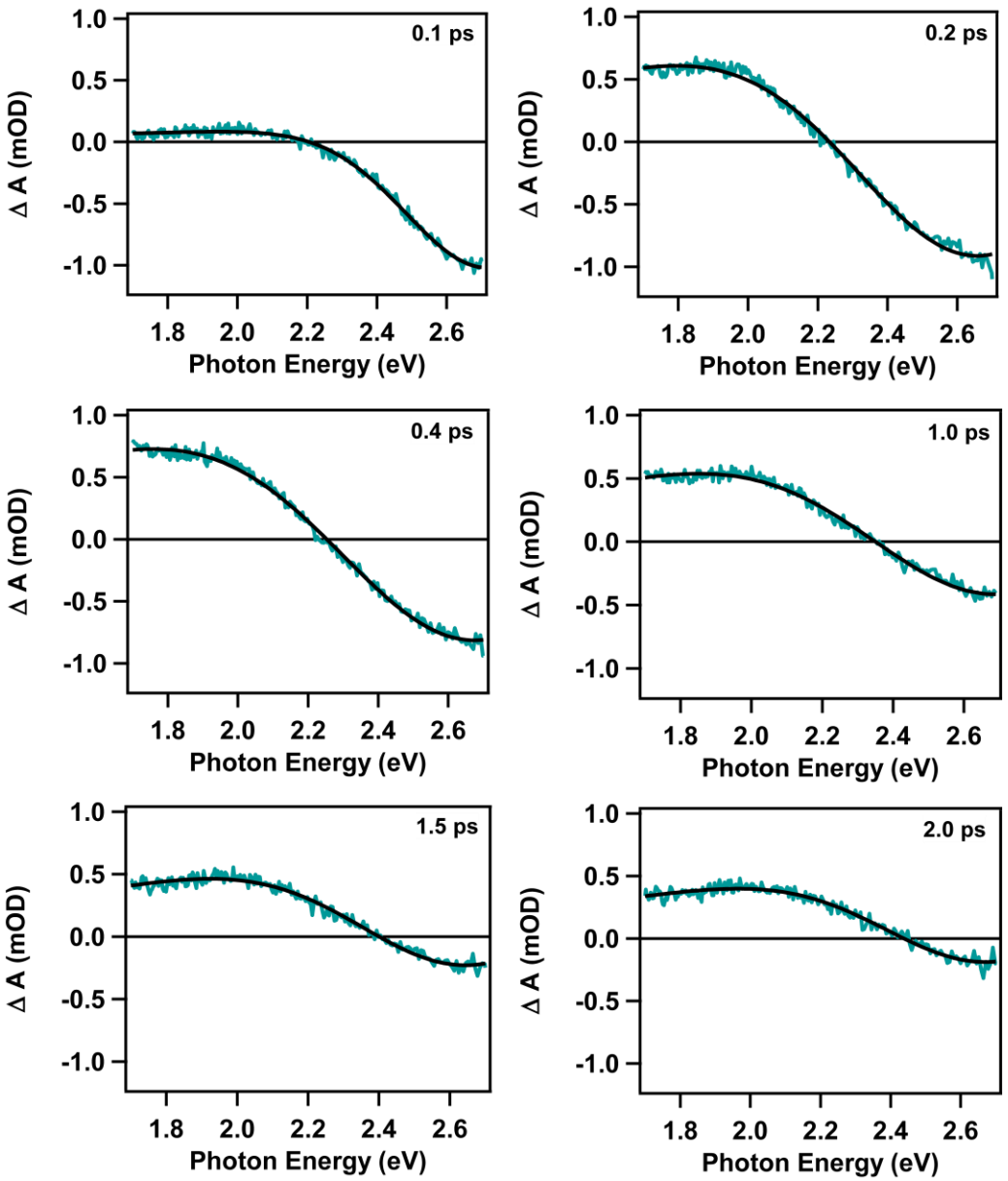

Figure 6.18. Fitting of TA spectra to a difference of Gaussian functions as shown in equation (6.4). Black traces are the fits.

Figure 6.19 shows the time dependence of ω(t) and $\Omega_{SPR}(t)$ after excitation. There is a clear shift in the $\Omega_{SPR}(t)$ and changes in the SPR width (ω(t)) over time. This clear shift of the SPR band is proposed to be a result of the interaction of Ag with TiO_2.[139] This could further support the electron transfer from Ag to TiO_2 at visible excitation.

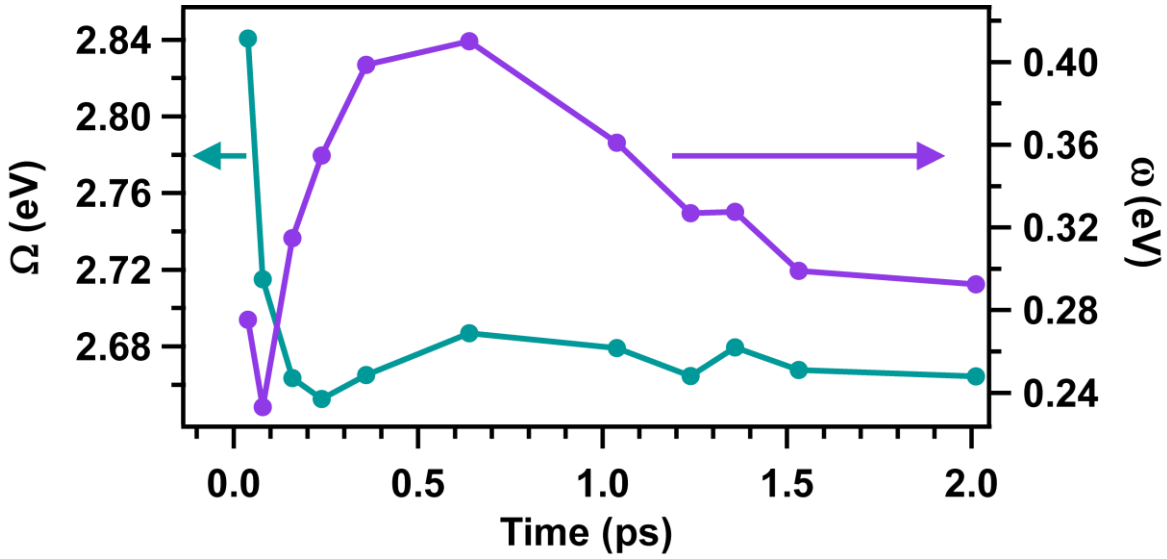

Figure 6.19. Plasmon band parameters Ω_{SPR} (t) (blue trace) and ω(t) (purple trace) as determined from Gaussian fit in equation (6.4) are shown as a function of time.

While we cannot quantify the electron transfer from Ag to TiO_2 in the Ag-TiO_2 film, given the data we have shown, we can certainly conclude that there is an interaction between Ag and TiO_2 in the film. It is possible that the electron transfer from the Ag to TiO_2 is a direct electron transfer which occurs on the order of 20 fs.[36] Such fast electron transfer cannot be observed with the time resolution of our experiment. This process involves direct generation of hot electrons in the electron absorbing orbitals of the semiconductor, in this case TiO_2. This can occur when the semiconductor is in close contact with the metal. This is certainly possible for our Ag-TiO_2 film given that the Ag nanoparticles are in direct contact with TiO_2.

6.4 Conclusions

Multicolor photochromism in Ag-TiO_2 is a well-established phenomenon. However, not a lot of work has been done to understand the excited state properties of Ag-TiO_2 films. We used femtosecond transient absorption spectroscopy to gain further insights into the Ag-TiO_2 system upon UV and visible illumination. Using 300 nm pulses to excite TiO_2 in the Ag-TiO_2 film, we successfully excited electrons within TiO_2 which were then transferred into the Ag nanoparticles.

The electron transfer from TiO_2 to Ag upon UV illumination was around 2 ps. This electron transfer supports the co-catalysis effect, where electrons excited from the valence band to conduction band of the semiconductor TiO_2, accumulated in the TiO_2 conduction band and then transferred over to a co-catalyst, Ag.

We also explored the effects of visible illumination on the Ag-TiO_2 film. With 450 nm excitation, TiO_2 alone will not promote electrons into its conduction band. However, with Ag nanoparticle interaction, when the Ag SPR band is excited, it can directly transfer its electron over to TiO_2. While we were unable to quantify this electron transfer, we presented evidence that could indicate the electron transfer could simply be too fast to observe in the time resolution of our experiments. A fast electron transfer on the order of 20 fs would be indicative of a direct electron transfer to a semiconductor from the metal. In order to further study the visible illumination of the Ag-TiO_2 film, it would be useful to probe signals in the near infrared or infrared. There, we could monitor signals that are due only to TiO_2 and would not have contributions from the SPR in Ag NPs. Clearly, there is still more to be discovered about the nature of electron transfer in Ag-TiO_2 films upon visible illumination. Gaining further insights into this mechanism could lead to further understanding the applications that these materials can be used for.

Chapter 7. Conclusions and Outlook

In this dissertation, we studied optical and excited-state properties in complex metal alloy systems. First, we explored the steady-state optical properties in $(Ga_{1-x}Zn_x)(N_{1-x}O_x)$ nanoparticles. In Chapter 3, optical properties in $(Ga_{1-x}Zn_x)(N_{1-x}O_x)$ were explored using diffuse reflectance spectroscopy. We used a band fluctuations model, where an Urbach tail and a direct bandgap were fit to diffuse reflectance transformed Kubelka-Munk plots of samples with various x values and differing compositions. We determined that there is an Urbach tail with energies of ~160-180 meV in all samples, regardless of composition or elemental distribution. A trend in the inhomogeneous samples was observed, where the Urbach energy increased with increasing x value. Perhaps an increase in the ZnO content results in greater inhomogeneity, thus increasing the Urbach tail. Since all samples, homogenous and heterogeneous, exhibited the Urbach tail, it must not simply be due to inhomogeneity, but also defect states.

Next, we studied the excited-state properties in $(Ga_{1-x}Zn_x)(N_{1-x}O_x)$ nanoparticles. Chapters 4 and 5 informed the behavior of excited charge carriers. First, in Chapter 4, we focused on the transient absorption (TA) study of nanoparticles with x=0.40 that were synthesized at 650 °C. We discovered that the carriers in these particles exhibit a carrier density-dependent spectral blueshift which is described by the Burstein-Moss effect. Knowing that the carrier decay in these particles could be modeled using the Burstein-Moss theory, we were able to calculate the reduced effective mass of excited carriers. We found that the reduced effective mass in $(Ga_{0.6}Zn_{0.4})(N_{0.6}O_{0.4})$ nanoparticles is quite large, $0.68m_0$, where m_0 is the electron rest mass. This lends us to information about the curvature of the bands and the mobilities of the carriers in these particles. We also sought to determine the origin of the short and long-lived decay components previously observed in $(Ga_{1-}$

$_xZn_x)(N_{1-x}O_x)$ nanoparticles. Using a carrier recombination model, we determined that the short-lived component is a result of trap mediated and Auger recombination within the particles. We found that the trap mediated and Auger recombination rate constants agree with literature values for semiconductor systems. The long-lived component was thought to be a result of a broad distribution of trap states and trap-limited recombination. From here, we moved on to study the excited-state decay in particles with different elemental distributions.

In Chapter 5, we compared the trap mediated and Auger recombination rate constants in $(Ga_{1-x}Zn_x)(N_{1-x}O_x)$ nanoparticles with homogeneous (synthesized at 800 °C) and heterogeneous (synthesized at 650 °C) distributions. The recombination rate constants were very similar among all the particle samples studied. In other words, the elemental distribution did not change the carrier dynamics. In this chapter, we also observed the NIR TA spectra and used MB as an electron scavenger to determine which carriers, electrons or holes, the TA signals were due to. We determined that free carriers observed in the NIR are most likely signal from holes and the short decay component we observe in the visible bleach is also due to holes, while the long-lived signal is due to electrons. Further work with more electron and hole scavenger experiments could conclusively demonstrate the signal dependence on each carrier.

Finally, in Chapter 6, we used TA spectroscopy to study an Ag-TiO_2 film. We were able to quantify the electron transfer from TiO_2 to Ag upon UV illumination as 2 ps, which supports the co-catalysis effect. We also studied the excited state spectra and decay kinetics of the Ag-TiO_2 film after visible illumination and determined that there is certainly an interaction between Ag and TiO_2 when the SPR is excited in Ag. We were unable to conclusively determine whether the signals observed were in fact due to electron transfer into TiO_2, but we do believe it is possible that the

transfer occurs on a very fast timescale, supporting a direct electron transfer. Further studies exploring TA signals in the NIR will lend to a better understanding of this electron transfer.

The main goal of the work presented in this dissertation was to gain new insights about the excited-state and optical properties of complex materials. The excited-state dynamics in $(Ga_{1-x}Zn_x)(N_{1-x}O_x)$ nanoparticles have previously not been comprehensively studied or well understood. Ag-TiO_2 is a system that has been studied using electrochemical methods, but extensive work to study the excited-state dynamics of Ag-TiO_2 films using femtosecond transient absorption spectroscopy was requiring more study. The work in this dissertation expands our fundamental knowledge of these materials. In particular, we now have a better understanding of the behavior of charge carriers in these materials after excitation. Knowledge of this fundamental behavior can provide insights into future material production for solar fuel generation.

References

1 Lewis, N. S.; Nocera, D. G.: Powering the planet: Chemical challenges in solar energy utilization. *Proceedings of the National Academy of Sciences* **2006**, *103*, 15729-15735.

2 Holdren, J. P.: Energy and Sustainability. *Science* **2007**, *315*, 737.

3 Zou, C.; Zhao, Q.; Zhang, G.; Xiong, B.: Energy revolution: From a fossil energy era to a new energy era. *Natural Gas Industry B* **2016**, *3*, 1-11.

4 Munawer, M. E.: Human health and environmental impacts of coal combustion and post-combustion wastes. *Journal of Sustainable Mining* **2018**, *17*, 87-96.

5 Milner, A. M.; Khamis, K.; Battin, T. J.; Brittain, J. E.; Barrand, N. E.; Füreder, L.; Cauvy-Fraunié, S.; Gíslason, G. M.; Jacobsen, D.; Hannah, D. M.; Hodson, A. J.; Hood, E.; Lencioni, V.; Ólafsson, J. S.; Robinson, C. T.; Tranter, M.; Brown, L. E.: Glacier shrinkage driving global changes in downstream systems. *Proceedings of the National Academy of Sciences* **2017**, 201619807.

6 Godbold, J. A.; Calosi, P.: Ocean acidification and climate change: advances in ecology and evolution. *Philosophical Transactions of the Royal Society B: Biological Sciences* **2013**, *368*, 20120448.

7 Prada, F.; Caroselli, E.; Mengoli, S.; Brizi, L.; Fantazzini, P.; Capaccioni, B.; Pasquini, L.; Fabricius, K. E.; Dubinsky, Z.; Falini, G.; Goffredo, S.: Ocean warming and acidification synergistically increase coral mortality. *Scientific Reports* **2017**, *7*, 40842.

8 Gust, D.; Moore, T. A.; Moore, A. L.: Solar Fuels via Artificial Photosynthesis. *Accounts of Chemical Research* **2009**, *42*, 1890-1898.

9 Blankenship, R. E.; Tiede, D. M.; Barber, J.; Brudvig, G. W.; Fleming, G.; Ghirardi, M.; Gunner, M. R.; Junge, W.; Kramer, D. M.; Melis, A.; Moore, T. A.; Moser, C. C.; Nocera, D. G.; Nozik, A. J.; Ort, D. R.; Parson, W. W.; Prince, R. C.; Sayre, R. T.: Comparing Photosynthetic and Photovoltaic Efficiencies and Recognizing the Potential for Improvement. *Science* **2011**, *332*, 805.

10 Turner, J. A.: Sustainable Hydrogen Production. *Science* **2004**, *305*, 972.

11 Maeda, K.; Takata, T.; Hara, M.; Saito, N.; Inoue, Y.; Kobayashi, H.; Domen, K.: GaN:ZnO Solid Solution as a Photocatalyst for Visible-Light-Driven Overall Water Splitting. *Journal of the American Chemical Society* **2005**, *127*, 8286-8287.

12 Maeda, K.; Teramura, K.; Takata, T.; Hara, M.; Saito, N.; Toda, K.; Inoue, Y.; Kobayashi, H.; Domen, K.: Overall Water Splitting on (Ga1-xZnx)(N1-xOx) Solid Solution Photocatalyst: Relationship between Physical Properties and Photocatalytic Activity. *The Journal of Physical Chemistry B* **2005**, *109*, 20504-20510.

13 Maeda, K.; Teramura, K.; Lu, D.; Takata, T.; Saito, N.; Inoue, Y.; Domen, K.: Photocatalyst releasing hydrogen from water. *Nature* **2006**, *440*, 295-295.

14 Maeda, K.; Teramura, K.; Lu, D.; Takata, T.; Saito, N.; Inoue, Y.; Domen, K.: Characterization of Rh−Cr Mixed-Oxide Nanoparticles Dispersed on (Ga1-xZnx)(N1-xOx) as a Cocatalyst for Visible-Light-Driven Overall Water Splitting. *J. Phys. Chem. B* **2006**, *110*, 13753-13758.

15 Maeda, K.; Teramura, K.; Masuda, H.; Takata, T.; Saito, N.; Inoue, Y.; Domen, K.: Efficient Overall Water Splitting under Visible-Light Irradiation on (Ga1-xZnx)(N1-xOx) Dispersed with Rh−Cr Mixed-Oxide Nanoparticles: Effect of Reaction Conditions on Photocatalytic Activity. *J. Phys. Chem. B* **2006**, *110*, 13107-13112.

16 Maeda, K.; Domen, K.: New Non-Oxide Photocatalysts Designed for Overall Water Splitting under Visible Light. *The Journal of Physical Chemistry C* **2007**, *111*, 7851-7861.

17 Maeda, K.; Hashiguchi, H.; Masuda, H.; Abe, R.; Domen, K.: Photocatalytic Activity of (Ga1-xZnx)(N1-xOx) for Visible-Light-Driven H2 and O2 Evolution in the Presence of Sacrificial Reagents. *The Journal of Physical Chemistry C* **2008**, *112*, 3447-3452.

18 Maeda, K.; Teramura, K.; Domen, K.: Effect of post-calcination on photocatalytic activity of (Ga1−xZnx)(N1−xOx) solid solution for overall water splitting under visible light. *Journal of Catalysis* **2008**, *254*, 198-204.

19 Hisatomi, T.; Maeda, K.; Lu, D.; Domen, K.: The Effects of Starting Materials in the Synthesis of (Ga1−xZnx)(N1−xOx) Solid Solution on Its Photocatalytic Activity for Overall Water Splitting under Visible Light. *ChemSusChem* **2009**, *2*, 336-343.

20 Hisatomi, T.; Maeda, K.; Takanabe, K.; Kubota, J.; Domen, K.: Aspects of the Water Splitting Mechanism on (Ga1-xZnx)(N1-xOx) Photocatalyst Modified with $Rh_{2-y}Cr_yO_3$ Cocatalyst. *J. Phys. Chem. C* **2009**, *113*, 21458-21466.

21 Maeda, K.; Domen, K.: Solid Solution of GaN and ZnO as a Stable Photocatalyst for Overall Water Splitting under Visible Light. *Chem. Mater.* **2010**, *22*, 612-623.

22 Ohno, T.; Bai, L.; Hisatomi, T.; Maeda, K.; Domen, K.: Photocatalytic Water Splitting Using Modified GaN:ZnO Solid Solution under Visible Light: Long-Time Operation and Regeneration of Activity. *Journal of the American Chemical Society* **2012**, *134*, 8254-8259.

23 Li, Y.; Zhu, L.; Yang, Y.; Song, H.; Lou, Z.; Guo, Y.; Ye, Z.: A Full Compositional Range for a (Ga1-x Zn x)(N1-x O x) Nanostructure: High Efficiency for Overall Water Splitting and Optical Properties. *Small* **2015**, *11*, 871-876.

24 Hahn, C.; Fardy, M. A.; Nguyen, C.; Natera-Comte, M.; Andrews, S. C.; Yang, P.: Synthesis and Photocatalytic Properties of Single Crystalline (Ga1-xZnx)(N1-xOx) Nanotubes. *Israel Journal of Chemistry* **2012**, *52*, 1111-1117.

25 Lee, K.; Tienes, B. M.; Wilker, M. B.; Schnitzenbaumer, K. J.; Dukovic, G.: (Ga1–xZnx)(N1–xOx) Nanocrystals: Visible Absorbers with Tunable Composition and Absorption Spectra. *Nano Letters* **2012**, *12*, 3268-3272.

26 Lee, K.; Lu, Y.-G.; Chuang, C.-H.; Ciston, J.; Dukovic, G.: Synthesis and characterization of (Ga1-xZnx)(N1-xOx) nanocrystals with a wide range of compositions. *Journal of Materials Chemistry A* **2016**, *4*, 2927-2935.

27 Jensen, L. L.; Muckerman, J. T.; Newton, M. D.: First-Principles Studies of the Structural and Electronic Properties of the (Ga1-xZnx)(N1-xOx) Solid Solution Photocatalyst. *The Journal of Physical Chemistry C* **2008**, *112*, 3439-3446.

28 Wei, W.; Dai, Y.; Yang, K.; Guo, M.; Huang, B.: Origin of the Visible Light Absorption of GaN-Rich Ga1−x ZnxN1−xOx (x = 0.125) Solid Solution. *The Journal of Physical Chemistry C* **2008**, *112*, 15915-15919.

29 Huda, M. N.; Yan, Y.; Wei, S.-H.; Al-Jassim, M. M.: Electronic structure of ZnO:GaN compounds: Asymmetric bandgap engineering. *Physical Review B* **2008**, *78*, 195204.

30 Wang, S.; Wang, L.-W.: *Atomic and Electronic Structures of GaN/ZnO Alloys*, 2010; Vol. 104.

31 Di Valentin, C.: Electronic Structure of (Ga1−xZnx)N1−xOx Photocatalyst for Water Splitting by Hybrid Hartree-Fock Density Functional Theory Methods. *The Journal of Physical Chemistry C* **2010**, *114*, 7054-7062.

32 Li, L.; Allen, P.: *Phase diagram, structure, and electronic properties of (Ga1-xZnx)(N1-xOx) solid solution*, 2011.

33 McDermott, E. J.; Kurmaev, E. Z.; Boyko, T. D.; Finkelstein, L. D.; Green, R. J.; Maeda, K.; Domen, K.; Moewes, A.: Structural and Band Gap Investigation of GaN:ZnO Heterojunction Solid Solution Photocatalyst Probed by Soft X-ray Spectroscopy. *The Journal of Physical Chemistry C* **2012**, *116*, 7694-7700.

34 Tongying, P.; Lu, Y.-G.; Hall, L. M. G.; Lee, K.; Sulima, M.; Ciston, J.; Dukovic, G.: Control of Elemental Distribution in the Nanoscale Solid-State Reaction That Produces (Ga1–xZnx)(N1–xOx) Nanocrystals. *ACS Nano* **2017**, *11*, 8401-8412.

35 Chuang, C.-H.; Lu, Y.-G.; Lee, K.; Ciston, J.; Dukovic, G.: Strong Visible Absorption and Broad Time Scale Excited-State Relaxation in (Ga1–xZnx)(N1–xOx) Nanocrystals. *Journal of the American Chemical Society* **2015**, *137*, 6452-6455.

36 Zhang, Y.; He, S.; Guo, W.; Hu, Y.; Huang, J.; Mulcahy, J. R.; Wei, W. D.: Surface-Plasmon-Driven Hot Electron Photochemistry. *Chemical Reviews* **2018**, *118*, 2927-2954.

37 Giannini, V.; Fernández-Domínguez, A. I.; Heck, S. C.; Maier, S. A.: Plasmonic Nanoantennas: Fundamentals and Their Use in Controlling the Radiative Properties of Nanoemitters. *Chemical Reviews* **2011**, *111*, 3888-3912.

38 Hartland, G. V.: Optical Studies of Dynamics in Noble Metal Nanostructures. *Chemical Reviews* **2011**, *111*, 3858-3887.

39 DuChene, J. S.; Niu, W.; Abendroth, J. M.; Sun, Q.; Zhao, W.; Huo, F.; Wei, W. D.: Halide Anions as Shape-Directing Agents for Obtaining High-Quality Anisotropic Gold Nanostructures. *Chem. Mater.* **2013**, *25*, 1392-1399.

40 DuChene, J. S.; Almeida, R. P.; Wei, W. D.: Facile synthesis of anisotropic Au@SiO2 core–shell nanostructures. *Dalton Transactions* **2012**, *41*, 7879-7882.

41 Yu, S.; Wilson, A. J.; Kumari, G.; Zhang, X.; Jain, P. K.: Opportunities and Challenges of Solar-Energy-Driven Carbon Dioxide to Fuel Conversion with Plasmonic Catalysts. *ACS Energy Letters* **2017**, *2*, 2058-2070.

42 Tatsuma, T.; Nishi, H.; Ishida, T.: Plasmon-induced charge separation: chemistry and wide applications. *Chemical Science* **2017**, *8*, 3325-3337.

43 Amirav, L.; Alivisatos, A. P.: Photocatalytic Hydrogen Production with Tunable Nanorod Heterostructures. *The Journal of Physical Chemistry Letters* **2010**, *1*, 1051-1054.

44 Schneider, C. A.; Rasband, W. S.; Eliceiri, K. W.: NIH Image to ImageJ: 25 years of image analysis. *Nature Methods* **2012**, *9*, 671.

45 Maeda, K.; Teramura, K.; Saito, N.; Inoue, Y.; Kobayashi, H.; Domen, K.: Overall water splitting using (oxy)nitride photocatalysts. *Pure and Applied Chemistry* **2006**, *78*, 2267-2276.

46 Yoshida, M.; Hirai, T.; Maeda, K.; Saito, N.; Kubota, J.; Kobayashi, H.; Inoue, Y.; Domen, K.: Photoluminescence Spectroscopic and Computational Investigation of the Origin of the Visible Light Response of (Ga1−xZnx)(N1−xOx) Photocatalyst for Overall Water Splitting. *The Journal of Physical Chemistry C* **2010**, *114*, 15510-15515.

47 RajaAmbal, S.; Yadav, A. K.; Jha, S. N.; Bhattacharyya, D.; Gopinath, C. S.: Electronic structure–sunlight driven water splitting activity correlation of (Zn1−yGay)(O1−zNz). *Physical Chemistry Chemical Physics* **2014**, *16*, 23654-23662.

48 Menon, S. S.; Kuppulingam, B.; Baskar, K.; Sairam, T. N.; Ravindran, T. R.; Gupta, B.; Singh, S.: Realization of high photocatalytic hydrogen generation activity by nanostructured Ga1−xZnxO1−zNz solid-solution without co-catalyst. *International Journal of Hydrogen Energy* **2015**, *40*, 13901-13908.

49 Zhang, Y.; Fang, D.-Q.; Zhang, S.-L.; Huang, R.; Wen, Y.-H.: Structural and electronic properties of ZnO/GaN heterostructured nanowires from first-principles study. *Physical Chemistry Chemical Physics* **2016**, *18*, 3097-3102.

50 Zhang, Y.; Wu, Z.-F.; Gao, P.-F.; Fang, D.-Q.; Zhang, S.-L.: Enhanced visible light absorption in ZnO/GaN heterostructured nanofilms. *Journal of Alloys and Compounds* **2017**, *704*, 478-483.

51 Lee, Y.-C.; Lin, T.-Y.; Wu, C.-W.; Teng, H.; Hu, C.-C.; Hu, S.-Y.; Yang, M.-D.: Visible luminescence properties of (Ga1−xZnx)(N1−xOx) solid solution (x = 0.22). *Journal of Applied Physics* **2011**, *109*, 073506.

52 Reinert, A. A.; Payne, C.; Wang, L.; Ciston, J.; Zhu, Y.; Khalifah, P. G.: Synthesis and Characterization of Visible Light Absorbing (GaN)1–x(ZnO)x Semiconductor Nanorods. *Inorg. Chem.* **2013**, *52*, 8389-8398.

53 Dou, M.; Persson, C.: Band gap reduction and dielectric function of Ga1−xZnxN1−xOx and In1−xZnxN1−xOx alloys. *physica status solidi (a)* **2012**, *209*, 75-78.

54 Nelson, J.: *The Physics of Solar Cells*, 2003; Vol. 57.

55 Klingshirn, C. F.: *Semiconductor Optics*; 4 ed.; Springer-Verlag Berlin Heidelberg, 2012.

56 Guerra, J.; Tejada, A.; Korte, L.; Kegelmann, L.; Töfflinger, J.; Albrecht, S.; Rech, B.; Weingärtner, R.: *Determination of the complex refractive index and optical bandgap of CH3NH3PbI3 thin films*, 2017; Vol. 121.

57 Shirayama, M.; Kadowaki, H.; Miyadera, T.; Sugita, T.; Tamakoshi, M.; Kato, M.; Fujiseki, T.; Murata, D.; Hara, S.; Murakami, T. N.; Fujimoto, S.; Chikamatsu, M.; Fujiwara, H.: Optical Transitions in Hybrid Perovskite Solar Cells: Ellipsometry, Density Functional Theory, and Quantum Efficiency Analyses for ${\mathrm{CH}}_{3}{\mathrm{NH}}_{3}{\mathrm{PbI}}_{3}$. *Physical Review Applied* **2016**, *5*, 014012.

58 Guerra, J. A.; Angulo, J. R.; Gomez, S.; Llamoza, J.; Montañez, L. M.; Tejada, A.; Töfflinger, J. A.; Winnacker, A.; Weingärtner, R.: The Urbach focus and optical properties of amorphous hydrogenated SiC thin films. *Journal of Physics D: Applied Physics* **2016**, *49*, 195102.

59 Guerra, J. A.; Montañez, L. M.; Tucto, K.; Angulo, J.; Töfflinger, J. A.; Winnaker, A.; Weingärtner, R.: Bandgap Engineering of Amorphous Hydrogenated Silicon Carbide. *MRS Advances* **2016**, *1*, 2929-2934.

60 Cooper, J. K.; Gul, S.; Toma, F. M.; Chen, L.; Liu, Y.-S.; Guo, J.; Ager, J. W.; Yano, J.; Sharp, I. D.: Indirect Bandgap and Optical Properties of Monoclinic Bismuth Vanadate. *The Journal of Physical Chemistry C* **2015**, *119*, 2969-2974.

61 S. Lewis, N.; Crabtree, G.: *Basic Research Needs for Solar Energy Utilization: report of the Basic Energy Sciences Workshop on Solar Energy Utilization, April 18-21, 2005*, 2005.

62 Walter, M. G.; Warren, E. L.; McKone, J. R.; Boettcher, S. W.; Mi, Q.; Santori, E. A.; Lewis, N. S.: Solar Water Splitting Cells. *Chemical Reviews* **2010**, *110*, 6446-6473.

63 Chen, Z.; Jaramillo, T. F.; Deutsch, T. G.; Kleiman-Shwarsctein, A.; Forman, A. J.; Gaillard, N.; Garland, R.; Takanabe, K.; Heske, C.; Sunkara, M.; McFarland, E. W.; Domen, K.; Miller, E. L.; Turner, J. A.; Dinh, H. N.: Accelerating materials development for photoelectrochemical hydrogen production: Standards for methods, definitions, and reporting protocols. *Journal of Materials Research* **2010**, *25*, 3-16.

64 Osterloh, F. E.: Inorganic Materials as Catalysts for Photochemical Splitting of Water. *Chem. Mater.* **2008**, *20*, 35-54.

65 Kudo, A.; Miseki, Y.: Heterogeneous photocatalyst materials for water splitting. *Chemical Society Reviews* **2009**, *38*, 253-278.

66 Maeda, K.; Teramura, K.; Saito, N.; Inoue, Y.; Domen, K.: Improvement of photocatalytic activity of (Ga1−xZnx)(N1−xOx) solid solution for overall water splitting by co-loading Cr and another transition metal. *Journal of Catalysis* **2006**, *243*, 303-308.

67 Tseng, H.-W.; Wilker, M. B.; Damrauer, N. H.; Dukovic, G.: Charge Transfer Dynamics between Photoexcited CdS Nanorods and Mononuclear Ru Water-Oxidation Catalysts. *Journal of the American Chemical Society* **2013**, *135*, 3383-3386.

68 Kamat, P. V.; Dimitrijevic, N. M.; Nozik, A. J.: Dynamic Burstein-Moss shift in semiconductor colloids. *The Journal of Physical Chemistry* **1989**, *93*, 2873-2875.

69 Manser, J. S.; Kamat, P. V.: Band filling with free charge carriers in organometal halide perovskites. *Nat Photon* **2014**, *8*, 737-743.

70 Kawamura, K.-i.; Maekawa, K.; Yanagi, H.; Hirano, M.; Hosono, H.: Observation of carrier dynamics in CdO thin films by excitation with femtosecond laser pulse. *Thin Solid Films* **2003**, *445*, 182-185.

71 Hickey, S. G.; Riley, D. J.; Tull, E. J.: Photoelectrochemical Studies of CdS Nanoparticle Modified Electrodes: Absorption and Photocurrent Investigations. *The Journal of Physical Chemistry B* **2000**, *104*, 7623-7626.

72 Muñoz, M.; Pollak, F. H.; Kahn, M.; Ritter, D.; Kronik, L.; Cohen, G. M.: Burstein-Moss shift of n-doped In0.53Ga0.47As/InP. *Physical Review B* **2001**, *63*, 233302.

73 Green, M. A.: Intrinsic concentration, effective densities of states, and effective mass in silicon. *Journal of Applied Physics* **1990**, *67*, 2944-2954.

74 Hanada, T.: Basic Properties of ZnO, GaN, and Related Materials. In *Oxide and Nitride Semiconductors: Processing, Properties, and Applications*; Yao, T., Hong, S.-K., Eds.; Springer Berlin Heidelberg: Berlin, Heidelberg, 2009; pp 1-19.

75 Lambrecht, W. R. L.; Rodina, A. V.; Limpijumnong, S.; Segall, B.; Meyer, B. K.: Valence-band ordering and magneto-optic exciton fine structure in ZnO. *Physical Review B* **2002**, *65*, 075207.

76 Suzuki, M.; Uenoyama, T.; Yanase, A.: First-principles calculations of effective-mass parameters of AlN and GaN. *Physical Review B* **1995**, *52*, 8132-8139.

77 Wang, Z.; Zhao, M.; Wang, X.; Xi, Y.; He, X.; Liu, X.; Yan, S.: Hybrid density functional study of band alignment in ZnO–GaN and ZnO–(Ga1−xZnx)(N1−xOx)–GaN heterostructures. *Physical Chemistry Chemical Physics* **2012**, *14*, 15693-15698.

78 DeLong, K. W.; Gabel, A.; Seaton, C. T.; Stegeman, G. I.: Nonlinear transmission, degenerate four-wave mixing, photodarkening, and the effects of carrier-density-dependent nonlinearities in semiconductor-doped glasses. *J. Opt. Soc. Am. B* **1989**, *6*, 1306-1313.

79 Ghanassi, M.; Schanne-Klein, M. C.; Hache, F.; Ekimov, A. I.; Ricard, D.; Flytzanis, C.: Time-resolved measurements of carrier recombination in experimental semiconductor-doped glasses: Confirmation of the role of Auger recombination. *Applied Physics Letters* **1993**, *62*, 78-80.

80 Klann, R.; Höfer, T.; Buhleier, R.; Elsaesser, T.; Tomm, J. W.: Fast recombination processes in lead chalcogenide semiconductors studied via transient optical nonlinearities. *Journal of Applied Physics* **1995**, *77*, 277-286.

81 Johnston, M. B.; Herz, L. M.: Hybrid Perovskites for Photovoltaics: Charge-Carrier Recombination, Diffusion, and Radiative Efficiencies. *Accounts of Chemical Research* **2016**, *49*, 146-154.

82 Robel, I.; Gresback, R.; Kortshagen, U.; Schaller, R. D.; Klimov, V. I.: Universal Size-Dependent Trend in Auger Recombination in Direct-Gap and Indirect-Gap Semiconductor Nanocrystals. *Physical Review Letters* **2009**, *102*, 177404.

83 Yang, Y.; Yang, M.; Li, Z.; Crisp, R.; Zhu, K.; Beard, M. C.: Comparison of Recombination Dynamics in CH3NH3PbBr3 and CH3NH3PbI3 Perovskite Films: Influence of Exciton Binding Energy. *The Journal of Physical Chemistry Letters* **2015**, *6*, 4688-4692.

84 Vodopyanov, K. L.; Graener, H.; Phillips, C. C.; Tate, T. J.: Picosecond carrier dynamics and studies of Auger recombination processes in indium arsenide at room temperature. *Physical Review B* **1992**, *46*, 13194-13200.

85 Semyonov, O.; Subashiev, A.; Chen, Z.; Luryi, S.: Radiation efficiency of heavily doped bulk n-InP semiconductor. *Journal of Applied Physics* **2010**, *108*, 013101.

86 Zakar, A.; Wu, R.; Chekulaev, D.; Zerova, V.; He, W.; Canham, L.; Kaplan, A.: Carrier dynamics and surface vibration-assisted Auger recombination in porous silicon. *Physical Review B* **2018**, *97*, 155203.

87 Klimov, V. I.; Mikhailovsky, A. A.; McBranch, D. W.; Leatherdale, C. A.; Bawendi, M. G.: Quantization of Multiparticle Auger Rates in Semiconductor Quantum Dots. *Science* **2000**, *287*, 1011.

88 Jha, P. P.; Guyot-Sionnest, P.: Trion Decay in Colloidal Quantum Dots. *ACS Nano* **2009**, *3*, 1011-1015.

89 Kurzmann, A.; Ludwig, A.; Wieck, A. D.; Lorke, A.; Geller, M.: Auger Recombination in Self-Assembled Quantum Dots: Quenching and Broadening of the Charged Exciton Transition. *Nano Letters* **2016**, *16*, 3367-3372.

90 Jiang, Y.; Teich, M. C.; Wang, W. I.: The Auger recombination rate is larger in a GaSb quantum well than in bulk GaSb. *Journal of Applied Physics* **1991**, *69*, 836-840.

91 Lakowicz, J. R.: *Principles of Fluorescence Spectroscopy*; 3 ed.; Springer US: New York, 2006.

92 Cardona, P. Y. a. M.: *Fundamentals of Semiconductors: Physics and Materials Propertues*; 4 ed.; Springer-Verlag Berlin Heidelberg: New York, 2010.

93 Johnston, D. C.: Stretched exponential relaxation arising from a continuous sum of exponential decays. *Physical Review B* **2006**, *74*, 184430.

94 Berberan-Santos, M. N.; Bodunov, E. N.; Valeur, B.: Mathematical functions for the analysis of luminescence decays with underlying distributions 1. Kohlrausch decay function (stretched exponential). *Chemical Physics* **2005**, *315*, 171-182.

95 Williams, G.; Watts, D. C.: Non-symmetrical dielectric relaxation behaviour arising from a simple empirical decay function. *Transactions of the Faraday Society* **1970**, *66*, 80-85.

96 O'Neil, M.; Marohn, J.; McLendon, G.: Dynamics of electron-hole pair recombination in semiconductor clusters. *The Journal of Physical Chemistry* **1990**, *94*, 4356-4363.

97 Dag, I.; Lifshitz, E.: Dynamics of Recombination Processes in PbI2 Nanocrystals Embedded in Porous Silica Films. *The Journal of Physical Chemistry* **1996**, *100*, 8962-8972.

98 Soloviev, V. N.; Eichhöfer, A.; Fenske, D.; Banin, U.: Size-Dependent Optical Spectroscopy of a Homologous Series of CdSe Cluster Molecules. *Journal of the American Chemical Society* **2001**, *123*, 2354-2364.

99 Nelson, J.; Chandler, R. E.: Random walk models of charge transfer and transport in dye sensitized systems. *Coordination Chemistry Reviews* **2004**, *248*, 1181-1194.

100 Clarke, T. M.; Jamieson, F. C.; Durrant, J. R.: Transient Absorption Studies of Bimolecular Recombination Dynamics in Polythiophene/Fullerene Blend Films. *The Journal of Physical Chemistry C* **2009**, *113*, 20934-20941.

101 Godin, R.; Wang, Y.; Zwijnenburg, M. A.; Tang, J.; Durrant, J. R.: Time-Resolved Spectroscopic Investigation of Charge Trapping in Carbon Nitrides Photocatalysts for Hydrogen Generation. *Journal of the American Chemical Society* **2017**, *139*, 5216-5224.

102 Godin, R.; Hisatomi, T.; Domen, K.; Durrant, J. R.: Understanding the visible-light photocatalytic activity of GaN:ZnO solid solution: the role of Rh2−yCryO3 cocatalyst and charge carrier lifetimes over tens of seconds. *Chemical Science* **2018**, *9*, 7546-7555.

103 Barzykin, A. V.; Tachiya, M.: Mechanism of Charge Recombination in Dye-Sensitized Nanocrystalline Semiconductors: Random Flight Model. *The Journal of Physical Chemistry B* **2002**, *106*, 4356-4363.

104 Ibáñez, M.; Zamani, R.; Li, W.; Shavel, A.; Arbiol, J.; Morante, J. R.; Cabot, A.: Extending the Nanocrystal Synthesis Control to Quaternary Compositions. *Crystal Growth & Design* **2012**, *12*, 1085-1090.

105 Aldakov, D.; Lefrançois, A.; Reiss, P.: Ternary and quaternary metal chalcogenide nanocrystals: synthesis, properties and applications. *Journal of Materials Chemistry C* **2013**, *1*, 3756-3776.

106 Fan, F.-J.; Wu, L.; Yu, S.-H.: Energetic I–III–VI2 and I2–II–IV–VI4 nanocrystals: synthesis, photovoltaic and thermoelectric applications. *Energy & Environmental Science* **2014**, *7*, 190-208.

107 Teresa Buscaglia, M.; Harnagea, C.; Dapiaggi, M.; Buscaglia, V.; Pignolet, A.; Nanni, P.: Ferroelectric BaTiO3 Nanowires by a Topochemical Solid-State Reaction. *Chem. Mater.* **2009**, *21*, 5058-5065.

108 Buscaglia, M. T.; Sennour, M.; Buscaglia, V.; Bottino, C.; Kalyani, V.; Nanni, P.: Formation of Bi4Ti3O12 One-Dimensional Structures by Solid-State Reactive Diffusion.

From Core−Shell Templates to Nanorods and Nanotubes. *Crystal Growth & Design* **2011**, *11*, 1394-1401.

109 He, X.; Wang, J.; Dai, Z.; Wang, L.; Tian, G.: The Synthesis of LiMnxFe1-xPO4/C Cathode Material through Solvothermal Jointed with Solid-State Reaction. In *Materials (Basel)*, 2016; Vol. 9.

110 McArthur, E. A.; Morris-Cohen, A. J.; Knowles, K. E.; Weiss, E. A.: Charge Carrier Resolved Relaxation of the First Excitonic State in CdSe Quantum Dots Probed with Near-Infrared Transient Absorption Spectroscopy. *The Journal of Physical Chemistry B* **2010**, *114*, 14514-14520.

111 Bychto, L.; Patryn, A.: Modulated free-carrier absorption in silicon – a spectroscopy approach. *physica status solidi (b)* **2015**, *252*, 1311-1318.

112 Tamaki, Y.; Furube, A.; Katoh, R.; Murai, M.; Hara, K.; Arakawa, H.; Tachiya, M.: Trapping dynamics of electrons and holes in a nanocrystalline TiO2 film revealed by femtosecond visible/near-infrared transient absorption spectroscopy. *Comptes Rendus Chimie* **2006**, *9*, 268-274.

113 Dworak, L.; Roth, S.; Scheffer, M. P.; Frangakis, A. S.; Wachtveitl, J.: A thin CdSe shell boosts the electron transfer from CdTe quantum dots to methylene blue. *Nanoscale* **2018**, *10*, 2162-2169.

114 Yang, Y.; Wu, K.; Shabaev, A.; Efros, A. L.; Lian, T.; Beard, M. C.: Direct Observation of Photoexcited Hole Localization in CdSe Nanorods. *ACS Energy Letters* **2016**, *1*, 76-81.

115 Singhal, G. S.; Rabinowitch, E.: Changes in the absorption spectrum of methylene blue with pH. *The Journal of Physical Chemistry* **1967**, *71*, 3347-3349.

116 Huang, J.; Huang, Z.; Yang, Y.; Zhu, H.; Lian, T.: Multiple Exciton Dissociation in CdSe Quantum Dots by Ultrafast Electron Transfer to Adsorbed Methylene Blue. *Journal of the American Chemical Society* **2010**, *132*, 4858-4864.

117 Naoi, K.; Ohko, Y.; Tatsuma, T.: TiO2 Films Loaded with Silver Nanoparticles: Control of Multicolor Photochromic Behavior. *Journal of the American Chemical Society* **2004**, *126*, 3664-3668.

118 Nadar, L.; Sayah, R.; Vocanson, F.; Crespo-Monteiro, N.; Boukenter, A.; Sao Joao, S.; Destouches, N.: Influence of reduction processes on the colour and photochromism of amorphous mesoporous TiO2 thin films loaded with a silver salt. *Photochemical & Photobiological Sciences* **2011**, *10*, 1810-1816.

119 Tobaldi, D. M.; Leonardi, S. G.; Pullar, R. C.; Seabra, M. P.; Neri, G.; Labrincha, J. A.: Sensing properties and photochromism of Ag–TiO2 nano-heterostructures. *Journal of Materials Chemistry A* **2016**, *4*, 9600-9613.

120 Ohko, Y.; Tatsuma, T.; Fujii, T.; Naoi, K.; Niwa, C.; Kubota, Y.; Fujishima, A.: Multicolour photochromism of TiO2 films loaded with silver nanoparticles. *Nature Materials* **2002**, *2*, 29.

121 Kawahara, K.; Suzuki, K.; Ohko, Y.; Tatsuma, T.: Electron transport in silver-semiconductor nanocomposite films exhibiting multicolor photochromism. *Physical Chemistry Chemical Physics* **2005**, *7*, 3851-3855.

122 Crespo-Monteiro, N.; Destouches, N.; Nadar, L.; Reynaud, S.; Vocanson, F.; Y. Michalon, J.: *Irradiance influence on the multicolor photochromism of mesoporous TiO2 films loaded with silver nanoparticles*, 2011; Vol. 99.

123 Ding, I.-K.; Zhu, J.; Cai, W.; Moon, S.-J.; Cai, N.; Wang, P.; Zakeeruddin, S. M.; Grätzel, M.; Brongersma, M. L.; Cui, Y.; McGehee, M. D.: Plasmonic Dye-Sensitized Solar Cells. *Advanced Energy Materials* **2011**, *1*, 52-57.

124 Wang, F.; Li, C.; Chen, H.; Jiang, R.; Sun, L.-D.; Li, Q.; Wang, J.; Yu, J. C.; Yan, C.-H.: Plasmonic Harvesting of Light Energy for Suzuki Coupling Reactions. *Journal of the American Chemical Society* **2013**, *135*, 5588-5601.

125 Cushing, S. K.; Li, J.; Meng, F.; Senty, T. R.; Suri, S.; Zhi, M.; Li, M.; Bristow, A. D.; Wu, N.: Photocatalytic Activity Enhanced by Plasmonic Resonant Energy Transfer from Metal to Semiconductor. *Journal of the American Chemical Society* **2012**, *134*, 15033-15041.

126 Tian, Y.; Tatsuma, T.: Mechanisms and Applications of Plasmon-Induced Charge Separation at TiO2 Films Loaded with Gold Nanoparticles. *Journal of the American Chemical Society* **2005**, *127*, 7632-7637.

127 Bois, L.; Chassagneux, F.; Battie, Y.; Bessueille, F.; Mollet, L.; Parola, S.; Destouches, N.; Toulhoat, N.; Moncoffre, N.: Chemical Growth and Photochromism of Silver Nanoparticles into a Mesoporous Titania Template. *Langmuir* **2010**, *26*, 1199-1206.

128 Utterback, J. K.; Grennell, A. N.; Wilker, M. B.; Pearce, O. M.; Eaves, J. D.; Dukovic, G.: Observation of trapped-hole diffusion on the surfaces of CdS nanorods. *Nature Chemistry* **2016**, *8*, 1061.

129 Sachs, M.; Pastor, E.; Kafizas, A.; Durrant, J. R.: Evaluation of Surface State Mediated Charge Recombination in Anatase and Rutile TiO2. *The Journal of Physical Chemistry Letters* **2016**, *7*, 3742-3746.

130 Wang, X.; Kafizas, A.; Li, X.; Moniz, S. J. A.; Reardon, P. J. T.; Tang, J.; Parkin, I. P.; Durrant, J. R.: Transient Absorption Spectroscopy of Anatase and Rutile: The Impact of Morphology and Phase on Photocatalytic Activity. *The Journal of Physical Chemistry C* **2015**, *119*, 10439-10447.

131 Kafizas, A.; Wang, X.; Pendlebury, S. R.; Barnes, P.; Ling, M.; Sotelo-Vazquez, C.; Quesada-Cabrera, R.; Li, C.; Parkin, I. P.; Durrant, J. R.: Where Do Photogenerated Holes Go in Anatase:Rutile TiO2? A Transient Absorption Spectroscopy Study of Charge Transfer and Lifetime. *The Journal of Physical Chemistry A* **2016**, *120*, 715-723.

132 Cowan, A. J.; Tang, J.; Leng, W.; Durrant, J. R.; Klug, D. R.: Water Splitting by Nanocrystalline TiO2 in a Complete Photoelectrochemical Cell Exhibits Efficiencies Limited by Charge Recombination. *The Journal of Physical Chemistry C* **2010**, *114*, 4208-4214.

133 Tamaki, Y.; Furube, A.; Murai, M.; Hara, K.; Katoh, R.; Tachiya, M.: Direct Observation of Reactive Trapped Holes in TiO2 Undergoing Photocatalytic Oxidation of Adsorbed Alcohols: Evaluation of the Reaction Rates and Yields. *Journal of the American Chemical Society* **2006**, *128*, 416-417.

134 Yoshihara, T.; Katoh, R.; Furube, A.; Tamaki, Y.; Murai, M.; Hara, K.; Murata, S.; Arakawa, H.; Tachiya, M.: Identification of Reactive Species in Photoexcited Nanocrystalline TiO2 Films by Wide-Wavelength-Range (400−2500 nm) Transient Absorption Spectroscopy. *The Journal of Physical Chemistry B* **2004**, *108*, 3817-3823.

135 Tamaki, Y.; Hara, K.; Katoh, R.; Tachiya, M.; Furube, A.: Femtosecond Visible-to-IR Spectroscopy of TiO2 Nanocrystalline Films: Elucidation of the Electron Mobility before Deep Trapping. *The Journal of Physical Chemistry C* **2009**, *113*, 11741-11746.

136 Gaál, A.; Bugar, I.; Capek, I.; Fialová, L.; Pálszegi, T.; Szöcs, V.; Satka, A.; Uherek, F.: *Femtosecond multicolor transient absorption spectroscopy of colloidal silver nanoparticles*, 2009; Vol. 19.

137 Karam, T. E.; Khoury, R. A.; Haber, L. H.: Excited-state dynamics of size-dependent colloidal TiO2-Au nanocomposites. *The Journal of Chemical Physics* **2016**, *144*, 124704.

138 Baldoví, H.; Albarracin, F.; Atienzar, P.; Ferrer, B.; Alvaro, M.; Garcia, H.: *Visible-Light Photoresponse of Gold Nanoparticles Supported on TiO2: A Combined Photocatalytic, Photoelectrochemical, and Transient Spectroscopy Study*, 2014; Vol. 16.

139 Aiboushev, A.; Gostev, F.; Shelaev, I.; Kostrov, A.; Kanaev, A.; Museur, L.; Traore, M.; Sarkisov, O.; Nadtochenko, V.: Spectral properties of the surface plasmon resonance and electron injection from gold nanoparticles to TiO2 mesoporous film: femtosecond study. *Photochemical & Photobiological Sciences* **2013**, *12*, 631-637.

140 Du, L.; Furube, A.; Hara, K.; Katoh, R.; Tachiya, M.: Ultrafast plasmon induced electron injection mechanism in gold–TiO2 nanoparticle system. *Journal of Photochemistry and Photobiology C: Photochemistry Reviews* **2013**, *15*, 21-30.

141 Stamplecoskie, K. G.; Manser, J. S.: Facile SILAR Approach to Air-Stable Naked Silver and Gold Nanoparticles Supported by Alumina. *ACS Applied Materials & Interfaces* **2014**, *6*, 17489-17495.

142 Hirakawa, T.; Kamat, P. V.: Charge Separation and Catalytic Activity of Ag@TiO2 Core−Shell Composite Clusters under UV−Irradiation. *Journal of the American Chemical Society* **2005**, *127*, 3928-3934.

143 Diesen, V.; Dunnill, C. W.; Österberg, E.; Parkin, I. P.; Jonsson, M.: Silver enhanced TiO2 thin films: photocatalytic characterization using aqueous solutions of tris(hydroxymethyl)aminomethane. *Dalton Transactions* **2014**, *43*, 344-351.

144 Couzon, N.; Maillard, M.; Bois, L.; Chassagneux, F.; Brioude, A.: Electrochemical Observation of the Plasmonic Effect in Photochromic Ag Nanoparticle Filled Mesoporous TiO2 Films. *The Journal of Physical Chemistry C* **2017**, *121*, 22147-22155.

145 Okumu, J.; Dahmen, C.; Sprafke, A. N.; Luysberg, M.; Plessen, G. v.; Wuttig, M.: Photochromic silver nanoparticles fabricated by sputter deposition. *Journal of Applied Physics* **2005**, *97*, 094305.

146 Gahlot, S.; Thakur, A.; Kulshrestha, V.; K. Shahi, V.: *Synthesis and Characterization of TiO2 and Ag/TiO2 Nanostructure*, 2013; Vol. 1512.

147 Katoh, R.; Murai, M.; Furube, A.: Transient absorption spectra of nanocrystalline TiO2 films at high excitation density. *Chemical Physics Letters* **2010**, *500*, 309-312.